



**HAL**  
open science

# Oscillateurs optoélectroniques à base de résonateurs silicium pour applications à la génération de signaux hyperfréquences et aux capteurs

Thi Phuong Do

► **To cite this version:**

Thi Phuong Do. Oscillateurs optoélectroniques à base de résonateurs silicium pour applications à la génération de signaux hyperfréquences et aux capteurs. Physique [physics]. Université Paris Saclay (COmUE), 2019. Français. NNT : 2019SACLN024 . tel-02292979

**HAL Id: tel-02292979**

**<https://theses.hal.science/tel-02292979>**

Submitted on 20 Sep 2019

**HAL** is a multi-disciplinary open access archive for the deposit and dissemination of scientific research documents, whether they are published or not. The documents may come from teaching and research institutions in France or abroad, or from public or private research centers.

L'archive ouverte pluridisciplinaire **HAL**, est destinée au dépôt et à la diffusion de documents scientifiques de niveau recherche, publiés ou non, émanant des établissements d'enseignement et de recherche français ou étrangers, des laboratoires publics ou privés.

# Silicon Resonators Based Optoelectronic Oscillators for Applications in Microwave Signal Generation and Sensing

Thèse de doctorat de l'Université Paris-Saclay  
Préparée à L'École normale supérieure Paris-Saclay

École doctorale n°575 Electrical, optical, bio:  
Physics and engineering (EOBE)

Spécialité de doctorat : Électronique et Optoélectronique, Nano-et  
Microtechnologies

Thèse présentée et soutenue à Cachan, le 2 juillet 2019

**Do Thi Phuong**

Composition du Jury:

Eric CASSAN C2N, Université Paris-Sud - Université Paris-Saclay	Président du Jury
Emmanuel BIGLER (FEMTO-ST)	Rapporteur
Joel CHARRIER FONTO, Université de Rennes 1	Rapporteur
Jean-Luc POLLEUX ESYCOM, ESIEE Paris, Université Paris-Est	Examineur
Isabelle LEDOUX RAK LPQM, École normale supérieure Paris-Saclay	Directrice de thèse
Bernard JOURNET LPQM, École normale supérieure Paris-Saclay	Invité







## Table of Contents

<b>Acknowledgements</b> .....	<b>I</b>
<b>List of figures</b> .....	<b>III</b>
<b>List of tables</b> .....	<b>VII</b>
<b>Résumé en Français</b> .....	<b>IX</b>
<b>Introduction</b> .....	<b>1</b>
<b>1.Optoelectronic Oscillator</b> .....	<b>5</b>
1.1. Oscillators.....	5
1.1.1 Oscillation conditions.....	5
1.1.2. Oscillator phase noise .....	8
1.1.3. Passive component of choice for microwave oscillators .....	14
1.2. OEO based on delay line .....	15
1.2.1. Principle of operation of OEO based on delay line .....	16
1.2.2. Analytical study of the OEO .....	18
1.2.3. Drawbacks of classical OEO.....	20
1.2.4. Applications of the opto-electronic oscillator .....	23
1.3. OEO based on optical resonator .....	26
1.3.1. Principle of operation.....	26
1.3.2. Optical resonator in the OEO system.....	28
1.3.3. Integrated microwave photonics .....	31
1.3.4. Integrated optoelectronic oscillator.....	34
1.4. Conclusion.....	37
<b>2. Silicon Ring Resonator Design, Fabrication and Characterization for OEO Loops...</b>	<b>40</b>
2.1. Integration within silicon photonics .....	40
2.1.1. Basic functions in silicon photonics.....	41
2.1.2. Silicon photonics for bulk index sensing applications.....	45
2.2. Silicon micro-ring resonators .....	50

2.2.1. Waveguide families.....	50
2.2.2. Silicon ring resonators.....	54
2.3. Silicon micro-ring resonator design .....	63
2.3.1. Waveguide chosen parameters.....	63
2.3.2. Final design of the RR directional coupler .....	66
2.3.3. Full ring resonator design strategy.....	67
2.4. Fabrication processing of micro-ring resonators based on the Si technology.....	69
2.4.1. Description of the passive Si structures fabrication process.....	70
2.4.2. Mask preparation for E-beam lithography .....	71
2.4.3. Fabrication results .....	73
2.5. Optical characterization of spiral ring resonators.....	74
2.6. Conclusion.....	79
<b>3. Investigation of OEO Configurations Including Silicon Ring Resonators .....</b>	<b>81</b>
3.1. Direct insertion of a millimeter -long silicon ring resonator into an optoelectronic oscillator loop.....	82
3.1.1. Study of the realized microwave photonic filter .....	82
3.1.2. Opto-electronic oscillator based on a millimeter-long silicon ring resonator .....	85
3.1.2a. Oscillation signal properties .....	86
3.1.3. Refractive index measurement based on mm-long Si RR integrated into an OEO loop.....	93
3.2. Wideband tunable microwave signal generation based on silicon photonic resonator.....	97
3.2.1. Principle of operation .....	97
3.2.2. Silicon ring resonator design and fabrication .....	99
3.2.3. Generation of an oscillation signal.....	101
3.2.4. Tunable oscillation signal .....	104
3.2.5. Application to index sensing.....	106

3.3. Conclusion.....	111
<b>Conclusion and Perspectives .....</b>	<b>114</b>
<b>References .....</b>	<b>118</b>



# Acknowledgements

First and foremost, I would like to express my special appreciation and thanks to my supervisor - Prof. ERIC CASSAN. He is the one who taught, guided and motivated me entering in the silicon photonic field since the very beginning of this thesis. I thank him for taking his time, for all his patience, responsibility, enthusiasm, encouragement, support and continuous optimism during my Ph.D journey. It has been a pleasure working under his supervision, learning from his experience and expertise.

I would like to send my sincere thanks to my other supervisors, Prof. ISABELLE LEDOUX-RAK and Dr. BERNARD JOURNET, who allowed me to enter this project. Especially, I would thank BERNARD JOURNET for his guidance, for all the discussion between us and for helping me with the RF experiment.

My special thank goes to Dr. CARLOS ALONSO-RAMOS. For me, Carlos like my other supervisor, who always take care of my work. I would like to thank him for helping me with the experiments, for his fruitful discussions, excellent idea, as well as his inspiration, have encouraged me to enrich my knowledge.

I would like to thank XAVIER LE ROUX, who is specialized in clean-room work. This work could not be achieved without his help. I deeply thank him for our discussion, for teaching me the fabrication technique and for making my design became real.

I would also thank Prof. PAUL CROZAT, Dr. DIEGO PÉREZ-GALACHO, and Dr. WEIWEI ZHANG, Dr. ELENA DURAN for all helps during my thesis. A big thank to my thesis committee members, for letting my defense be an enjoyable moment, and for your brilliant comments and suggestions.

For more than 3 years of my thesis, I have a chance to work under excellent team spirit. I would like to thank all members of C2N and LPQM, who always helped and shared with me my difficulty and happy moments.

Last but not least, I am deepest grateful and wish to offer my sincere thanks to my parents and my sister who always besides, encourage and motivate me to follow my dream.

Paris, 22 July 2019

Do Thi Phuong

# List of figures

<b>Fig.1.1.1.</b> Block diagram of a sinusoidal oscillator using an amplifier with an angular frequency dependent feedback path .....	6
<b>Fig. 1.1.2.</b> (a) Modulus and (b) Phase of the transfer function $H(j\omega)$ in case of $Q=5$ and $Q=20$ ; $H_0=1$ .....	7
<b>Figure 1.1.3.</b> Power spectrum of the ideal and real signal generated by the oscillator. Red line: Perfect signal, Blue line: signal impacted by phase noise.....	9
<b>Fig.1.1.4.</b> The impact of the phase noise into the spectrum of the oscillation signa .....	10
<b>Figure 1.1.5.</b> Power spectral density of phase noise at the output of an oscillator. (a) $f_n < \Delta f/2$ (low $Q$ ) and (b) $f_n > \Delta f/2$ (high $Q$ .....	14
<b>Fig 1.2.1.</b> Basic scheme of an opto-electronic oscillator (OEO) .....	16
<b>Fig.1.2.2.</b> Example of oscillator spectrum, at 18 GHz, with a fiber length of 1.5 km. The oscillator FSR is approximately 134 kHz (only).....	20
<b>Fig 1.2.5.</b> Main idea of the implementation of the OEO in the 5G Mobile and Wireless Networks <sup>41</sup> . A low phase oscillator signal is distributed to the base stations from a central station via one optical link. The number of base stations which benefit from the oscillator line depends on several parameters of the OEO and on the conditions of the central station.....	24
<b>Fig.1.3.1.</b> Schematic configuration of the OEO based on optical resonator (top) (PD: photo-detector) and working principle of the system (bottom) .....	27
<b>Fig.1.3.2.</b> Three of the most common types of WGM resonators: (a) a microsphere, (b) a micro disk, (c) a microtoroid .....	30
<b>Fig.1.3.3.</b> Examples of IMWP in different platform. (a) Programmable signal processor SOI <sup>70</sup> , (b) All-integrated tunable filter in indium phosphide <sup>71</sup> and (c) High spectral resolution bandpass filter silicon nitride .....	33
<b>Fig.1.3.4.</b> Different integrated OEO based on different substrates and approaches: (a) Lithium niobite (LiNbO3) WGM resonator <sup>39,98</sup> , (b) InP optical delay line <sup>94</sup> , (c) Chalcogenide stimulated Brillouin scattering <sup>95</sup> , (d) Phase modulator and micro-disk resonator (MDR) on SOI .....	35

<b>Fig.2.1.1.</b> Examples of silicon-based laser: (a) Microsphere Er doped laser <sup>106</sup> , (b) First electrical pump silicon laser based on Ge <sup>108</sup> and (c) III-V based silicon laser using hybrid InP <sup>109</sup> .....	42
<b>Fig.2.1.2.</b> Examples of: (a) Silicon-based modulator using plasmonic dispersion effect <sup>125</sup> and (b) Silicon-based photodetector using Ge <sup>132</sup> .....	44
<b>Fig 2.1.3.</b> Scheme of the evanescent field sensing <sup>153</sup> .....	46
<b>Fig 2.1.4.</b> (a) Typical method used in bulk optical refractive index sensors by measuring the wavelength change dependent on the cover refractive index of the sample, (b) The RI sensitivity is determined by the slope of the wavelength shift for known changes in the sample cover material RI.....	47
<b>Fig.2.2.1.</b> Various types of SOI waveguide structures.....	51
<b>Fig.2.2.2.</b> Typical mode profiles of various waveguide structures at 1.55 $\mu\text{m}$ wavelength: (a) and (b) TE and TM modes strip waveguide, respectively, (c) TE mode rib waveguide and (d) TE mode slot waveguide .....	53
<b>Fig.2.2.3.</b> Ring resonator configuration: (a) All-pass and (b) Add-drop RR.....	54
<b>Fig.2.2.4.</b> Example of transmission spectrum of (a) all-pass and (b) add-drop RR.....	56
<b>Fig.2.2.5.</b> Quality factor as function of perimeter length for different propagation loss in (a) all - pass configuration and (b) add - drop ring configuration.....	57
<b>Fig.2.2.6.</b> (a) Schematic of the super-mode theory of waveguide directional coupler and (b) example of symmetric (even) and asymmetric (odd) modes calculated from an optical mode solver at 1.55 $\mu\text{m}$ wavelength .....	59
<b>Fig.2.2.7.</b> $L_c/L_b$ ratio corresponding to a RR critical condition calculated from Eq. (2.2.13) as function of waveguide loss and for different resonator lengths .....	62
<b>Fig.2.3.1.</b> Refractive index sensitivity as function of waveguide width.....	64
<b>Fig.2.3.2.</b> Electric field energy distributed for TM mode of strip waveguide at 1.55 $\mu\text{m}$ wavelength. ....	65
<b>Fig.2.3.4.</b> The beating length $L_b$ calculated as function of coupling gap $d$ (SOI waveguide geometry: $h = 220$ nm, $w = 350$ nm, $n_{PMMMA} = 1.484$ , TM waveguide operate at 1.55 $\mu\text{m}$ ).....	66
<b>Fig.2.3.5.</b> Design structure of spiral add-drop RR, $R$ : smallest bending radius, $W_c$ : spacing between two successive turns, $L_{str}$ : length of straight path length in the spiral shape .....	67
<b>Fig.2.3.6.</b> Design structure of the directional coupler.....	68
<b>Fig.2.3.7.</b> Schematic of spiral RRs illustrate for the flexibility variation of combination of $L_c/d$ (here $L_{c1}/d_1$ and $L_{c2}/d_2$ ) while maintain the spiral length.....	69

<b>Fig.2.4.1.</b> SOI RR fabrication process applied within the C2N clean room for the fabrication of the silicon photonic samples: (a) Preparation of SOI wafer, (b) ZEP-520A photoresist deposition, (c) E- beam lithography, (d) Development, (e) Etching and (f) Cleaning step .....	70
<b>Fig.2.4.2.</b> Example of .npf file including (a) RR shape inside 500 $\mu\text{m}$ $\times$ 500 $\mu\text{m}$ main-field consisting of (b) 10 $\mu\text{m}$ x 10 $\mu\text{m}$ size subfields .....	72
<b>Fig.2.4.3.</b> (a) and (b):Assume the writing mechanisms of e-beam lithography system along the coupling path length, the red line describes a direction of the beam moving stage, (c) Fabrication error in the coupling region, (d) Successful fabrication result after applying the empirical method to control the beam writing .....	73
<b>Fig.2.4.3.</b> Fabrication result of spiral SOI RR. (a) of spiral rings fabricated in the sample, (b) zoom-in in one device, (c) Detail of coupling region, (d) Detail of grating coupler .....	74
<b>Fig.2.5.1.</b> Experimental setup for optical characterization of Silicon.....	75
<b>Fig.2.5.2.</b> (a) The coupling efficiency as a function of a wavelength for nominal grating coupler designs and (b) Typical transmission spectral of a spiral RR (coupling gap $d = 400$ nm, coupling length $L_C = 7$ $\mu\text{m}$ ).....	76
<b>Fig.2.5.3.</b> (a) The zoom-in in the optical transmission and (b) the Lorentzian fitting for the resonance peak (coupling gap $d = 400$ nm, coupling length $L_c = 7$ $\mu\text{m}$ ).....	78
<b>Fig.2.5.4.</b> Variation of the micro-ring drop port extinction ratio and loaded quality factor $Q$ depending on the coupling length (here for a coupling gap $d = 400$ nm) at 1550 nm wavelength (marker: experimental results and line curve: fitting curve) .....	79
<b>Fig. 3.1.1.</b> Schematic of the studied configuration to characterize the open loop microwave response of the OEO, i.e. to study the realized equivalent microwave bandpass filter MPF. PC: Polarization controller, IM: Intensity modulator, RR: Ring resonator, EDFA: Erbium-doped amplifier, PD: Photo-detector, G: RF amplifier, VNA: Vector network analyzer.....	83
<b>Fig.3.1.2.</b> $S_{21}$ transmission coefficient's magnitude deduced from the integration of Silicon spiral RR.....	84
<b>Fig. 3.1.3.</b> Experimental setup schematic of the OEO based on a silicon spiral RR .....	86
<b>Fig.3.1.4.</b> Spectrum of the signal generated by the OEO based on spiral Silicon RR.....	86
<b>Fig. 3.1.5.</b> (a) RF spectrum of the signal generated by the OEO acquired in the Max-Hold mode of the RF spectral analyser. (b) Phase noise measurement of the generated oscillation frequency collected several times .....	88
<b>Fig.3.1.6.</b> Phase noise spectral of OEO based on silicon RR for the two .....	91

<b>Fig.3.1.7.</b> (a) Spiral RR with the opened window for sensing detection, (b) Capture picture showing the set of available refractive index liquids, and (c) List of used refractive index liquids .....	93
<b>Fig. 3.1.8.</b> (a) Plot of the normalization of S21 when differences cladding index values are used and (b) S21 center frequency changed as a function of the refractive index unit .....	95
<b>Fig. 3.2.1.</b> (a) Basic schematic and (b) Principle of operation of the proposed tunable OEO. In (a), IM: Intensity modulator, RR: Ring resonator and PD: Photodetector. In (b), the red curve corresponds to the optical carrier (or laser source frequency); the orange curve illustrates the sideband lobes of the modulated signal, the blue curve indicates the optical transfer function of the RR and the green one represents the generated RF frequency $f_{RF}$ .....	98
<b>Fig.3.2.2.</b> (a) Scanning electron microscope image of the fabricated silicon RR, (b) Grating coupler and (c) Bending curve .....	99
<b>Fig.3.2.3.</b> Experimental optical transmission of the silicon RR (coupling gap: 300 nm, coupling length: 4.5 $\mu\text{m}$ ). .....	100
<b>Fig.3.2.4.</b> Experimental setup of the proposed tunable OEO in open loop configuration. OSA: Optical spectrum analyzer. PC: Polarization controller, IM: Intensity modulator, RR: Ring resonator, EDFA: Erbium doped amplifier, PD: Photodetector, G: RF amplifiers, VNA: Vector network analyzer, OSA: Optical spectrum analyzer .....	101
<b>Fig. 3.2.5.</b> (a) S <sub>21</sub> transmission coefficient's magnitude of the beating frequency between laser and resonance wavelength, (b) S <sub>21</sub> transmission coefficient's phase focus around highest magnitude value .....	102
<b>Fig. 3.2.6.</b> (a) Oscillation spectrum of the generated signal based on our proposed approach, (b) zoom-in view and (c) Phase noise characteristic of the created signal.....	104
<b>Fig.3.2.7.</b> (a) Oscillation frequency generated with different laser wavelengths and (b) Plot of the oscillation frequency depending on the beating frequency, i.e. $f_b =  f_0 - f_R$ .....	105
<b>Fig.3.2.8.</b> (a) Phase noise characteristic for differences generated signals and (b) Observed phase noise level at 1 MHz offset frequency from carrier .....	106
<b>Fig.3.2.9.</b> A proof of concept experiment setup dedicated to refractive sensing based on a proposed OEO .....	107
<b>Fig.3.2.10.</b> (a) Optical transmission and (b) Electrical spectrum depending on temperature	109
<b>Fig.3.2.11.</b> Calculation of oscillation changes versus refractive index variations.....	110

# List of tables

<b>Table 1.2.1.</b> Different types of OEO based on delay line and their performances .....	22
<b>Table 1.3.1.</b> IOEO based on different approaches. WGM: Whispering gallery mode, ODL: optical delay line, SBS: stimulated Brillouin scattering, PM to IM: phase to intensity modulation, MDR: micro-disk resonator. ....	34
<b>Table 2.3.1.</b> Beating length calculated for different coupling gaps (SOI waveguide: $h = 220$ nm, $w = 350$ nm, $n_{\text{PMMA}} = 1.484$ , TM waveguide operate at $1.55$ $\mu\text{m}$ ) .....	67
<b>Table 2.5.1.</b> Losses parameters of our RR.....	77



# Résumé en Français

Ce travail de thèse est une contribution à l'intégration des éléments constitutifs d'un **oscillateur optoélectronique (OEO)** en photonique intégrée. Il s'intègre au domaine plus vaste de la photonique microonde.

Dans sa version la plus traditionnelle proposée dès 1996 [Yao-96], la boucle opto-micronde qu'est l'OEO est constituée d'un laser très stable émettant dans la fenêtre télécoms ( $\lambda \sim 1.55 \mu\text{m}$ ), d'un modulateur électro-optique, d'une longue section de fibre ( $\gg 1\text{km}$ ) jouant le rôle de retard, d'un photodétecteur, et d'un ensemble de composants radio-fréquences (RF) comprenant un amplificateur, un filtre sélectif, et coupleur RF (Figure suivante).

Le système se comporte comme un système bouclé traditionnel et présente une condition d'oscillation classique de type Barkhausen permettant la génération de signaux RF. Le signal émis par le laser joue le rôle de porteuse optique, et la fibre apporte le retard nécessaire à produire le terme de phase nécessaire à l'oscillation de l'ensemble rétro-actionné.

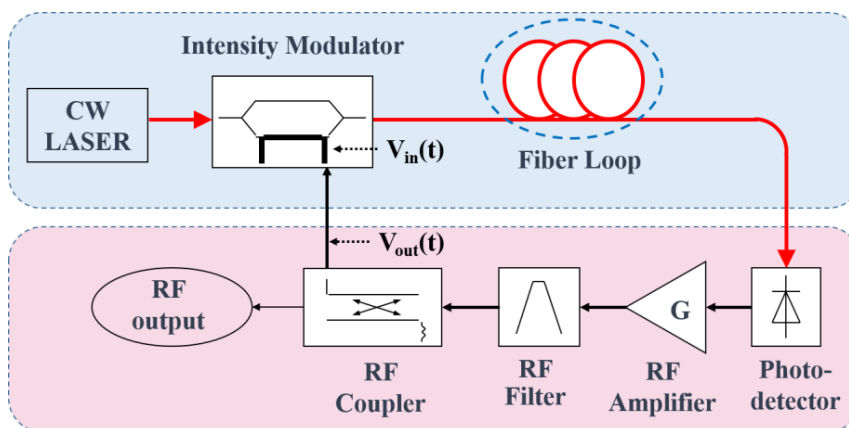


*Schéma de principe d'un oscillateur optoélectronique (OEO) classique, à ligne à retard fibrée.*

Comparé à des systèmes plus classiques d'oscillateurs RF tels que les oscillateurs à quartz à plusieurs étages, cet ensemble comporte un avantage décisif en termes de

pureté spectrale des signaux générés, très bas bruit dans les meilleures réalisations. Intrinsèquement, tous les éléments de la boucle mixte concourent à ce résultat, parmi lesquels la sélectivité du filtre RF passe-bande est un élément clef.

Par rapport aux oscillateurs RF basés, par exemple, sur l'utilisation des résonateurs à quartz, ce système permet d'atteindre aisément et directement des fréquences RF d'opération de plusieurs dizaines de GHz, évitant ainsi l'utilisation d'étages de multiplication de fréquences par mise en cascade, et peut conduire à des régimes d'oscillation produisant des **signaux très bas bruit de phase**. Le bruit de phase des oscillateurs à quartz fonctionnant à une fréquence de 5GHz est ainsi typiquement de  $-145$  dBc/Hz à 10kHz de la porteuse RF [Leli-18] mais se dégrade rapidement pour des fréquences plus élevées.

La **génération de signaux microondes à grande pureté spectrale** est ainsi le point fort des OEO, qui intéressent tout une gamme d'applications allant des contre-mesures dans le domaine des radars et la réalisation de porteuses RF très stables (de fréquence  $f_{RF}$ ) pour la transmission d'informations multiplexées à haute fréquence ( $f_{RF} > 10$  GHz) jusqu'aux applications capteurs. Simultanément, les OEO sont classiquement réalisés à partir de composants discrets, assemblés dans des volumes de plusieurs dizaines de centimètres carrés, voire plusieurs mètres carrés dans les implémentations sur banc optique/RF de développement. Il en résulte une problématique de manque d'intégration, qui nuit beaucoup au déploiement des applications des OEO. Par ailleurs, la présence d'une longue section de fibre conduit à une possible oscillation à chaque fréquence multiple de l'inverse du délai intra-cavité ( $\tau$ ) essentiellement introduit par la fibre, ce qui conduit la structure classique de l'OEO à un fonctionnement facilement multimode non désiré.

Pour ces deux raisons, une modification de boucle a été proposée, reposant sur le remplacement de la section de fibre optique par un résonateur optique. Dans cette option, le résonateur a pour fonction de créer l'équivalent d'un retard temporel important, ce qui rend nécessaire l'utilisation de résonateurs à fort facteur de qualité  $Q$  ( $Q = \pi f_{RF} \tau$ ), typiquement supérieurs à  $10^6$  pour des retards équivalents à quelques km de fibre. Par ailleurs, la modification de la partie optique de la boucle d'une section de fibre à un

résonateur modifie la nature du système bouclé passant d'une structure d'oscillateur à retard à celle d'un oscillateur à filtre déphasant. Cette structure modifiée d'OEO a fait elle-même l'objet de nombreuses études, conduisant à des réalisations marquantes, notamment via l'utilisation de résonateurs à modes de galerie à facteurs de qualité très élevés ( $Q > 10^8$ ) basés sur l'utilisation de sphères de silice [Vol-10].

Sur le principe, les **plateformes d'intégration photonique** et optoélectronique, dont les progrès ont été importants ces dernières années, offrent toutes les blocs nécessaires à l'intégration complète d'un OEO à résonateur en technologie planaire, sur une surface de moins 1 cm<sup>2</sup>, voire moins de 1 mm<sup>2</sup>. L'intégration de composants et de fonctions à base de **semiconducteurs III/V**, typiquement sur substrats InP, offre par exemple une voie possible complète. La **photonique sur silicium**, sur laquelle ce travail de thèse s'appuie principalement, est une autre voie d'intégration possible, présentant avantages et inconvénients par rapport à la voie d'intégration sur plateforme III/V. Les modulateurs électro-optiques (à effet plasma de porteurs libres), les résonateurs optiques (micro-résonateurs en anneau), les photodétecteurs (Germanium sur silicium), les filtres et les amplificateurs RF, sont en principe co-intégrables sur la même plateforme silicium [Viv- 13]. Seule la source laser silicium n'est pas disponible, bien que les solutions d'intégration de diodes laser III/V sur silicium aient connu récemment des progrès très importants tels que des sources très stables co-intégrées soient maintenant directement disponibles dans la fenêtre télécoms [Sze-17].

Dans ce contexte, différents travaux récents se sont intéressés à l'intégration de systèmes puces à boucle opto-micronde pour la génération de signaux à bas bruit. De manière assez notable, plusieurs contributions importantes ont été publiées très récemment par plusieurs groupes ([Tan-18] : CAS/Chine et Université de Valencia/Espagne, [Zha-17] et [Zha-18] : Ottawa University). Ces travaux ont apporté des contributions intéressantes mais n'ont pas permis de couvrir l'ensemble des problématiques liées à l'intégration d'OEO en photonique. En particulier, l'utilisation de circuits photoniques III/V à base d'InP [Tan- 18] induit des problèmes de complexité de réalisation des circuits et de puissance consommée, tandis que l'intégration sur silicium proposée ([Zha-17], [Zha-18]) n'a pas exploré toutes les voies possibles, et l'ensemble n'a donné lieu à ce jour qu'à quelques rares démonstrations expérimentales.

L'objectif de cette thèse était d'apporter une contribution à l'intégration des oscillateurs optoélectroniques dans la voie d'une intégration sur silicium. La contribution principale apportée a été de concevoir, fabriquer, et caractériser des résonateurs en anneaux silicium sur isolant (SOI), de les intégrer à des boucles opto-microondes d'OEO, de démontrer la possibilité de mise en oscillation des structures bouclées, et de caractériser leurs performances. Les études menées l'ont donc été en travaillant essentiellement sur la base du schéma de principe décrit sur la figure suivante.

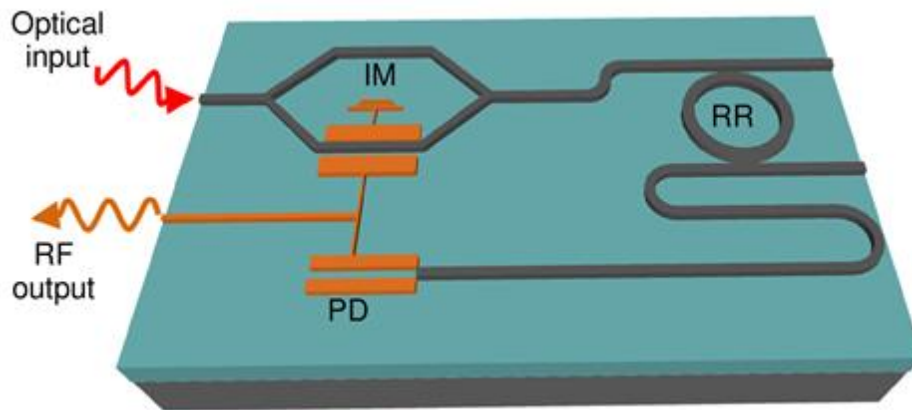


*Schéma de principe idéalisé d'un oscillateur optoélectronique intégré.*

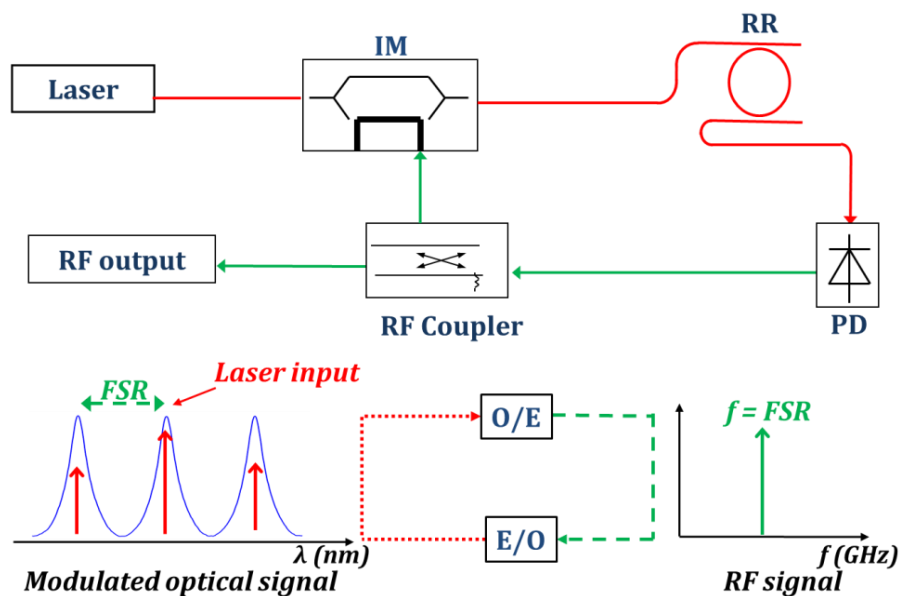
Le manuscrit a été construit autour de trois chapitres, complétés par une introduction et une conclusion, à laquelle nous avons ajouté des perspectives.

Le **chapitre 1** rassemble l'essentiel du contexte et des motivations de la thèse. Un rappel des caractéristiques générales principales des oscillateurs microondes est donné, puis les deux familles principales d'oscillateurs optoélectroniques étudiés dans la littérature y sont introduites. Ce chapitre se termine ensuite par un tour d'horizon des objectifs du travail mené, à savoir principalement l'insertion de résonateurs en anneaux fabriqués en technologie SOI dans une boucle d'un oscillateur optoélectronique, et l'étude des systèmes ainsi réalisés. Plus précisément, le chapitre 1 se pose comme objectifs : i) La réalisation de structures bouclées simples reposant des résonateurs ultra-longes ( $FSR \sim 10\text{GHz}$ ) et un simple modulateur électro-optique d'intensité ; ii) L'exploration de structures plus originales autorisant une accordabilité de la fréquence micro-onde générée la plus large possible ; iii) Une possible application des boucles opto-RF ainsi réalisées à la détection d'indice de réfraction pour la réalisation de capteurs intégrés sensibles (limite de détection  $\ll 10^{-5}$ ).

Le **chapitre 2** décrit toutes les étapes de modélisation, optimisation, fabrication, et caractérisations des résonateurs en anneaux réalisés en photonique SOI en vue de leur intégration dans une boucle opto-microonde. Le **chapitre 3**, quant à lui, rassemble l'ensemble des caractérisations expérimentales des deux principales configurations d'oscillateurs optoélectroniques étudiées au cours de la thèse.

Pour décrire de manière décloisonnée l'ensemble des étapes réalisées ainsi que les résultats obtenus, nous décrivons ci-après en une seule étape l'ensemble des résultats obtenus dans les chapitres 2 et 3.

Le schéma de configuration de base de la **PREMIÈRE CONFIGURATION** étudiée et le principe de fonctionnement de l'OEO basé sur un résonateur en anneau de silicium de FSR directement microondes sont illustrés sur la figure suivante. Dans ce schéma, le signal optique est utilisé comme porteuse optique modulée par un modulateur d'intensité (IM) qui produit deux bandes latérales dans le domaine optique. Le résonateur en anneau (RA) génère un peigne optique qui agit comme un filtre optique. Par le battement de deux lignes de peignes optiques adjacentes dans un photodétecteur (PD), les lignes spectrales optiques sont ensuite traduites dans le domaine RF. Ce procédé consiste essentiellement à créer un filtre passe-bande hyperfréquence équivalent.

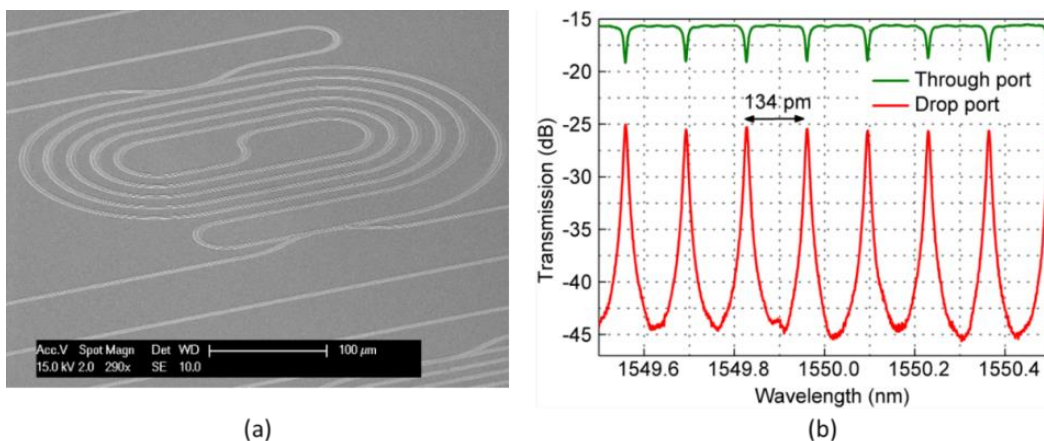


Principe de fonctionnement d'un oscillateur optoélectronique avec micro-résonateur optique.

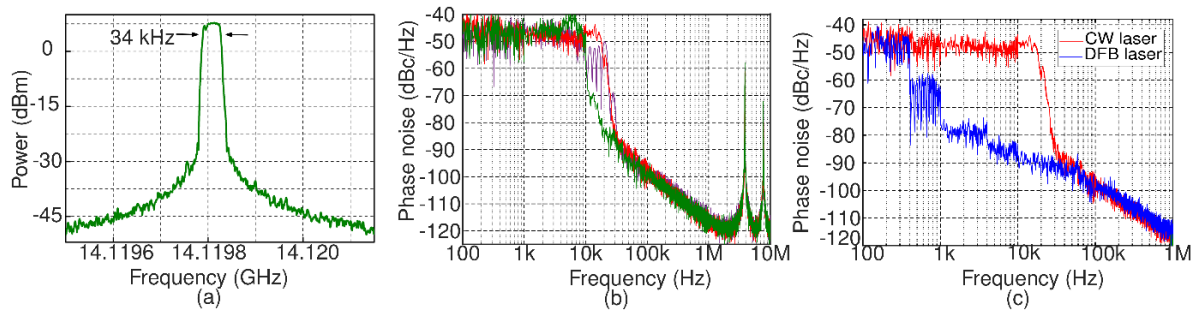
Cette configuration nécessite un résonateur add-drop (RA) avec une gamme spectrale libre optique ( $FSR_{opt}$ ) suffisamment faible, typiquement dans la gamme des cent picomètres ou moins. En conséquence, la longueur du résonateur est alors de quelques millimètres au moins. Afin de réduire l'encombrement de la structure, des RA ont été dessinés sous forme de spirales. Deux jeux de résonateurs à anneau spiralés de largeurs de guides d'ondes différentes de 365 nm et 550 nm ont été conçus et fabriqués. Un exemple de résultat de fabrication est donné ci-après. Les dispositifs ont été testés à l'aide d'un laser accordable couplé au guide d'ondes d'entrée par l'intermédiaire d'un coupleur à réseau avec un angle de couplage correctement ajusté, et le signal extrait de la même manière d'un réseau de sortie. Des FSR d'environ 15 GHz ont été obtenus par cette approche, avec des facteurs de qualité optiques de l'ordre de  $3 \times 10^5$  à  $\lambda = 1,55 \mu\text{m}$ .

Ces résonateurs ont été introduits dans la boucle d'oscillateurs opto-électroniques constitués d'éléments discrets, toujours par des dispositifs d'injection/extraction de la lumière adéquats. Des résultats très concordants de mise en oscillation RF ont été mis en évidence, et les oscillateurs opto-électroniques ainsi réalisés ont été caractérisés en bruit de phase, comme le montrent les figures suivantes.

L'ensemble des résultats a conduit à valider de manière probante la possible utilisation de résonateurs SOI millimétriques à FSR directement compatibles avec une conversion opto-microondes pour la réalisation d'oscillateurs optoélectroniques fonctionnant dans une gamme typiquement de moins de 18 GHz.



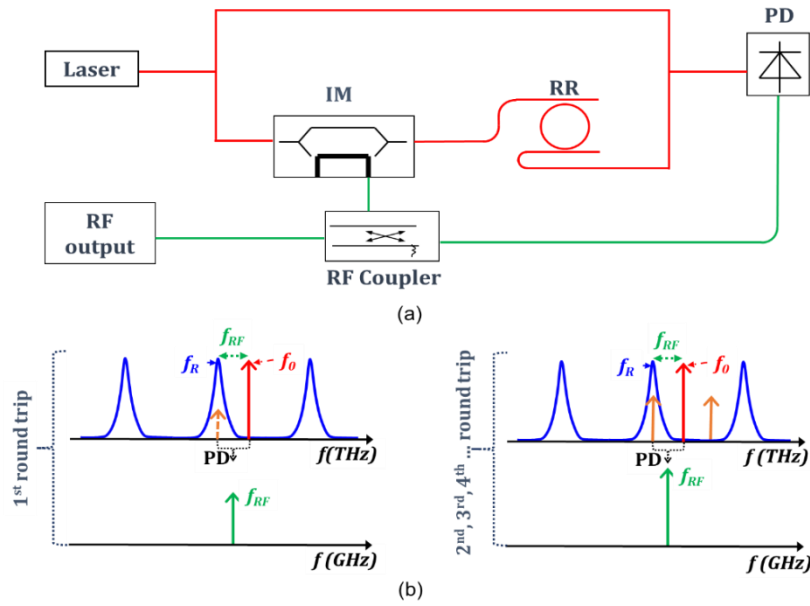
Micro-résonateur en forme de spirale : (a) vue du composant et sa transmission en (b).



Résultats concernant l'oscillateur optoélectronique avec résonateur en spirale : (a) spectre de l'oscillateur en mode "Max-Hold" ; (b) bruit de phase de l'oscillateur ; (c) comparaison entre les bruits de phase obtenus avec différents types de lasers.

Dans une **SECONDE APPROCHE**, nous nous sommes intéressés à une configuration plus originale, que nous avons proposée afin de **répondre à l'enjeu important de la possible accordabilité en fréquence du signal RF généré**. La figure suivante en détaille le principe. Au lieu d'utiliser le résonateur en anneau afin de sélectionner deux raies consécutives amplifiées par le système bouclé hybride, la porteuse optique issue du laser CW utilisé est placée à proximité d'une résonance d'un RA de FSR beaucoup plus important que précédemment ; dans le même temps, le photodétecteur est alimenté simultanément par la raie latérale de modulation issue du RA et la porteuse elle-même, qui est également directement rebouclée sur le photodétecteur. Après démarrage des oscillations à partir du bruit présent dans la boucle, le battement effectué au niveau du photodétecteur est directement issu de la différence de fréquence entre la fréquence de la porteuse et celle de la résonance la plus proche, soit  $f_{RF} = |f_{laser} - f_{résonance}|$ .

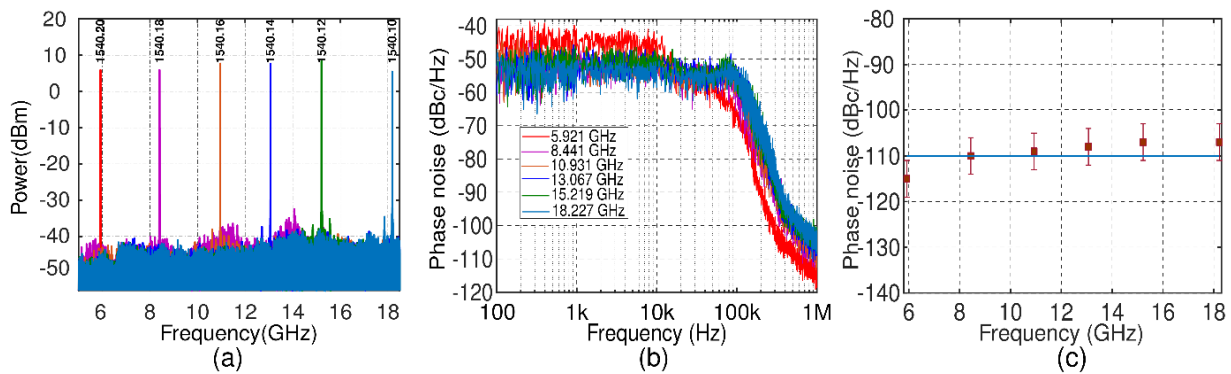
En conséquence, la fréquence microonde générée est alors directement accordable par modification de la fréquence de la porteuse ou par modification de la résonance à fréquence fixe de la porteuse. Sur le principe, il en résulte ainsi un moyen très simple d'obtenir une fréquence RF à la demande (dans la limite des bandes passantes des éléments actifs de la boucle : modulateur, photodétecteur, amplificateur) ou de transformer l'oscillateur optoélectronique en capteur conditionné en fréquence dès lors qu'un stimulus modifie la fréquence de résonance  $f_{résonance}$  (effet thermique, modification d'indice, etc).



Principe de fonctionnement d'un oscillateur optoélectronique à résonateur optique et battement direct avec la raie du laser.

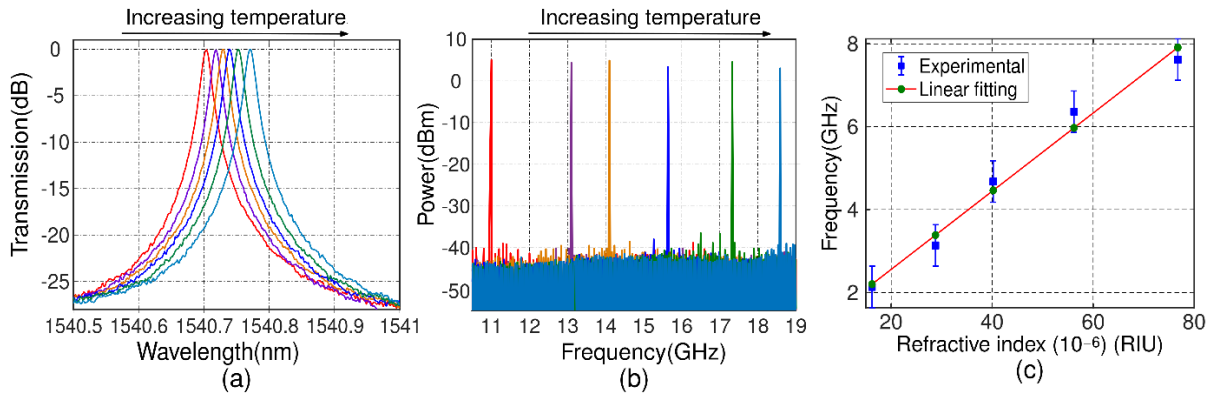
Au travers de modélisations, essais, et caractérisations expérimentales, nous avons testé et vérifié ces principes avec succès, ouvrant une riche voie à des applications et des prolongements ultérieurs.

La figure suivante montre ainsi des spectres et des caractéristiques de bruit de phase obtenus pour des fréquences RF générées comprises entre environ 6 GHz et 18 GHz.



Accordabilité du nouvel oscillateur optoélectronique. Figure (a) : fréquences générées sur une plage de 6 GHz à 18 GHz ; Figure (b) : mesure du bruit de phase sur la même plage de fréquence ; Figure (c) : bruit de phase à 1 MHz d'offset par rapport à la porteuse.

Une estimation de la modification de fréquence obtenue par une variation thermique des indices de réfraction des matériaux constitutifs des résonateurs, en particulier de celui du matériau de couverture, nous a ainsi permis d'estimer une limite de détection de l'ordre de  $10^{-8}$  pour la meilleure des réalisations de la thèse.



Effet d'une variation de la température du résonateur sur la fréquence de l'oscillateur. Figure (a) : influence sur la transmission du résonateur ; Figure (b) : évolution correspondante de la fréquence d'oscillation ; Figure (c) : estimation de la variation de la fréquence d'oscillation en fonction de l'indice de réfraction de la couche de confinement.

- [Yao-96] X. S. Yao, L. Maleki, *IEEE J. Quantum Electron.* 32, 1141 (1996).
- [Leli-18] Lelievre, O., Crozatier, V., Baili, G., et al. "Ultra low noise 10 GHz dual loop optoelectronic oscillator: Experimental results and simple model." 2016 IEEE International Frequency Control Symposium, IFCS 2016 - Proceedings. 2016
- [Vol-10] K. Volyanskiy, P. Salzenstein, H. Tavernier, M. Pogurmirskiy, Y. K. Chembo, Laurent Larger, *Optics Express* 18 (21), 22358-22363 (2010).
- [Sze-17] B. Szelag et al., "Hybrid III-V/Si DFB laser integration on a 220 nm fully CMOS-compatible silicon photonics platform", 2017 IEEE International Electron Devices Meeting (*IEDM*), 2-6 Dec. 2017, INSPEC Accession Number: 17507954, DOI: 10.1109/IEDM.2017.8268450
- [Viv-13] L. Vivien, L. Pavesi, « Handbook of Silicon Photonics », CRC Press, 2013, ISBN 9781439836101
- [Tan-18] J. Tang, T. Hao, W. Li, D. Domenech, R. Baños, P. Muñoz, N. Zhu, J. Capmany, M. Li, "Integrated optoelectronic oscillator", *Optics Express* Vol. 26, Issue 9, pp. 12257-12265 (2018)
- [Zha-17] W. Zhang, J. Yao, "A silicon photonic integrated frequency-tunable microwave photonic bandpass filter", 2017 International Topical Meeting on Microwave Photonics (MWP), 23-26 Oct. 2017, INSPEC Accession Number: 17398281, DOI: 10.1109/MWP.2017.8168635
- [Zha-18] W. Zhang, J. Yao, "On-chip silicon photonic integrated frequency-tunable bandpass microwave photonic filter", *Optics Letters* 43 (15), pp. 3622-3625 (2018).



# Introduction

The generation of spectral-pure and stable microwave and millimeter wave signals are important for many applications. In this domain, oscillators are pivotal functions for almost any communication, navigation, surveillance, or test and measurement systems. They can be used as local oscillators (LO) to enable frequency up and down conversions, or as reference sources for system synchronization. An oscillator can be found in many applications such as radars, satellites, radio astronomy, data-telecommunication and networks, time and frequency metrology, signal processing, and sensing. The origin of oscillators goes back essentially to nearly 1918 <sup>1</sup> when the first microwave oscillator was invented by using vacuum tubes. In general, a microwave oscillator combines both active and passive devices. The oscillation starts when the gain and phase satisfy the so-called Barkhausen criterion. The oscillation frequency being defined by the passive device. One of the drawbacks of microwave oscillators is that the phase noise of the oscillation signal tends to increase with the frequency of operation. Many electronic design tricks make it possible to minimize the phase noise of oscillators, but a fundamental problem remains concerning all-electronic structures, for which the optoelectronic oscillator (OEO) has provided essential unlock contributions in 1994 <sup>2</sup>. The underlying idea of an OEO is to rely on a hybrid optical/microwave loop system making use of a long length optical fiber with extremely low loss to make microwave signals propagate through an optical carrier and resulting as a whole in an ultra-pure and stable oscillation frequency. The advantage of OEOs compared to other microwave oscillators is that the oscillation frequency can be directly synthesized using high-selectivity microwave filters. The phase noise of the generated signal, therefore, does not increase with operating frequency increase. With great potential for creating low phase noise signals at high frequencies, OEOs can be used in many high-end applications such as satellites, military radar systems, ... However, the first generations of OEOs presented some major challenges. Firstly, they suffered from a frequency drift due to temperature fluctuations in the fiber, that needed a bulky temperature

control box to overcome this drawback. Secondly, the closed opto-RF loop suffered from a multi-mode behavior resulting from the long length optical fiber used as a delay line, giving rise to non-constant oscillation frequency starting operation, multimode behavior and frequency mode hopping.

The inherent drawbacks of classical OEOs based on a long optical fiber line ( $\gg 100$  m, up to few kms) proved to be difficult to solve. An alternative solution was proposed consisting of replacing the optical fiber delay line by a small size and high-quality factor optical resonator <sup>3</sup>. For such structures, the resonator is acting as a microwave filter. This approach brings a great help in reducing the size of OEOs, obviating the need for bulky temperature control systems, and offering a potential way to completely avoid multi-mode and mode hopping behaviors while still providing low phase noise signal properties. Many types of optical resonators have been introduced in OEO by making use Fabry-Perot <sup>4</sup>, fiber-ring resonators <sup>5,6</sup> or whispering gallery mode (WGM) resonators <sup>7,8</sup>. However, these resonators generally suffer from a lack of integration possibilities, thus preventing really solid perspective in terms of OEO integration.

Today, integrated microwave photonics (IMWP) that consists in combining photonic integrated circuits (PIC) technologies and microwave optics has emerged as a field with a great interest due to its potential for enhanced functionalities and robustness as well as a reduction of size, weight, cost, and power consumption of complex systems merging optical and microwave signals <sup>9,10</sup>. The recent development of PICs based on different material substrates such as III-V semiconductors, Lithium Niobate ( $\text{LiNbO}_3$ ), the mainstream Silicon on Insulator (SOI) technology, high-index glasses, Nitrides, and polymers, have opened new perspectives for the potential integrating IMWP and particularly the OEO system. In principle, all the elementary blocks of an OEO (electro-optical modulators, optical resonators, photodetectors, etc.) have been indeed developed for other applications. A full integration of these systems has significant potential to provide low phase noise spectrally pure signals within ultra-compact size footprints, bringing many advantages in comparison with classical OEO systems. Recent developments in this field, i.e. the Brillouin filter based on chalcogenide waveguide or the optical delay lines based on InP, showed impressive results. Nevertheless, silicon

photonics now is considered as one of the main viable technology platforms for high complexity, large-scale photonic circuits because of its compatibility with the manufacturing processes and tools used in the CMOS industry. Moreover, the high core/cladding index contrast of silicon photonic waveguides allows sub-micrometer structure dimensions, tight bends, and close spacings, and in turn, this allows dense packing of optical functions on the surface of a chip. In addition, the quick development of silicon photonic integrated circuits allows for multiple functions in a single chip operating at high frequency. Actually, all basic building blocks necessary for OEO loop such as the laser, modulator, the photodetector have been already implemented in the SOI platform complemented by III/V diode integration through hybrid on-Si integration [11–13](#). Integration on the SOI platform, therefore, can be considered as a promising solution to implement ultra-compact OEOs. In this context, one of the solutions is based on loops with an electro-optical phase modulator and an indirect phase/intensity modulation conversion by using an optical notch filter. Despite this progress, these efforts towards the integration of OEO into the silicon photonic platform have not resulted in definitive and inconvenient solutions, and a diversity of approaches still remains possible.

In this context, the present work aims at exploring the direct insertion of silicon-based add-drop ring resonators in the loop of OEO to anticipate, based on the study of several configurations, the performances that fully integrated OEOs on silicon would have.

**The first chapter** begins with an overview introduction about microwave oscillators. We will then discuss the classical OEO system performances with its working principle, (phase) noise properties, limitations, and applications. Then, a particular study will focus on OEOs based on an optical resonator. Several types of optical resonators integrated into the OEO loop will be described with their advantages and drawbacks. This will allow us, finally, to identify the desirable characteristics for the development of OEOs integrated on a chip.

**Chapter 2** then brings together all the milestones and results we have obtained concerning the design, the fabrication, and the characterization of integrated silicon

photonic resonators designed with a view to their insertion into an OEO loop. To this end, we will quickly describe in a preliminary phase the main components of silicon photonics, starting with optical waveguides and their typical dimensions and index contrast, turns and curved waveguides (particularly useful for the realization of long spirals: from a few tens of  $\mu\text{m}$  to a few cm), etc. A theoretical review of the properties of ring resonators, a description of the principles adopted for the design of lithography masks, as well as the optical characterization methods used, will precede the presentation and analysis of the properties of the realized planar ring resonators.

Following the results obtained in **chapter 2**, **chapter 3** mainly presents the insertion of the realized SOI micro-ring resonators in OEO loop configurations made of external elements (e.g. mainly a laser module, an optical amplitude modulator, RF amplifiers, and a photodiode). Three main results obtained in open loop and closed loop configurations, and application for bulk index sensing will be investigated in this chapter. Recognizing the limitations of traditional OEO structures, particularly in terms of the tunability of the generated microwave signal frequency, a new configuration of OEO is then proposed. The proposed scheme alleviates the use of complex solution to generate ultra-broadband signal tunable frequency without any degradation of the signal performance. We will first explain the working principle of the system, and then study the optical characterization of the micro-ring resonator, and its integration in the OEO loop in both the opened and closed configurations. Then, the frequency tunability of the realized OEO will be studied. As a proof of concept of the overall study, we will finally apply the realized OEOs to the analysis of refractive index measurements, thus preparing a subsequent step of applying the looped chain as a sensor, or even as a biosensor.

# 1

## Optoelectronic Oscillator

This chapter will focus on the optoelectronic oscillator with its configuration, advantages and drawbacks, the possible way to improve system performances, as well as the perspectives to go towards integrated OEOs. Taking into account the fact that the OEO is basically a microwave signal generator, we shall first start with some basic definitions useful for microwave oscillators before entering more into details about OEOs.

### 1.1. Oscillators

The first microwave oscillators were invented at the beginning of the 20th century shortly after the development of vacuum tubes <sup>14,15</sup>. Signals generated by an electronic/RF oscillator can be of different waveform types, including sinusoidal, rectangular, triangular, square and pulse shapes. In this work, we will focus on harmonic oscillators in which a sinusoidal waveform is generated.

We shall present here very classical and well-known results, which are not always associated together. It is important for us to remind all these theoretical points for a better understanding of the oscillators developed in this work.

#### 1.1.1 Oscillation conditions

In most general case, oscillator is a nonlinear circuit which converts a DC power to an AC power. The basic conceptual operation of a sinusoidal oscillator can be described with a feedback circuit shown in Fig 1.1.1. Here we shall use the complex formalism, which supposes that the system is linear

## 1.1. Oscillators

The system includes an amplifier with a gain value  $\underline{A}$ . The output voltage is noted as  $\underline{V}_o(j\omega)$ . This voltage passes through a feedback network with an angular frequency-dependent transfer function  $\underline{H}(j\omega)$  and is added to the input of the circuit  $\underline{V}_i(j\omega)$ .

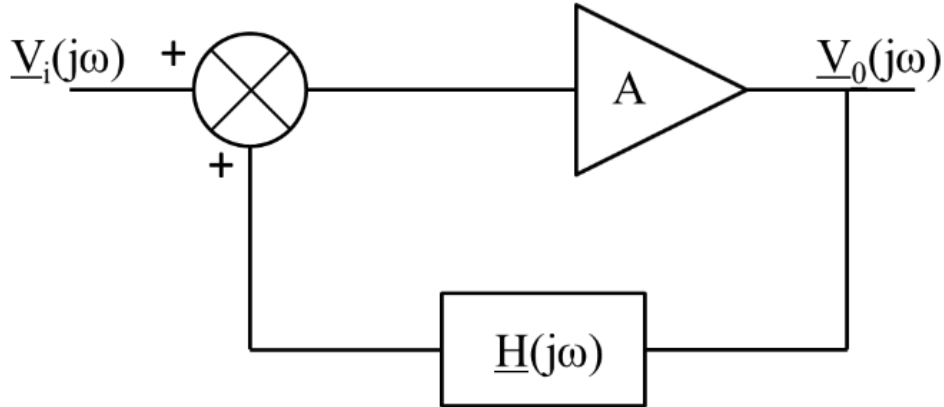


**Fig.1.1.1.** Block diagram of a sinusoidal oscillator using an amplifier with an angular frequency dependent feedback path.

By considering the feedback signal, the output voltage  $V_o(j\omega)$  can be expressed as:

$$\underline{V}_o(j\omega) = \underline{A}\underline{V}_i(j\omega) + \underline{H}(j\omega)\underline{A}\underline{V}_o(j\omega) \quad (1.1.1)$$

which can be solved to yield the output voltage in terms of the input voltage as:

$$\underline{V}_o(j\omega) = \frac{\underline{A}}{1 - \underline{A}\underline{H}(j\omega)} \underline{V}_i(j\omega) \quad (1.1.2)$$

where  $\underline{A}\underline{H}(j\omega)$  is the loop gain. At one particular angular frequency, if the denominator of **Eq. (1.1.2)** becomes zero, it is possible to achieve a non-zero output for a zero-input signal, thus forming an oscillator. The oscillation occurs when the loop gains  $\underline{A}\underline{H}(j\omega)$  is equal to 1. In addition to a condition on the modulus, the phase of  $\underline{H}(j\omega)$  must thus be equal to  $0 \bmod(2\pi)$ , with the hypothesis of  $\underline{A}$  being a real and positive number,  $\underline{A} = A_0$ : it means that the total phase shift around the loop is  $0 \bmod(2\pi)$  or  $k*2\pi$  ( $k$  being an integer).

To conclude, the circuit can oscillate when two conditions, known as the Barkhausen conditions, are satisfied: firstly, the **loop gain must be equal or greater than unity** and secondly the feedback signal must be phase shifted by  $2\pi$  after one turn in the loop.

Here we present the main important points about electronic oscillators by using a very classical transfer function, a second order one:

$$\underline{H}(j\omega) = \frac{H_0}{1 + jQ\left(\frac{\omega}{\omega_0} - \frac{\omega_0}{\omega}\right)} \quad (1.1.3)$$

,  $Q$  being here the quality factor of the microwave filter which can also be expressed by  $Q = \frac{\omega_0}{\Delta\omega}$  (1.1.4) with  $\Delta\omega = 2\pi\Delta f$  and  $\Delta f$  is the filter bandwidth at -3dB.

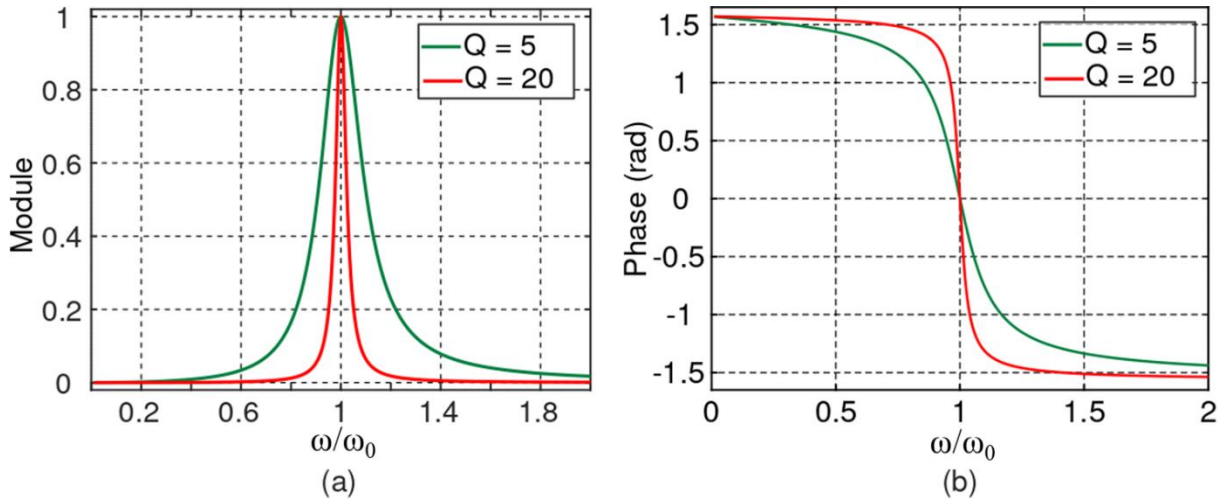


**Fig. 1.1.2.** (a) Modulus and (b) Phase of the transfer function  $H(j\omega)$  in case of  $Q=5$  and  $Q=20$ ;  $H_0=1$ .

As can be seen in **Fig.1.1.2b**, the phase shift of the loop is crossing 0 at the oscillation frequency which is  $f_{osc} = f_0$  ( $\omega_{osc} = \omega_0$ ). Classically it is said that even without input signal ( $V_i = 0$ ), the oscillator can start generating oscillations by amplifying the noise which is always present in the RF components inside the loop, and especially in the amplifier. The oscillation starts with small noise inside the loop. The amplitude of the oscillation signal increases within the loop, but only the frequencies selected in amplitude and phase by the filter can be maintained in the loop, being quickly self-sustaining if a mechanism is in place to guarantee a unitary gain after a one-turn circulation in the loop. After a certain number of turns, the amplitude of the signal is indeed limited by non-linearities, mainly caused by the saturation occurring inside the amplifier when a large signal is amplified, or by an active control mechanism that limits the gain.

## 1.1. Oscillators

As mentioned before, noise existing in the loop is essential for the oscillator to generate the oscillation signal, however, it influences also the quality of the generated signal. The noise inside the oscillator comes from several contributions by different origins from passive and active components (e.g. thermal noise, Schottky noise, etc). Considering noise coming out from the amplifier, a simple hypothesis that a small random phase perturbation produced by the amplifier can be introduced as  $\underline{A} = A_0 e^{j\psi_n}$  can be made. From **Eq. (1.1.3)** and from the Barkhausen oscillation conditions, it is possible to determine the angular oscillation frequency is  $\omega_{osc} = \omega_0 + \delta\omega_n$  as:

$$\delta\omega = \frac{\omega_0}{2Q} \delta\psi_n \quad (1.1.5)$$

Here, we can see that the quality factor influence on the noise can be written as:

$$\left. \frac{d\omega}{d\psi} \right|_{\omega=\omega_0} = \frac{\omega_0}{2Q} \quad (1.1.6)$$

The quality factor  $Q$  of the filter is thus related to the fluctuations of the oscillation frequency and large values of  $Q$  will be desirable to minimize phase fluctuations occurring within the loop.

The evaluation of the signal generated by the oscillator and therefore the oscillator stability depends on two different aspects. The first one is the **short-term random fluctuation (or spectral purity) of the oscillation frequency**, which is usually quantified by the **phase noise**. And the second one is its long-term stability versus time, which is the degree of uniformity of the oscillator frequency over time and is limited by the aging of the oscillator elements. Finally, the phase noise is usually used to quantify the signal generated by an oscillator.

### 1.1.2. Oscillator phase noise

The phase noise is an important parameter to scale in order to evaluate the quality of a harmonic oscillator. An ideal oscillator would have a frequency spectrum consisting of a single delta function at its operating frequency (red line in **Fig. 1.1.3**), but a real oscillator presents a much wider spectrum (blue line in **Fig. 1.1.3**). It is because the generated signal is affected by many different random noises generated inside the

oscillator loop inducing amplitude, phase and frequency fluctuations. This in-loop noise is directly linked to the noise generated by the active element (the amplifier) and the selectivity of the filtering element. In a feedback oscillator, the phase fluctuations of the amplifier are directly converted into frequency fluctuations through the oscillator nonlinearity <sup>16</sup>. Let us introduce the main definitions allowing to quantify the noise in an oscillator signal and mainly the so-called phase noise.

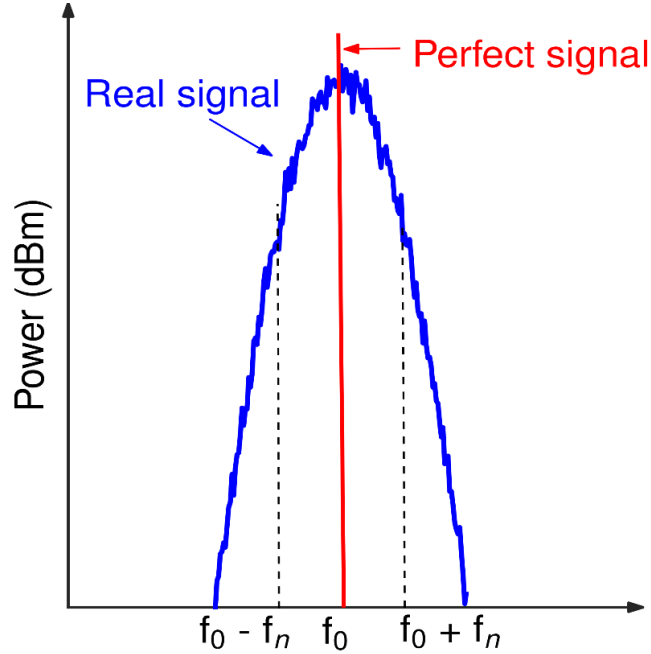


**Figure 1.1.3.** Power spectrum of the ideal and real signal generated by the oscillator. Red line: Perfect signal, Blue line: signal impacted by phase noise.

Consider the signal with only noise resulting from random phase fluctuations  $\varphi_n(t)$ .

$$\begin{aligned} V(t) &= V_0 \cos[2\pi f_0 t + \varphi_n(t)] \\ &= V_0 \{ \cos(2\pi f_0 t) \times \cos[\varphi_n(t)] - \sin(2\pi f_0 t) \times \sin[\varphi_n(t)] \} \end{aligned} \quad (1.1.7)$$

This phase fluctuation  $\varphi_n(t)$  induces frequency fluctuations:

$$f(t) = f_0 + \frac{1}{2\pi} \frac{d\varphi_n(t)}{dt} \quad (1.1.8)$$

The random phase fluctuation  $\varphi_n(t)$  is supposed here to have a wide frequency spectrum but an absolute value very small compared to 1. **Eq. (1.1.7)** can be rewritten as:

### 1.1. Oscillators

$$V(t) = V_0 \cos[2\pi f_0 t + \varphi_n(t)] \approx V_0 [\cos(2\pi f_0 t) - \sin(2\pi f_0 t) \varphi_n(t)] \quad (1.1.9)$$

By introducing the Fourier transform  $\Phi_n(\Delta f)$  of the random phase fluctuation  $\varphi_n(t)$  and changing  $\sin(2\pi f_0 t)$  and  $\cos(2\pi f_0 t)$  into their complex forms, **Eq.(1.1.9)** becomes:

$$V(t) = \frac{V_0}{2} \left\{ e^{j2\pi f_0 t} + j \int_{-\infty}^{\infty} [\Phi_n(f) e^{j2\pi(f_0+f)t}] df \right\} + \frac{V_0}{2} \left\{ e^{-j2\pi f_0 t} - j \int_{-\infty}^{\infty} [\Phi_n(f) e^{-j2\pi(f_0-f)t}] df \right\} \quad (1.1.10)$$

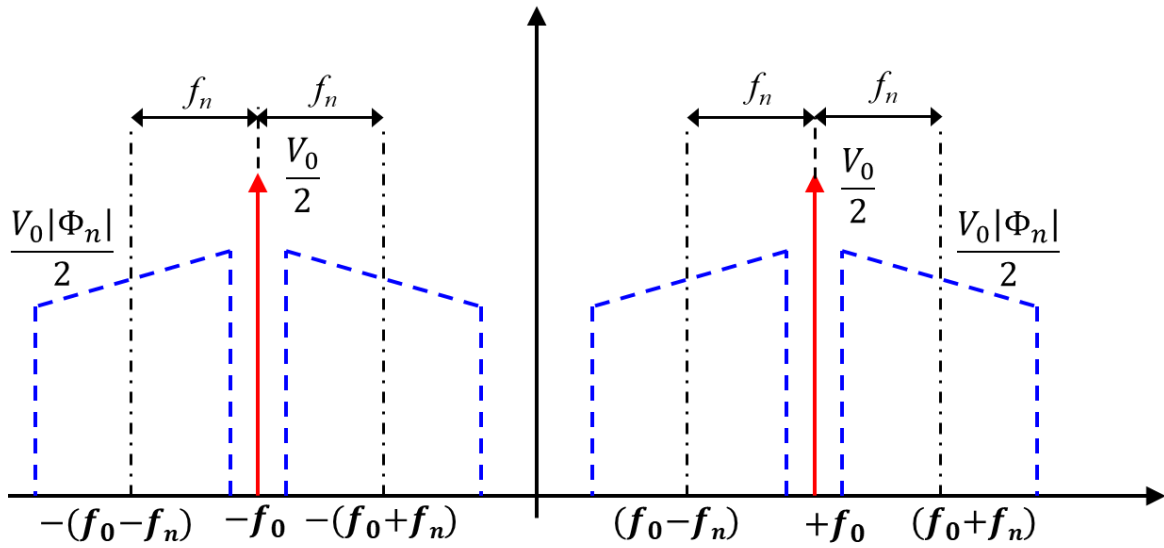


**Fig.1.1.4.** The impact of the phase noise into the spectrum of the oscillation signal.

**Fig. 1.1.4** plots the impact of the phase noise into the spectrum of the oscillation signal. Here,  $\frac{V_0^2}{2}$  is the power of the carrier and  $\frac{V_0^2}{2} |\Phi_n(\Delta f)|^2$  is the power in a frequency band of 1 Hz in one side of the carrier. The power repartition is considered by both positive and negative frequencies. In addition, from the Parseval theorem, it is known that  $|\Phi_n(f)|^2 = S_\varphi(f)$ , where  $S_\varphi(f)$  is the spectral power density of the phase fluctuations  $\varphi_n(t)$ , which is expressed in  $\text{rad}^2/\text{Hz}$ . Therefore, from the previous calculation, we can see that the power in a frequency band of 1 Hz in one side of the carrier can be written as  $\frac{V_0^2}{2} |\Phi_n(f)|^2 = \frac{V_0^2}{2} S_\varphi(f)$ .

The noise power expressed in dB at an offset frequency  $f_n$  from the carrier is so given by  $P_{\text{dB}} = 10 \log[|\Phi_n(f)|^2]$  or  $P_{\text{dB}} = 10 \log[S_\varphi(f)]$ .

This result lead to the first **definition of the phase noise**, which is defined as the ratio power in one phase modulation sideband to the total power per unit bandwidth (1 Hz) at a particular offset  $f_n$ , from the oscillation frequency  $f_0$ , and denoted as  $L(f_n)$  <sup>17</sup>.

$$L(f_n) = \frac{\text{Area of 1 Hz band width}}{\text{Total area under the curve}} \quad (1.1.11)$$

This definition was directly based on measurement and could be performed by a spectrum analyzer. However, this definition considers both amplitude and phase noise of the signal. In order to isolate the effect of phase fluctuation only, another definition has been introduced by an IEEE standard <sup>18,19</sup>, as one half of the double-sideband spectral density of phase fluctuation.

$$L(f_n) = \frac{1}{2} S_{\varphi}^{+}(f_n) \quad (1.1.12)$$

where  $S_{\varphi}^{+}(f_n) = 2S_{\varphi}(f_n)$  is the single band power spectrum density of the random phase noise fluctuations, i.e.  $S_{\varphi}(f) = |\Phi_n(f)|^2$ . When it is expressed in dB, the unit is noted dBc/Hz (the letter “c” meaning “from the carrier”).

It is also possible to introduce the frequency noise and the frequency spectral power density.  $S_f(f_n) = f^2 S_{\varphi}(f_n)$ .

Finally, it is mainly  $L(f_n)$  and  $S_{\varphi}(f_n)$  that are usually used in frequency metrology to specify the phase noise or the short-term stability of frequency standards.

There are two origins for non-perfect generated signals: noise components of known sources (electrical ~50 Hz, mechanical, acoustic...) that can be identified in a phase noise spectrum as noise peaks (called spurious peaks) and noise generated by multiple random fluctuations inside the oscillation loop. Some causes of these fluctuations are: thermal noise, white noise, flicker noise (characterized by its  $1/f$  noise slope) and high frequency noise. Because of these various origins, it is difficult to consider all the contributions for modelling the oscillator phase noise. Despite that, a simple and well-known analysis has been introduced by Leeson <sup>16</sup>, and known as the Leeson effect, in 1966 to describe the phase noise behavior in a classical oscillator.

As we have already seen before, let us consider a random phase fluctuation (produced by the amplifier or other sources)  $\psi_n(t)$  having a frequency spectrum. It

## 1.1. Oscillators

induces frequency fluctuations characterized by an offset with respect to the center oscillation frequency such as  $f_{osc} = f_0 + f_n$ . We then analyze the power spectral density of phase noise in 2 cases: when  $|f_n| < \frac{\Delta f}{2}$  (low  $Q$  filter) and when  $|f_n| > \frac{\Delta f}{2}$  (high  $Q$  filter).

**If  $|f_n| < \frac{\Delta f}{2}$  with  $\frac{\Delta f}{2} = \frac{f_0}{2Q}$**  : under the feedback loop, this frequency remains in the bandwidth of the microwave filter:

$$f \in \left[ f_0 - \frac{\Delta f}{2}, f_0 + \frac{\Delta f}{2} \right]$$

We then find again the result of section **1.1.1**:  $\delta\omega_n = \frac{\omega_0}{2Q}\psi_n$  or  $f_n = \frac{f_0}{2Q}\psi_n(t)$ .

The output frequency fluctuation therefore can be rewritten as:

$$f(t) = f_0 + \frac{f_0}{2Q}\psi_n(t) \quad (1.1.13)$$

From Eq. (1.1.8) and Eq. (1.1.13) we have:

$$\frac{d\varphi_n(t)}{dt} = \frac{\omega_0}{2Q}\psi_n(t) \text{ or } \varphi_n(t) = \frac{\omega_0}{2Q} \int \psi_n(t) dt \quad (1.1.14)$$

Moving to the phase noise as previously introduced and from the formula concerning the Fourier transform about derivative calculation:

$$S_{\varphi_n}(f_n) = \frac{1}{\omega^2} S_{\delta\omega_n}(f_n) = \frac{1}{(2\pi f)^2} \left( \frac{\omega_0}{2Q} \right)^2 S_{\psi_n}(f_n)$$

$$\text{so } S_{\varphi_n}(f_n) = \frac{1}{f_n^2} \left( \frac{f_0}{2Q} \right)^2 S_{\psi_n}(f_n).$$

**If  $|f_n| > \frac{\Delta f}{2}$**  : in this case, the frequencies  $f = f_0 \pm f_n$  are totally filtered, the feedback loop has no effect and the phase fluctuations can be found at the output. Therefore,  $\varphi_n(t) = \psi_n(t)$  and so:  $S_{\varphi}(f_n) = S_{\psi}(f_n)$ .

To summarize both cases we can write the formula, known as the Leeson formula:

$$S_{\varphi}(f_n) = S_{\psi}(f_n) \left[ 1 + \frac{1}{f_n^2} \left( \frac{f_0}{2Q} \right)^2 \right] = S_{\psi}(f_n) \left[ 1 + \frac{f_L^2}{f_n^2} \right] \quad (1.1.15)$$

$f_L = \frac{f_0}{2Q}$  is called the Leeson frequency. **Eq. (1.1.15)** clearly indicates that **to obtain a low phase noise** it is necessary to have a low value of  $f_L$  corresponding to a **high value of the quality factor  $Q$** .

In case of only white noise at the output of the amplifier  $S_\psi(f_n) = S_{\psi_0}$ , we obtain:

$$S_\varphi(f_n) = S_{\psi_0} \left[ 1 + \frac{f_L^2}{f_n^2} \right] \quad (1.1.15b)$$

But for a general noisy amplifier there will be at its output white noise at higher values of the frequency and flicker noise (or  $1/f$  noise) at lower values, the limit between these two kinds of noise being noted as  $f_c$  (called corner frequency). In this case it is necessary to consider the order of magnitude of the quality factor  $Q$  and we shall discuss for the offset frequency decreasing from "high" value down to zero. At high frequencies, the noise is predominantly white, constant with frequency. At lower frequencies there is mainly flicker noise.

- Case of a low  $Q$  which means  $f_L > f_c$ : for  $|f_n| > f_L$  there is only white noise and  $S_\varphi(f_n) = S_{\psi_0}$ , then for  $f_c < |f_n| < f_L$  there is a slope of  $\frac{1}{f_n^2}$ , and finally for low offset frequencies flicker noise is the most important and the slope is  $\frac{1}{f_n^3}$ .
- Case of a high  $Q$  which means  $f_L < f_c$ : if  $|f_n| > f_c$  there is once again only white noise and  $S_\varphi(f_n) = S_{\psi_0}$ , then for  $f_L < |f_n| < f_c$  there will be flicker noise the output phase noise has a slope  $\frac{1}{f_n}$ , and finally for the very low offset frequencies, smaller than the Leeson frequency  $|f_n| < f_L$  the slope is  $\frac{1}{f_n^3}$ .

These results are summarized in the **Figure 1.1.5** plotting the power spectral density of phase noise as a function of the offset frequency for both cases low  $Q$  and high  $Q$ . In both cases, for frequencies very close to the carrier at  $f_0$ , the noise power decrease as  $\frac{1}{f_n^3}$ . If the microwave filter has a relative low  $Q$ , then from frequency between corner frequency and Leeson frequency,  $f_c < |f_n| < f_L$ , the noise power

## 1.1. Oscillators

drops as  $\frac{1}{f_n^2}$ . If the microwave filter has a relative high  $Q$ , then from frequency between Leeson frequency and corner frequency  $f_L < |f_n| < f_c$  the noise power drops as  $\frac{1}{f_n}$ .

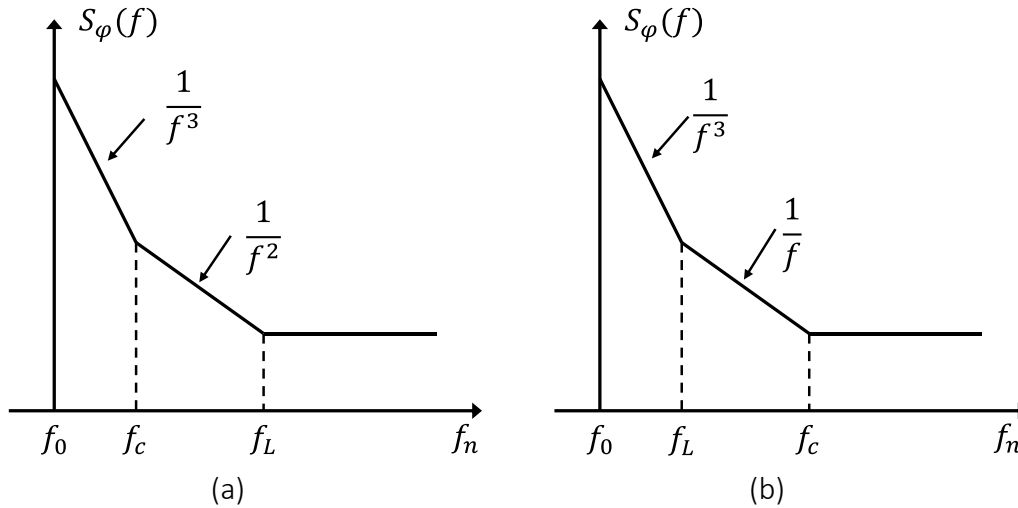


**Figure 1.1.5.** Power spectral density of phase noise at the output of an oscillator. (a)  $f_n < \Delta f/2$  (low  $Q$ ) and (b)  $f_n > \Delta f/2$  (high  $Q$ ).

### 1.1.3. Passive component of choice for microwave oscillators

Microwave oscillators can be divided into many different types based on frequency bandwidths, type of active devices or passive devices (RF filter). Among them, the RF filter mainly affects to the cost, frequency tuning range, stability, sensitivity and noise performance of the oscillator, and therefore is commonly used to define different types of oscillators <sup>15</sup>. In most of general cases, the RF filter is determined by the microwave resonator used, the quality factor of the filter is defined in **Eq. (1.1.4)**. From **Eq. (1.1.15)**, it is easy to see that **the oscillator phase's fluctuation is inversely proportional to the microwave resonator's loaded quality factor**. A high microwave resonator quality factor thus leads to less fluctuations of the oscillation signal. Many types of high  $Q$  microwave resonators used for the stabilization of the electronic oscillator can be used, such as electro-mechanical (piezo-electrical) resonators, i.e. quartz crystals, electromagnetic resonators, i.e. dielectric cavities and acoustic and

electrical delay lines. The choice of the resonator is generally determined by a variety of factors, but for the highest achievable  $Q$  at room temperature, the crystal quartz is the best choice for the stabilization of electronic oscillators<sup>14</sup>. However, they have limited range of frequency tunability (from 32.7 kHz to some hundreds of MHz)<sup>20</sup>, therefore they cannot be directly used to generate high frequency signals. In order to reach higher frequencies, a popular approach is to produce a harmonic of a lower frequency oscillator through the use of a frequency multiplier<sup>17</sup> by using reactive diode multipliers, resistive diode multipliers, or transistor multipliers. But the main disadvantage of this approach is that noise level is increased with the multiplication factor  $M$ , by  $10\log_{10}(M^2)$ . This is because frequency multiplication is effectively a phase multiplication process as well, so phase noise variations get multiplied in the same way that frequency is multiplied. For this reason, **a new type of oscillator with significantly low noise and very high stability, as well as high application frequency is expected.** This goal can be achieved by embedding optical technology into traditional electrical systems, which can bring advantages in low loss, light weight, high frequency operation and immunity to electromagnetic interferences. This is the idea behind the invention of the opto-electronic oscillator (OEO) system.

## 1.2. OEO based on delay line

The first microwave oscillator using optical components was first introduced in 1982 by Neyer and Voges<sup>21</sup>. Then, in 1991 R. Logan et al.<sup>22</sup> from NASA's Jet Propulsion Laboratory (JPL) published a paper introducing the so-called fiber optic stabilized electronic oscillator (FOSO), with the idea to improve phase stabilization based on an optical fiber delay line. This oscillator after that was improved by Logan's colleague in 1994<sup>2,23</sup>, using kilometers-long optical fiber delay line, and called opto-electronic oscillator (OEO) system. Up to now, after more than 20 years of development, OEO has been spreading into research laboratories and entering into real-world applications, ranging from aerospace to telecommunications to instrumentation and even sensing. In the following of this manuscript, starting from OEO based on delay

line, we will explain the advantages of the system and how can it can overcome the limitations of traditional microwave oscillators.

### 1.2.1. Principle of operation of OEO based on delay line

The OEO became to be popular after the paper of X. S. Yao and L. Maleki in 1994<sup>2</sup>; it is known to provide spectrally pure and stable microwave and millimeter-wave (mm-W) signals with a great potential for applications in communications, radars or sensing<sup>23</sup>. A classical OEO comprises a stable continuous wave light source, a fast light intensity modulator, a kilometer-long optical fiber delay line and a fast quadratic photo-detector. Albeit the hybrid nature of the system loop, the OEO structure principle of operation relies on a classical Barkhausen-like oscillation condition when feeding the detector output signal onto the optical modulator radio-frequency (RF) input to close the loop (Fig.1.2.1).

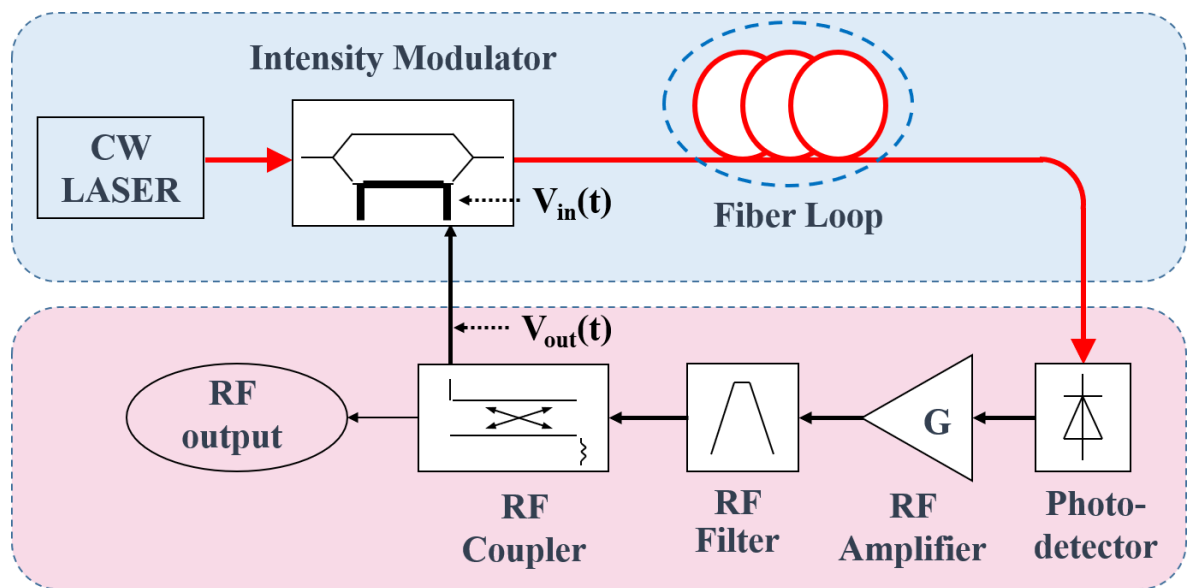


Fig 1.2.1. Basic scheme of an opto-electronic oscillator (OEO).

The OEO starts with the laser light beam which is modulated by an intensity modulator before to be sent into a long length optical fiber. This optical fiber is used to create a delay but can also be considered as storing energy inside the system. At the output of the fiber, the modulated signal arrives on a photodetector to be converted into

### 1.2.1. Principle of operation of OEO based on delay line

a microwave signal at frequency  $f_{osc}$ . It is then amplified and coupled back to the modulator for closing the loop.

The OEO feedback loop can generate self-sustained oscillations if its overall gain is larger than 1, and the waves circulating in it add up in phase <sup>3,23</sup>. The former requirement can be met with insertion of gain in the loop and, the latter, by controlling the phase. The phase oscillation condition allows to determine the oscillation frequency. Considering the effect of the fiber as introducing a pure delay (neglecting its attenuation), its transfer function can be written as:  $\underline{H}(j\omega) = e^{-j\tau_p\omega}$  where  $\tau_p$  is the propagation time in the fiber. If the propagation time in the electronic components of the system can be neglected, the global propagation time in the loop is equal to  $\tau_p$ . From the oscillation phase condition (see section **I.1.1**) we have:  $\omega_{osc}\tau_p = k \cdot 2\pi$  ( $k$  being an integer), where  $\tau_p = \frac{n_{eff}L_{fiber}}{c_0}$  (**1.2.1**),  $L_{fiber}$  being the length of the fiber and  $n_{eff}$  its effective index ( $n_{eff} = 1.44$ ) and  $c_0$  the light velocity in vacuum ( $c_0 = 3 \times 10^8$ ).

So, the possible oscillation frequencies can be written as:

$$f_{osc} = k \frac{c_0}{n_{eff}L_{fiber}} \quad (1.2.2)$$

The OEO with such a structure can have many oscillation modes. To select the desired frequency at the output of the oscillator, a microwave filter must be added in the feedback loop. By this way any frequency supported by the bandwidth of the component can be generated under the oscillation conditions.

This system differs from the previous oscillator circuits by making use of very low loss optical fiber delay line (0.2 dB/km) as a key element to create high quality factor component for the oscillator producing a signal which is characterized by its high spectral purity. The equivalent  $Q_{fiber}$  in the long fiber delay line can be written as <sup>23</sup>:

$$Q_{fiber} = \pi f_0 \tau_p = \pi f_0 \frac{L_{fiber} n_{eff}}{c_0} \quad (1.2.3)$$

Clearly,  $Q_{fiber}$  increases when the fiber length increases. For an OEO including a 10 km fiber delay line and operating at 10 GHz frequency, the equivalent  $Q_{fiber}$  inside the fiber is around  $1.5 \times 10^6$ .

## 1.2.2. Analytical study of the OEO

In the OEO, the electro-optic modulator (EOM) is a key element as a transducer from RF to optical domain. The second transducer in the system is the photodiode which works usually with a linear behavior, which is not the case of the EOM.

Theoretically, considering a Mach-Zehnder interferometer, the optical power at the E/O modulator's output is related to an AC applied voltage  $V_{in}(t)$  by:

$$P(t) = \frac{\alpha P_0}{2} \left\{ 1 + \eta \cos \left[ \pi \left( \frac{V_{in}(t)}{V_\pi} + \frac{V_0}{V_\pi} \right) \right] \right\} \quad (1.2.4)$$

where  $\alpha$  is the fractional insertion loss of the modulator,  $P_0$  is the input optical power,  $V_0$  is a constant voltage,  $V_\pi$  is its half-wave voltage of the modulator, and  $\eta$  determines the extinction ratio of the modulator given by  $(1+\eta)/(1-\eta)$ .

After propagation in the optical fiber, the signal  $P(t)$  is converted into an electrical signal by the photodetector, which gives after going through an RF amplifier an output electrical signal expressed as <sup>23,24</sup>:

$$V_{out}(t) = P(t) \rho R G_A = V_{ph} \left\{ 1 + \eta \cos \left[ \pi \left( \frac{V_{in}(t)}{V_\pi} + \frac{V_0}{V_\pi} \right) \right] \right\} \quad (1.2.5)$$

where  $V_{ph} = I_{ph} R G_A$  is the voltage generated at the output of the amplifier,  $R$  is the load impedance of the detector,  $G_A$  is the amplifier's voltage gain, and  $I_{ph} = \frac{\alpha P_0 \rho}{2}$  is the detected photocurrent where  $\rho$  is the responsivity of the detector.

**Eq. (1.2.5)** is nonlinear but can be linearized if we force the signal through the narrow band pass filter to block all harmonic components <sup>23</sup>. The result then allows to calculate the spectral power density of the oscillator. The details of this calculation are given in refs. <sup>14,23</sup>. From this calculation, we have:

$$S_{f_{osc}}(f_n) = \frac{\delta}{(\delta/2\tau_p)^2 + (2\tau_p)^2(\tau_p f_n)} \quad (1.2.6)$$

$\delta$  being the signal to noise ratio of the OEO defined as:

$$\delta = \frac{\rho_N G_A^2}{P_{osc}} = \frac{[4k_B T e q(NF) + 2q_e I_{ph} R + N_{RIN} I_{ph}^2 R] G_A^2}{P_{osc}} \quad (1.2.7)$$

### 1.2.1. Principle of operation of OEO based on delay line

where  $\rho_N$  is the total noise density input to the oscillator and is the sum of the thermal noise of the amplifier, i.e.  $\rho_{th,A} = 4k_B T_{eq}(NF)$  expressed here with the equivalent noise

temperature depending on the noise figure  $NF$  of the amplifier, the shot noise from the photodetector  $\rho_{shot} = 2eI_{ph}R$  and the laser's relative intensity noise (RIN)  $\rho_{RIN} = N_{RIN}I_{ph}^2R$ . In **Eq. (1.2.7)**,  $k_B$  is the Boltzman constant,  $q_e$  is the electron charge,  $I_{ph}$  is the photocurrent across the load resistor of the photodetector, and  $N_{RIN}$  is the RIN noise of the pump laser.

It is noteworthy that **Eq. (1.2.7)** does not contain the oscillation frequency. This is basically denoting an important feature of the OEO: **the phase noise of an OEO is fixed and is the same for any generated frequency**. This feature can be interpreted as: Unlike the behavior of classical microwave oscillators where the noise figure increases with the working frequency, the OEO can thus provide signals at high frequency without any degradation of its phase noise properties.

From **Eq. (1.2.6)**, we also see that the spectral power density is influenced by the delay time  $\tau_p$  which is proportional to the fiber length as described by **Eq. (1.2.1)**. So evidently the noise can be reduced by any desired amount by simply lengthening the fiber. The state of the art showing OEO with a phase noise of -163 dBc/Hz at 6 kHz offset frequency from 10 GHz carrier has been obtained with a 16 km long fiber<sup>25</sup>. This performance was limited by the Flicker noise of the photo-detector used inside the loop.

To summarize, the main idea behind the OEO is to use a long length optical fiber with extremely low loss in order to obtain directly a high oscillation frequency with a very low phase noise. This is not possible with an electronic microwave oscillator. This first structure proposed for OEOs is indeed facing some problems mainly coming from the use of a long fiber delay line, leading to a lack of compactness and integration of the entire system.

### 1.2.3. Drawbacks of classical OEO

As described above, one of the features of OEOs is that many frequencies are supported in the loop, being associated with the optical fiber length as indicated in **Eq. (1.2.2)**. The distance between two modes is the mode spacing and so-called the Free Spectral Range of the oscillator and is noted  $FSR_{osc}$ . It depends on the effective refractive index  $n_{eff}$  of the fiber, the global length  $L_{fiber}$  of the fiber loop, and the light velocity in vacuum  $c_0$ .

$$\Delta f = FSR_{osc} = \frac{c_0}{n_{eff}L_{fiber}} \quad (1.2.8)$$

An example of the oscillation spectrum generated by a fiber based OEO can be seen in **Fig.1.2.2**. On both sides of the center frequency at 18.003 GHz corresponding to the oscillation frequency, other peaks at a distance of 134 kHz are visible, in good agreement with **Eq. (1.2.8)** taking into account  $L_{fiber} = 1.5$  km. These multi-modes oscillations raise problems related to the starting conditions of the oscillations (which mode wins the competition is not firmly prescribed) and is also responsible for mode hopping between the different loop modes during the full-CW operation (i.e. frequency instability).

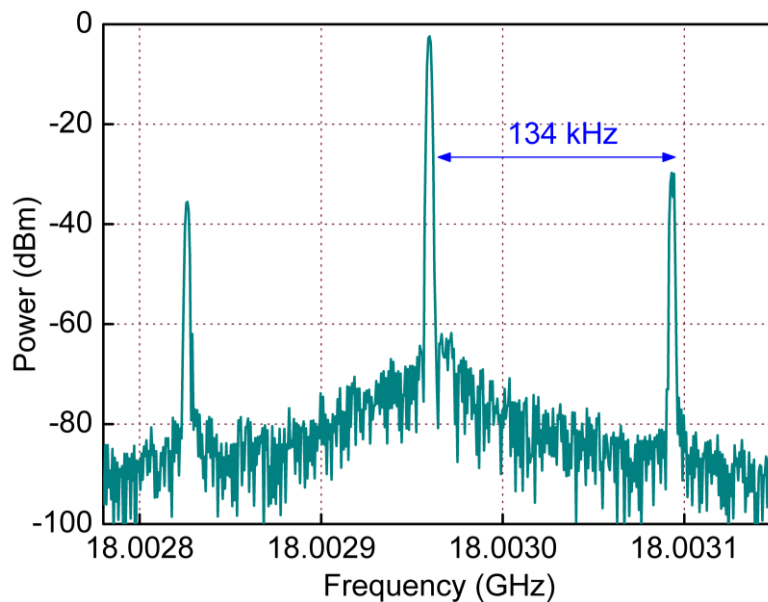


**Fig.1.2.2.** Example of oscillator spectrum, at 18 GHz, with a fiber length of 1.5 km. The oscillator FSR is approximately 134 kHz (only).

From previous discussion about the effects of the optical fiber length on both the quality factor and the free spectral range, we can see that a **trade-off appears** between a long fiber for a **great quality factor** and a **short one** for having a **single mode oscillation** and so to **avoid possible mode hopping**.

The first solution used to suppress this multi-mode behavior is to consider an RF filter with a bandwidth narrow enough for selecting only one oscillation frequency. For

example, as mentioned above, for an OEO using 1.5 km fiber, multi-mode oscillation can be created with a  $FSR_{osc}$  as small as 134 kHz. In order to suppress this behavior, a RF filter with the bandwidth smaller than 134 kHz is required. That means the desired RF filter should have a quality factor larger than 135 000 (for 18 GHz oscillation frequency). A filter with such bandwidth is difficult to realize, especially when the length of the fiber is long, and the operation frequency is in the microwave and mm-wave range. Moreover, the RF filter bandwidth must be further decreased if the fiber length increases. Therefore, in general cases, many spurious modes still pass through the RF filter under the oscillation condition of the loop. The oscillator then can start at different frequencies each time the loop is closed, which is obviously a drawback.

Another issue is also related to the optical fiber refractive index dependence on the temperature. The effective refractive index  $n_{eff}$  of a typical single mode fiber (silica) has nearly linear dependence on temperature (T) with a slope of  $\Delta n_{eff}/\Delta T \sim 1.2 \times 10^{-5} / ^\circ\text{C}$  in the temperature range between  $-60$  to  $85$   $^\circ\text{C}$  <sup>26</sup>. Hence, the OEO has a carrier frequency variation depending on temperature given by:

$$\frac{\Delta f}{\Delta T} = - \frac{f}{n_{eff}} \frac{\Delta n_{eff}}{\Delta T} \quad (1.2.9)$$

For a 10 GHz carrier, the temperature variation results in frequency drift around 83 kHz/ $^\circ\text{C}$ . To avoid this possible oscillation frequency drift, the optical fiber delay line should be placed into a temperature-controlled box, which makes the system become bulky.

To conclude, the need for long length optical fiber leads to some major challenges to the OEO stability, mainly due to mode hopping and temperature fluctuations in the

## 1.2. OEO based on delay line

fiber<sup>3</sup>. While the latter can be addressed by using a bulky temperature control system, the former is still difficult to solve.

Many works have aimed at reducing or remove this multi-mode behavior while keeping at the same time generated signal spectral purity. The most popular well-known approach is based on the use of multi-loop OEO configurations, either relying on dual-loop<sup>27–32</sup> or master/slave OEOs<sup>33–35</sup>. In the dual-loop OEO, two feedback loops with different fiber lengths are used. The possible oscillation frequencies must add up in phase after each round trip. The modes from each loop which are the closest to each other can lock and suppress the other cavity modes. In this configuration, the mode spacing is dictated by the shorter loop, resulting in an oscillator having large mode spacing. The trade-off of this system comes from the phase noise, which is now an average of the noise levels of the two loops individually, i.e. degraded compared to what we have with a long single loop<sup>28</sup>. In addition, since both loops support side modes, these modes are not completely eliminated, but merely nearly suppressed<sup>29</sup>. Similar to the dual-loop OEO, the master/slave OEO makes use of an OEO with a longer fiber for a master OEO and a shorter one for a slave OEO. The RF signal from the master OEO is injected into the slave one to lock the oscillation frequency and phase. The length of the slave OEO's optical fiber is chosen such that only one mode is allowed within the RF-filter in that single loop OEO, therefore, suppressing the spurious modes from the master OEO by the destructive interference in the slave OEO's cavity. None like the dual-loop OEO, the phase noise, in this case, is fixed by the long fiber loop of the master OEO. A comparison of the best OEO in term of phase noise performances for different configurations is given in **Table 1.2.1**

**Table 1.2.1.** Different types of OEO based on delay line and their performances.

Type of OEO	Fiber length (km)	Oscillation frequency $f_{osc}$ (GHz)	Phase noise (dBc/Hz)	FSR <sub>osc</sub> (kHz)
Single fiber delay line <sup>25</sup>	16 km	10	-163 dBc/Hz @ 6 kHz	13
Dual-loop <sup>36</sup>	1 km/100m	10	-144.7 dBc/Hz	> 100

			@ 10 kHz	
Master/slave <sup>34</sup>	4 km/547 m	10	-140 dBc/Hz @ 10 kHz	354

From **table 1.2.1**, it can be seen that the multi-loop OEO based on either a dual-loop configuration or a master/slave one gives possible ways to reduce the aforementioned multi-mode behavior of classical OEOs while keeping a low phase noise level. However, with a second section of fiber makes the system even more bulky. Another solution to improve the performances of OEOs is to replace the fiber delay line by a high-quality factor optical resonator. This solution will be discussed in detail in section 1.3 of this chapter.

Although the disadvantage in spurious mode and mode hopping effects that need to be improved, OEO with its advantage of self-generating continuous-wave microwave frequency with ultra-low phase noise, has been used in widespread applications in diverse fields of science and technology ranging from metrology to communication, sensing, satellite and radar systems.

## 1.2.4. Applications of the opto-electronic oscillator

Due to its unique characteristics, OEOs are used in many applications where traditional microwave oscillators cannot meet the requirements of low phase noise. The two outstanding applications of OEO are: RF/optical generation and sensing detection.

### 1.2.4a. RF/optical signal generation

As mentioned before, OEO has been invented to generate high-frequency oscillation signals with low phase noise. Therefore, since the first invented in 1994, OEO has been indicated as a promising objective in the RF/optical signal generation domain. The system has been used for some high-end technology applications where the ultra-pure signal is extremely important. For example, since OEO has the ability of generating tens of gigahertz low of phase noise microwave signals with great flexibility, being mainly limited by the bandwidths of the electrical and optoelectronic employed

## 1.2. OEO based on delay line

devices. It has been employed in payload satellites or military radars <sup>37–39</sup> where transmitted and received signals are required together with broadband operator and low phase noise. Moreover, OEO can be very compact if an ultrahigh- $Q$  whispering-gallery-mode resonator is used to replace the long length optical fiber. Remarkably, an ultra-compact OEO package smaller than a coin was reported previously <sup>3,39</sup> with a phase noise of -108 dBc/Hz at 10 kHz offset, demonstrating the significant potential of this system for deployment in satellite payloads and military radars. In addition, OEO was proposed for application in satellite telemetry and control <sup>40</sup>.

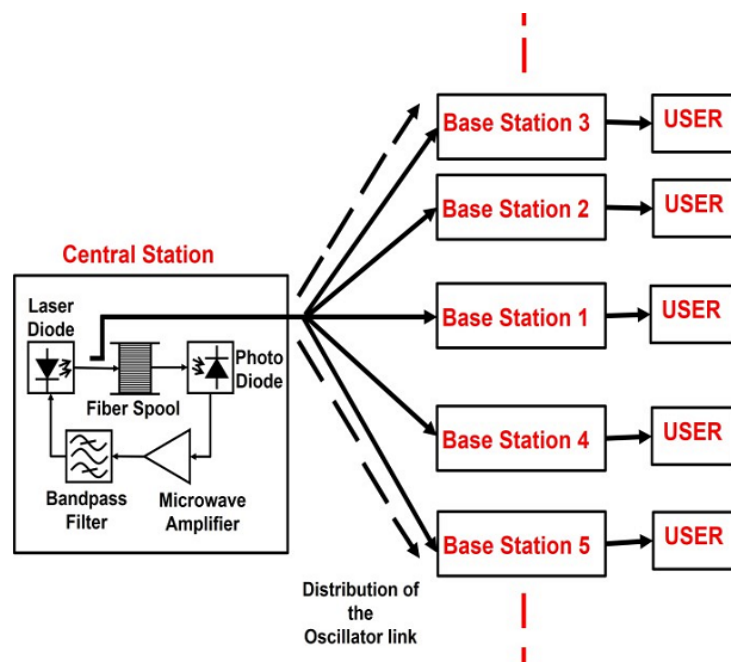


**Fig 1.2.5.** Main idea of the implementation of the OEO in the 5G Mobile and Wireless Networks <sup>41</sup>. A low phase oscillator signal is distributed to the base stations from a central station via one optical link. The number of base stations which benefit from the oscillator line depends on several parameters of the OEO and on the conditions of the central station.

Moreover, the exponential increase in mobile data traffic is considered to be a critical driver towards the new era, or 5G, of mobile wireless networks, using mm-W signal <sup>41–44</sup>. The 5G networks lie in providing very high data rates, extremely low latency, manifold increase in a base station. To meet these promising abilities, a mm-W source with high spectral purity, frequency tunability, a drastic reduction in size, weight and cost is required <sup>42</sup>. Those requirements are matching some of the OEO features, making the OEO a possible solution of choice in this domain. **Fig 1.2.5** describes the

main idea of the implementation of an OEO as a central station for 5G networks, by removing the local oscillator from the base-station and placing OEO on the center station<sup>41</sup>. By this way, OEO could feed a large number of base stations and thereby divide the costs of the OEO signal generation between many stations. Moreover, the oscillation signal could be distributed to many stations with a high bit rate and low latency.

### 1.2.4b. Applications to sensing

Besides the features on the RF/optical signal generation, a signal generated by an OEO has a great potential for sensing applications. In this option, the target parameter or signal to be measured is converted to a frequency shift of the oscillation signal<sup>45,46</sup>. Then, an analysis of the oscillation frequency in the electrical domain allows to retrieve the target parameter. Moreover, the generated signal from the OEO is characterized by a narrow linewidth and low phase noise, such that an analysis on the oscillating frequency leads to high resolution and high signal to noise ratio (SNR). Diverse applications to sensing, measurement, and detection have already been demonstrated by using OEO<sup>45-53</sup>.

The OEO based sensing schemes rely on the perturbation of the oscillation frequency and  $FSR_{OEO}$  due to a variation of the time delay  $\Delta\tau_p$  of the loop. This time delay actually reflects the change of the effective loop length:  $c\Delta\tau_p = n_{eff}\Delta L + L\Delta n_{eff}$ ,  $n_{eff}$  and  $\Delta n_{eff}$  being the mode effective refractive index and its change, and  $L$  and  $\Delta L$  the loop physical length and its change. By measuring the change of the oscillation frequency, any impact contributing to the physical length and the effective refractive index can be measured. Examples of OEO based sensing based on this principle can be found in previous articles<sup>47-50,52</sup>, and were applied to optical length changes<sup>47</sup>, distance measurements<sup>48</sup>, temperature<sup>49,50</sup> and refractive index<sup>52</sup> detections. In another configuration, a high  $Q$  optical filter was introduced in the OEO loop for implementing a microwave photonic filter (MPF) (see section 1.3 of this chapter), leading to similar sensing applications<sup>45,51 53,54</sup>.

In summary, various applications of the OEO system in different domains have been discussed, showing its importance for the research community and maybe in the

future for the commercial sector. However, a critical limitation lies on the bulk size of the system and on a detrimental mode hopping (mainly due to long fiber length). An alternative solution to solve these issues is to replace the optical fiber delay line by a high  $Q$  optical element, it can help to reduce the system's size and avoid mode hopping. For this purpose, introducing an optical resonator presents interesting properties.

### 1.3. OEO based on optical resonator

An elegant solution has been proposed to overcome previous drawbacks of OEOs by replacing the optical fiber spool by an optical resonator <sup>3</sup>. In such direction, many kinds of optical elements such as Fabry-Perot etalon <sup>4,55-57</sup>, fiber ring resonators <sup>6,58</sup> and Whispering-Gallery Mode (WGM) based resonators <sup>59-61</sup> were considered.

#### 1.3.1. Principle of operation

A typical configuration of the OEO based on an optical resonator is shown in Fig.1.3.1.

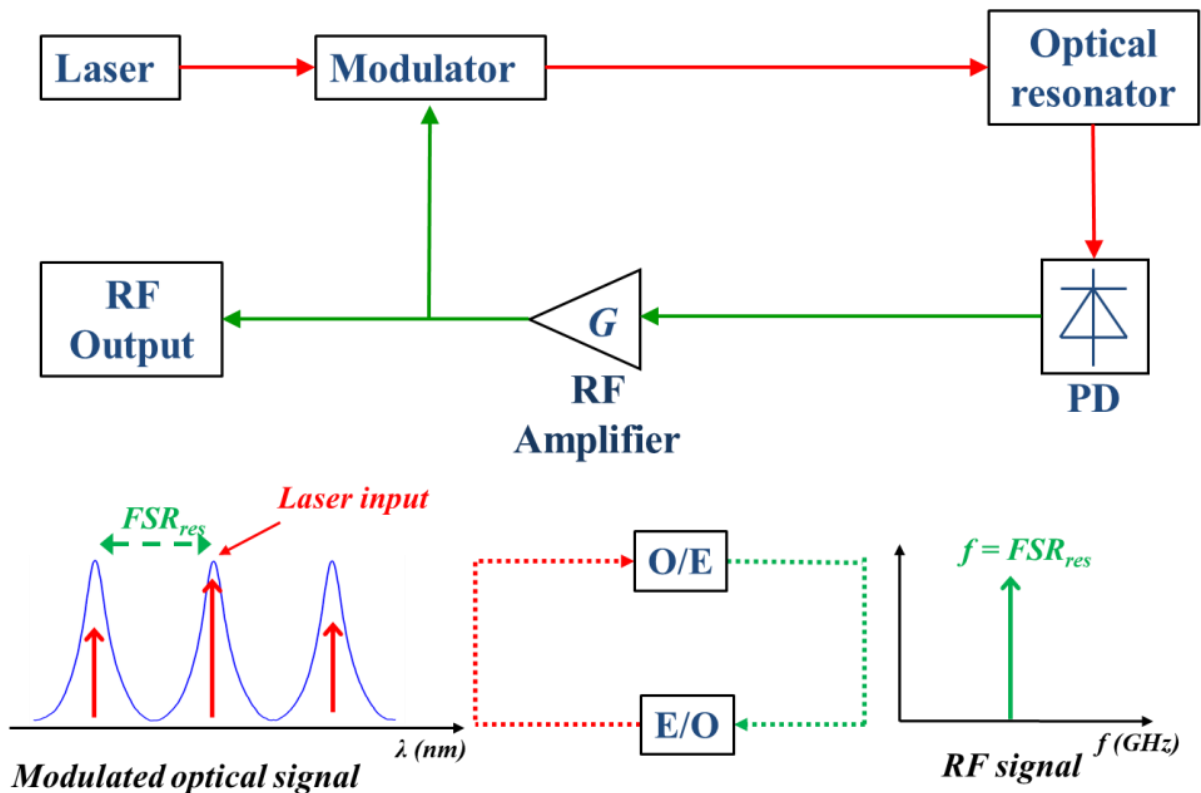


**Fig.1.3.1.** Schematic configuration of the OEO based on optical resonator (top) (PD: photo-detector) and working principle of the system (bottom).

In this OEO structure, the optical signal at the output of a continuous wave laser is modulated by an intensity modulator before being coupled into a multimode optical resonator with several comb line transmissions. An optical/RF conversion using a quadratic conversion based on a photo-detector is then implemented by taking the beating of two adjacent resonance frequencies passing through the resonator transfer function. One of the most classical solution to achieve this operation is based on the use of an optical cavity having a comb of optical resonance frequencies spaced apart by a free spectral range ( $FSR_{res}$ ), e.g. a Fabry-Perot or a ring cavity. This process, in essence, relies on using a periodical optical spectrum at the output of the resonator to create a microwave signal, thus selecting the microwave frequency corresponding to the free spectral range of the resonator ( $FSR_{res}$ ). The converted signal after being amplified by an RF amplifier to enable sufficient gain for the loop is sent back to the modulator to close it. The schematic working principle of this configuration is illustrated in the bottom part of **Fig.1.3.1**. To obtain the oscillation condition, the laser frequency must match one of the transmission peaks of the optical resonator and the free spectral range of the resonator ( $FSR_{res}$ ) also needs to belong to the microwave domain. The oscillation frequency of the system is proportional to the  $FSR_{res}$  of the resonator.

$$f_{osc} = k * FSR_{res} \quad (1.3.1)$$

where  $k$  is a positive integer. Because a small cavity length of the resonator can be made in order to enlarge the mode spacing of the oscillation frequency, an easy selection of one single mode for the oscillator by the microwave filter can be done. Thus, the purpose of the microwave bandpass filter in this configuration is to reject the RF signal outside the frequency band of interest, and not to perform narrow band-filtering like in a conventional OEO based on a delay line. With the small size resonator which can provide  $FSR_{res}$  in the GHz range, no microwave filter at all is theoretically required, although it could be interesting to add one for limiting the noise level injected into the modulator. The use of an optical resonator brings a great help in reducing the size of the OEOs, obviating the need for bulky temperature control systems and high-performance RF filters, making the loop more easily oscillate on only one oscillation mode and

### 1.3. OEO based on optical resonator

avoiding mode hopping. This solution changes the oscillator system nature from a delay line oscillator to an optical resonator oscillator one, making the introduced optical resonator a key element for the closed loop. Up to now, many types of optical resonators have been developed to be used in this purpose.

#### 1.3.2. Optical resonator in the OEO system

An optical resonator can be realized in different configurations, sizes and forms. Among the most well-known high optical quality factor resonators, there are Fabry-Perot etalon <sup>4,55–57</sup>, fiber ring resonators <sup>6,58</sup> and Whispering-Gallery Mode (WGM) resonators<sup>59–63</sup>.

##### 1.3.2a. Fabry-Perot etalons

A Fabry-Perot (FP) resonator is basically realized with two highly reflecting mirrors maintained in parallel. For an application to the OEO, a high-finesse FP was used as the mode selector in Refs <sup>55,56</sup>. Kim and Cho<sup>56</sup> reported a 41.5 mm length FP cavity with an  $FSR_{res}$  of 3.61 GHz. In another work, Ozdur *et al.*<sup>55</sup> used a 1000 finesse curved-curved FP etalon to generated 10.287 GHz RF filter with a  $FWHM$  of 13 MHz, the resulting OEO showing lower phase noise and higher RF stability compared to the similar system based on the fiber delay line. Similarly with Ozdur's work, a 100 000 finesse FP etalon with a 1.5 GHz  $FSR_{res}$  was used in the OEO <sup>4</sup>. By doing so, the authors obtained an oscillation frequency of 10.5 GHz with a low phase noise at -120 dBc/Hz at 10 kHz offset frequency from the microwave carrier. Moreover, one year later, this group achieved oscillations at tunable oscillation frequency in the 6 to 60 GHz range<sup>57</sup>.

##### 1.3.2b. Fiber ring resonators

Another kind of optical resonator featuring high optical quality factor is the fiber ring resonator (FRR). The FRR takes advantage of the low loss of optical fibers to provide an ultra-high optical quality factor ( $\gg 10^6$ ). It is realized using two symmetrical and low loss directional couplers, linked with single mode polarization maintaining optical fibers. In the reported OEO based on FRR <sup>6,58</sup>, FRR were realized with different fiber lengths, i.e. 10 m, 20 m and 100 m, the corresponding optical quality factors being

### *1.3.2. Optical resonator in the OEO system*

$2 \times 10^8$ ,  $5.1 \times 10^9$  and  $2 \times 10^9$ , respectively. In the experimental setup, a laser Pound-Drever-Hall (PDH) stabilization loop was used to stabilize the laser frequency to one of the resonator's resonance peaks. The setup provided a signal with a frequency spacing equal to the FSR

### 1.3. OEO based on optical resonator

of the fiber ring resonator. The related phase noise results were -90dBc/Hz and -128 dBc/Hz at 10 kHz offset frequency for 10 m and 100 m long passive cavities, respectively (and a 10 GHz oscillation frequency).

#### 1.3.2c. Whispering-Gallery mode resonators (WGM)

Another attractive class of optical resonators is the Whispering Gallery Mode (WGM) resonators, in which light is trapped in a circling orbit supported by total internal reflection at the boundaries of the structure. WGM can be realized in different geometry structures (micro-spheres, micro-disks, micro-toroidals) in different materials such as silicon, fused silica, Calcium Fluoride, Magnesium Fluoride or lithium tantalate <sup>59</sup>.

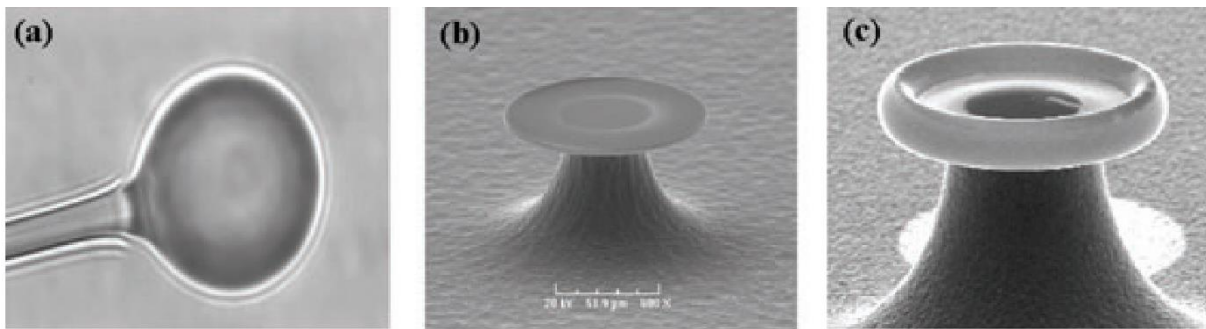


**Fig.1.3.2.** Three of the most common types of WGM resonators: (a) a microsphere, (b) a micro disk, (c) a microtoroid <sup>59</sup>.

One example of a OEO based on a  $10^8$  optical quality factor WGM can be found in <sup>60</sup>. This OEO provided an oscillation signal at 34.6 GHz with a phase noise of -109 dBc/Hz at 100 kHz offset and a noise floor of -149 dBc/Hz was generated. Moreover, a tunable oscillation frequency in the 1-25 GHz range and a phase noise varying from -100 dBc/Hz to -154 dBc/Hz was also achieved.

As can be seen from all these references and studies, it appears that the replacement of the optical fiber delay line by a high  $Q_{opt}$  optical resonator leads to a new kind of OEO with low phase noise and potentially avoiding the multi-mode operation and mode hopping behavior of classical OEOs. Moreover, shrinking the employed optical resonator size can open the possibility for designing an integrated OEO device with other functions in a same compact footprint. However, even more compact than fiber section OEO, many of the resonator based OEO approaches described here are still

based on discrete elements and have only a moderate to very moderate degree of integration. In this context, there is in fact a strong interest in further miniaturizing the resonator dimension and, if possible, integrating it with the other active and passive functions of the opto-RF loop system. This objective may be entirely feasible in view of the progress made in recent years by the integrated microwave photonics (IWMP) field.

### **1.3.3. Integrated microwave photonics**

Microwave Photonics (MWP) is a growing research and application field in which radio-frequency (RF) signals are generated, distributed, processed and analyzed using the strength of the photonics technology <sup>10,64</sup>. It started in the late 1980s when the transport of microwave signals in the electrical domain faced increasing difficulties due to bulky devices, heating effects, high losses at higher frequencies, low bandwidth and too reduced tunability of high-frequency filters <sup>65</sup>. MWP takes the advance of the photonics technology to provides functionalities in microwave systems and brings advances including reduced sizes, weights, and costs, as well as low and constant attenuation over the entire microwave and mm-W modulation frequency ranges, immunity to electromagnetic interferences, low dispersion and high data-transfer capacity <sup>66</sup>. MWP also adds fundamental value by enabling key functionalities to be realized in microwave systems using photonics, i.e. filtering, arbitrary waveform generation, frequency up/down-conversion, and instantaneous measurement, all of which are quite complex or, in some cases, not even possible using RF techniques alone <sup>67</sup>. It is now found in many applications including cellular, wireless, and satellite communications, cable television, distributed antenna systems, optical signal processing, and medical imaging.

In early works, MWP systems were formed by discrete components such as lasers, modulators, filters, and photodetectors. They were connected together through fiber big tails, occupying large size interconnections. Moreover, the use of discrete components also led to an increase in system costs (mainly packaging costs) and high-power consumption. These factors prevented the widespread application of MWP. An evolution appeared with the availability of photonic integrated circuits (PIC), in which

### 1.3. OEO based on optical resonator

MWP components are incorporated in photonic circuits, and this solution is known as **integrated microwave photonic (IMWP)**. Conceptually, PICs are very similar to electronic integrated circuits. They combine multiple optical components on a single chip to form a single multifunctional photonic device. The use of a fewer photonic chips inherently simplifies the whole assembly process, compared to discrete components, and enables radical miniaturization, cost reduction, and performance enhancement <sup>68</sup>. Thus, IMWP has the potential to scale down the MWP in term of performance, power, footprint and cost efficiency. Moreover, most of the photonic devices are currently highly temperature dependent and so require temperature regulation, which consumes a large amount of the bias power. As integrated photonics systems require less power for temperature control, the power consumed by photonic devices can be reduced drastically.

An important feature of PIC is that a number of different designs can be combined on the same wafer because they all use the same fabrication process, and such a wafer is usually called a Multi-Project Wafer<sup>69</sup>. Despite that many materials can be amenable to produce PICs, only a few platforms have implemented generic processes and offered access to IMWP runs <sup>10</sup>: this mainly includes Indium Phosphide (InP), Silicon Nitride (Si<sub>3</sub>N<sub>4</sub>) and Silicon on Insulator (SOI) technologies. Each of these technological paths has its own strengths and weaknesses. Notwithstanding, impressive functions have been shown in recent times. Some examples of IMWP using different platforms can be seen in **Fig.1.3.3**.

InP takes advantage of the monolithically integration scheme and is the only material enabling various types of active and passive photonic components, including lasers, modulators, optical amplifiers, tunable devices, and photodetectors. This platform allows creating a compact circuit with a bending radius of the order of 100  $\mu\text{m}$ . However, the limitation of this material substrate comes from the optical waveguide losses which are typically high, in the order of at least 1.5-3 dB/cm <sup>73</sup>.

Si<sub>3</sub>N<sub>4</sub> features in ultra-low propagation losses. Depending on the fabrication process, Si<sub>3</sub>N<sub>4</sub> waveguide losses can reach as low as 0.1-0.2 dB/cm <sup>74</sup>. However, due to low index contrast in Si<sub>3</sub>N<sub>4</sub>, bending waveguide radius in Si<sub>3</sub>N<sub>4</sub> devices are typical large

(50 – 150  $\mu\text{m}$ ) which results in moderate compact footprint circuits, while the material itself cannot bring on-chip active functions.

SOI takes benefit of its compatibility with the microelectronic complementary metal oxide semiconductor (CMOS) technology to make electronic-photonic co-integration a real possibility. On the other hand, due to high index contrast between silicon and its oxide, SOI waveguide modes are well confined, offering tight bending radii (minimum feature size at 1.5  $\mu\text{m}$  in the telecom band <sup>75</sup>), thus allowing ultra-compact circuits. Propagation losses in SOI waveguides can be as low as 0.1dB/cm for single-mode operation at telecom wavelengths <sup>76</sup>, and various classes of optical Si modulators and Ge photodetectors operating at least at 40GBbits.s<sup>-1</sup> have been demonstrated. In addition, the hybrid integration of III/V laser diodes on silicon has been demonstrated by several groups <sup>77</sup>.

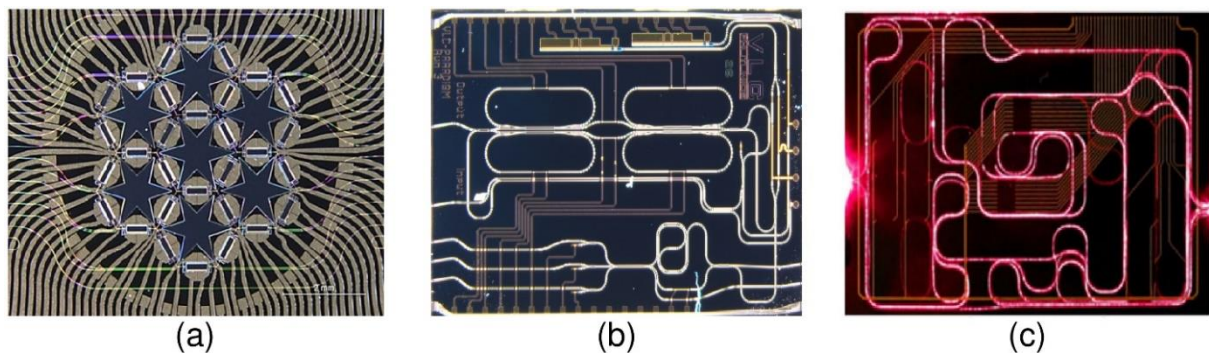


**Fig.1.3.3.** Examples of IMWP in different platform. (a) Programmable signal processor SOI <sup>70</sup>, (b) All-integrated tunable filter in indium phosphide <sup>71</sup> and (c) High spectral resolution bandpass filter silicon nitride <sup>72</sup>.

To sum up, many functionalities have been realized in these technologies, such as beamforming in InP <sup>78</sup> and Si<sub>3</sub>N<sub>4</sub> <sup>79</sup>, a true time delay in SOI <sup>80,81</sup>, MWP filter in InP <sup>82</sup>, Si<sub>3</sub>N<sub>4</sub> <sup>83</sup>, SOI <sup>84,85</sup>, phase shifter in SOI <sup>86</sup>, and all of this provides a strong basis to realize advanced IMWP circuits.

Apart from these mainstream approaches, other materials could also be considered. For example, Chalcogenide glasses which are highly nonlinear materials have been exploited for nonlinear optoacoustic processing based on Brillouin scattering effect to provide small bandwidth MWP filters <sup>87,88</sup>. On the other hand, Lithium Niobate on insulator (LNOI) circuits have allowed to demonstrate ultra-high  $Q$  resonators <sup>89</sup> and

### 1.3. OEO based on optical resonator

compact modulators <sup>90,91</sup>. Finally, polymer materials have also been proposed for implementation delay lines <sup>92</sup> and beamforming functions <sup>93</sup>. Taking into account all functionalities, we can see that the future for the IMWP is bright. Concerning integration, IMWP not only bring the advantage to allow many functionalities in a single chip but also critically enhanced performance, and then opening up many applications such as filtering, microwave signal generation, mobile and wireless networks, analog-to-digital conversion (ADC), frequency measurement or spectrum analysis <sup>10</sup>.

### 1.3.4. Integrated optoelectronic oscillator

As mentioned above, photonic integration has made it possible to make a considerable leap forward in the field of microwave photonics. This has, of course, resulted in significant progress on OEOs. **Table 1.3.2** summarizes some key results reported in recent years.

**Table 1.3.1.** IOEO based on different approaches. WGM: Whispering gallery mode, ODL: optical delay line, SBS: stimulated Brillouin scattering, PM to IM: phase to intensity modulation, MDR: micro-disk resonator.

Architecture	Working frequency	Level of integration	Phase noise
LiNbO <sub>3</sub> WGM <sup>39</sup>	35 GHz	Discretely packaged photonic and RF parts (fully integrated included source)	-108 dBc/Hz @ 10kHz
InP ODL <sup>94</sup>	7.3 and 8.87 GHz	Monolithically integrated photonic and RF parts	~ -90dBc/Hz @ 1MHz
Chalcogenide SBS <sup>95</sup>	5-40 GHz	Partially integrated photonic parts	-100 dBc/Hz @ 10 kHz
PM to IM based on MDR <sup>96</sup>	3 - 8 GHz	PM and MDR in the same chip	-80 dBc/Hz @ 10 kHz
PM to IM based on all-pass ring <sup>97</sup>	10-18 GHz	PM and all-pass ring in the same chip	unknown

Among the first integrated OEOs, a high  $Q$  lithium niobate ( $\text{LiNbO}_3$ ) WGM resonator OEO was reported in Refs <sup>39,98</sup>. All of the three optical parts of the OEO proposed in this work (laser, modulator, WGM filter, and detector) were discretely packaged together with the RF devices. The resonator, excited with light from a semiconductor laser, served both as the high- $Q$  element and as the modulator in the OEO loop. This system achieved an oscillation frequency at 35 GHz and a phase noise level of -108 dBc/Hz at 10 kHz offset from the carrier. To our knowledge, this is up to now the only OEO with a successful integration of the source, and all the optical and electrical RF components. It is now provided by OEwaves (**Fig.1.3.4a**) <sup>39</sup> and has already found application in military platforms <sup>98</sup>.

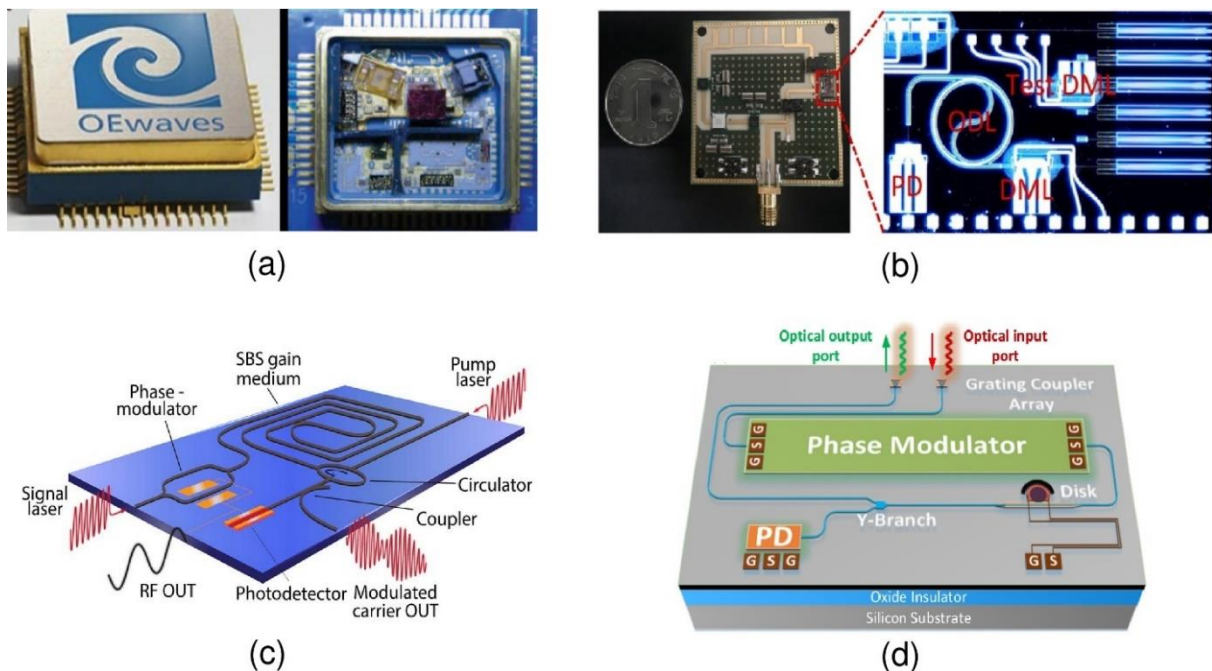


**Fig.1.3.4.** Different integrated OEO based on different substrates and approaches: (a) Lithium niobate ( $\text{LiNbO}_3$ ) WGM resonator <sup>39,98</sup>, (b) InP optical delay line <sup>94</sup>, (c) Chalcogenide stimulated Brillouin scattering <sup>95</sup>, (d) Phase modulator and micro-disk resonator (MDR) on SOI <sup>96</sup>.

In another way, Jiantang *et al.* (**Fig.1.3.4b**) <sup>94</sup> have successfully demonstrated a monolithically integrated photonic and RF parts on a InP substrate. In this proposed scheme, light waves from the directly modulated laser (DML) was detected by a photodetector (PD) after propagation through an optical delay line (ODL). The DML, ODL, and PD were monolithically integrated on the InP photonic platform. The RF

### 1.3. OEO based on optical resonator

components, i.e. the RF filter, the electrical amplifier, attenuator, coupler, bias tee were soldered to the board with a reflow oven and tin-lead based solder paste. Two different oscillation frequencies at 7.3 and 8.87 GHz were demonstrated by tuning the injection current of the laser. Phase noise values of -91 dBc/Hz and -92 dBc/Hz at 1 MHz offset from carrier were obtained for 7.3 GHz and 8.87 GHz, respectively.

The two types of integrated OEO described above have gained a huge reduction in size and weight in comparison with the typical OEO based on a fiber delay line, but the frequency tunability was still limited in these works. In this purpose, one of the preferred approaches is based in the use of phase modulators. One example of this approach is the OEO based on stimulated Brillouin scattering (SBS) (**Fig.I.3.4c**)<sup>95</sup> made of a 6 cm long highly nonlinear chalcogenide rib waveguide with a cross section of 850 nm×2.6 μm. By using two distributed feedback (DFB) lasers, one passing through a phase modulator and coupled into SBS, the second serving as a pump laser and coupled from the opposite side of the chip to generate the narrow-band SBS response, one sideband of a phase-modulated signal was amplified by the SBS gain, and a phase modulation to intensity modulation conversion was performed. A microwave signal was then generated by the PD. The entire operation of the system was in fact equivalent to a microwave photonic filter, with the passband determined by the SBS gain spectrum. The bandwidth of the MPF was around 34 MHz<sup>99</sup> due to a narrowband signal provided by the SBS mechanism. The obtained oscillation frequency at 40 GHz was characterized by a phase noise lower than -100 dBc/Hz at 10 kHz offset frequency. Moreover, by tuning the frequency of the carrier laser relative to the pump laser, an ultrawide tunability (5-40 GHz) of the generated microwave signal without any degradation of performance was demonstrated.

Similarly, a combination of phase modulation and optical notch filtering was employed in a SOI photonic circuit<sup>96,97</sup>. In this configuration, either a microdisk resonator (MDR)<sup>96</sup> or an all-pass ring resonator<sup>97</sup> was used as an optical notch filter to filter out one sideband of a phase modulated signal, thus achieving phase modulation to intensity modulation conversion. As it was observed, the entire operation was equivalent to an MPF, with a bandwidth determined by the bandwidth of the notch of the optical notch filter. The center frequency was determined by the wavelength spacing between

the optical carrier and the center wavelength of the notch. By feeding back signal to the modulator with a sufficient gain, an oscillation frequency was generated. In <sup>96</sup>, two configurations of MDR with a high resistivity metallic microheater placed on top or a p-type doped silicon heater in the MDR were investigated. By controlling the electrical power applied to the micro-heater, the resonance frequency of the resonator was tuned, leading to the tuning of the center frequency of the bandpass MPF, and thus of the frequency of the generated microwave signal. Experimentally, an oscillation frequency with a tunable range from 3 to 8 GHz with a phase noise performance around -80 dBc/Hz at 10 kHz offset frequency was demonstrated. This scheme of OEO was explored for sensing applications. As reported in <sup>97</sup>, by tuning the temperature of the all-pass ring, the resonance frequency of the resonator was changed, which resulted in a change of the oscillation frequency. By calculating the change of oscillation frequency with respect to the device temperature change, a sensitivity of 7.7 GHz/°C was demonstrated, showing the ability of the oscillator to be extremely sensitive to small temperature variations.

To sum-up, integrated OEO show key advantages for RF signal generation in terms of small size, high stability, low power consumption, and large frequency tuning range. From the successful demonstration listed above, a future for IOEO in a single chip is expected to be bright with the potential to open up a new range of applications for RF signal generation. Nevertheless, in this domain, more studies are necessary before to arrive at a complete system and different approaches remain possible.

## 1.4. Conclusion

In this part, we have presented some elements concerning the evolution of microwave signal generation, starting from microwave oscillators to OEO based on optical fiber delay lines, and then to OEO based on optical resonators. As it is, each generation was born in order to reduce the disadvantages of the previous ones. Clearly, the latest generations of OEO based on optical resonators offer many advantages, i.e. low phase noise signal at microwave and millimeter wave signal, small size, low power

### *1.3. OEO based on optical resonator*

consumption, giving an opportunity to reduce or avoid mode hopping, and eliminating the requirement of bulky temperature control system.

**Regarding their integration**, very significant progress has been made in recent times. However, not all the challenges have been fully achieved; in particular, the **integration on silicon** of all the elements of a complete OEO system, largely tunable in frequency, has still not been achieved. **The target of this work is to go this way, by considering firstly the direct insertion of SOI micro-resonators in OEO loops.** Two different approaches with

fixed and tunable frequency schemes will be discussed and explored in this thesis. Generating RF/Optical signals has, of course, applications in the field of telecommunications or radars. On another hand, as described in section **I.2.4b**, OEO is turning out to be also a very useful system for sensing applications. Looking towards this kind of applications, this work will be focused on this option and the capabilities of the studied OEO with respect to index sensing will be systematically investigated throughout the manuscript.

**Chapter 2** will first, deal with the reason why we have chosen the silicon photonic platform for the integration of OEO. Some necessary photonic building already developed on SOI will be discussed accordingly. The last three parts of chapter 2 will then been focused on the design, the fabrication, and the characterization of optical ring resonators in view of their insertion into OEO opto-RF loops.



# 2

## Silicon Ring Resonator Design, Fabrication and Characterization for OEO Loops

Among several material platforms which can offer access to integrated microwave photonics and particularly to the possible realization of integrated Optoelectronic Oscillators (OEOs), we have chosen to work with the Silicon on Insulator (SOI) one. In the following of this manuscript, we will explain the reason for this choice. Three main building blocks necessary for integrated OEOs and well developed in Si photonics will be discussed in this chapter. Then, we will introduce the ability of using OEO for sensing detection, as it is one of the main aims of this work.

### 2.1. Integration within silicon photonics

Silicon photonics emerged in the mid-1980s but has really been developed from the early 2000s and has established itself as the major photonic integration platform for various applications such present and future applications in data centers, high-performance computing, and sensing <sup>76</sup>. Among diverse technological platforms used to realize photonics integrated circuits (PICs), SOI photonics is now seen as the mainstream one due to some specific advantages. First of all, the ability to use the Complementary Metal Oxide Semiconductor (CMOS) technology has become the key advance behind silicon photonics, resulting in high volume production capability at low cost <sup>76,100</sup>. Moreover, Silicon – Si ( $n_{Si} = 3.48$  at  $\lambda = 1.55\mu\text{m}$ ) and its oxide - SiO<sub>2</sub> ( $n_{SiO_2} = 1.44$  at  $\lambda = 1.55\mu\text{m}$ ) can form high-index contrast ( $\Delta n \sim 2$ ), and thus high-

confinement optical waveguides ideally suited for medium to high integration and small passive devices in the telecommunication wavelength range ( $1300 \text{ nm} \leq \lambda \leq 1600 \text{ nm}$ ). The field has rapidly evolved from a ‘scientific hot topic’ to an industrially viable platform and starts bringing market benefits. The fast development of Si photonic integration circuits has been allowed by the possible realization of multiple functions in a single chip. Regarding integrated OEOs, the three main necessary components of the opto-RF loop, i.e. the light source, the optical modulator, and the signal detector have been developed in/on SOI platform, at least considering the possible hybrid integration of III/V devices on Si.

In the next section, we will introduce the three basic key devices essential for PICs and particular for integrated OEOs. Then, we will draw a specific focus on recent progress on index sensing in Si photonics in order to introduce the basics that we will use later to characterize the index sensing properties of the OEOs demonstrated in chapter 3 and chapter 4.

## **2.1.1. Basic functions in silicon photonics**

### **2.1.1a. Lasing in Silicon photonics**

Light source is an indispensable component in every telecommunication system, including integrated OEOs. However, laser is a weak point in silicon photonics. It is because Si is an indirect bandgap material, and it not naturally capable of providing efficient radiative recombination <sup>11</sup>. Three main approaches have been proposed to achieve light generation in/on silicon: The hybrid integration of luminescent materials on silicon, Germanium (Ge)-on-Si lasers, and III-V-based Si lasers <sup>101</sup>. Each approach has unique properties and advantages, but also drawbacks.

The hybrid integration of luminescent materials on silicon takes advantage of materials that naturally exhibit light emission and that can be integrated on silicon. Examples of such materials are carbon-nanotubes <sup>102</sup> or rare-earth materials in which Erbium is the most popular employed one <sup>103–105</sup>. Taking into the fact that Erbium is a well-studied material and it can be considered a (nearly) CMOS compatible material,

## 2.1. Integration within silicon photonics

a lot of research efforts have been pursued in the direction of Er-laser. However, up to now, no efficient electrically pumped laser based on Erbium has been reported yet. Nevertheless, optical pumped laser based on Erbium doped gain media<sup>104,106,107</sup> has been demonstrated, showing promises for Er-silicon-based lasers.

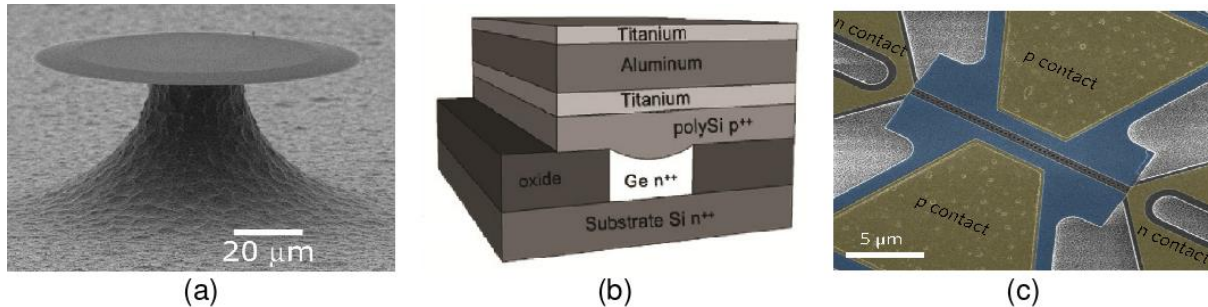


**Fig.2.1.1.** Examples of silicon-based laser: (a) Microsphere Er doped laser<sup>106</sup>, (b) First electrical pump silicon laser based on Ge<sup>108</sup> and (c) III-V based silicon laser using hybrid InP<sup>109</sup>.

In another direction, although Ge is an indirect band gap material, it exhibits a pseudo-direct gap behavior<sup>110</sup>. This unique band structure allows for Ge to operate properly at telecommunication wavelengths around 1.55 μm and potentially to achieve efficient light emission by engineering its band structure. Bandgap engineering concepts of Ge, either using n-type doping<sup>111</sup>, tensile strain layers<sup>112</sup>, or germanium-tin (GeSn) alloys<sup>113</sup> have been proposed. In addition, the first electrically pumped Ge laser was successfully demonstrated in 2012<sup>108</sup>, with a lasing wavelength in range from 1520 nm to 1570 nm (**Fig 2.1.1b**). Moreover, Ge-based lasers potentially show advantages of processing compatibility with the Si technology, allowing to reduce device fabrication under the single flag of group IV materials.

Finally, III–V based lasers are in fact considered as the present most practical on-chip optical sources in silicon photonics. III-V semiconductor materials bring the advantage of direct bandgap emission, high gain values and band gap tuning by the control of alloy compositions<sup>76</sup>. Three common approaches were demonstrated: direct mounting integration<sup>114</sup>, heterogeneous based on bonding<sup>109,115,116</sup>, and direct hetero-epitaxial growth<sup>117–119</sup>. High quality hybrid on Si III-V lasers have been reported either in heterogeneous based bonding<sup>109</sup> or epitaxial growth<sup>120</sup>. More recently, III-V on

silicon laser using transfer printing method was proposed <sup>121</sup>, demonstrating high output power above 2 mW and low threshold current of around 18 mA.

To summarize, we have shortly discussed here the possible ways of light generation in/on silicon. Currently, III-V-based Si lasers formed via bonding techniques demonstrate the best performances and show the best opportunities for practical applications in the near future. However, in the long term, direct hetero-epitaxial growth of III-V materials on Si seems more promising for low-cost and high-yield fabrication <sup>101</sup>. On the other hand, Ge-based Si laser with its advantages on CMOS compatible can be considered as a competitive candidate for large scale monolithic integration for the long-term approach.

### 2.1.1b. Silicon optical modulators

Electrical to optical signal (E/O) conversion through the modulation process is a necessary function for OEOs. The field of silicon optical modulators has attracted strong research attention since the two precursory works demonstrated by Intel Corporation in 2004 <sup>122</sup> and Xu et al. <sup>123</sup> in 2005. However, silicon is not an ideal material in which to produce an optical modulator since it lacks the linear Pockels electro-optic effect found in more traditional photonics materials. Several approaches have been proposed to achieve high performance modulation in silicon devices. The most common method is based on using the plasma dispersion effect, where free electron and hole concentrations in an optical waveguide result in changes in the material's refractive index and absorption <sup>12,124,125</sup>. The other method is to introduce a strong electro-optical effect material to the silicon platform, examples of them are graphene <sup>126,127</sup>, organic polymers <sup>128,129</sup> or III-V compounds <sup>130</sup>. A further approach to achieve modulation in silicon involves straining the silicon waveguide to introduce the Pockels effect <sup>131</sup>.

Silicon-based modulators can implement different types of modulation formats, including intensity <sup>122,133</sup>, phase <sup>125,127</sup> and polarization <sup>126</sup> modulations. All of them are suitable for OEOs since OEO based on intensity <sup>134</sup>, phase <sup>97</sup> or polarization <sup>135</sup> modulators have been experimentally studied. With efforts from both academic institutes and industry, the performance of modulators based on silicon have been improved dramatically. A silicon-based modulator with a flat frequency response

## 2.1. Integration within silicon photonics

exceeding 170 GHz<sup>125</sup> (**Fig.2.1.2a**) has been investigated by using the plasma dispersion effect. Up to now, the modulation speed of on-off keying (OOK) signal reached up to 70 Gbit/s<sup>136</sup> and a bit rate of 321.4 Gbit/s modulator was demonstrated<sup>137</sup>.

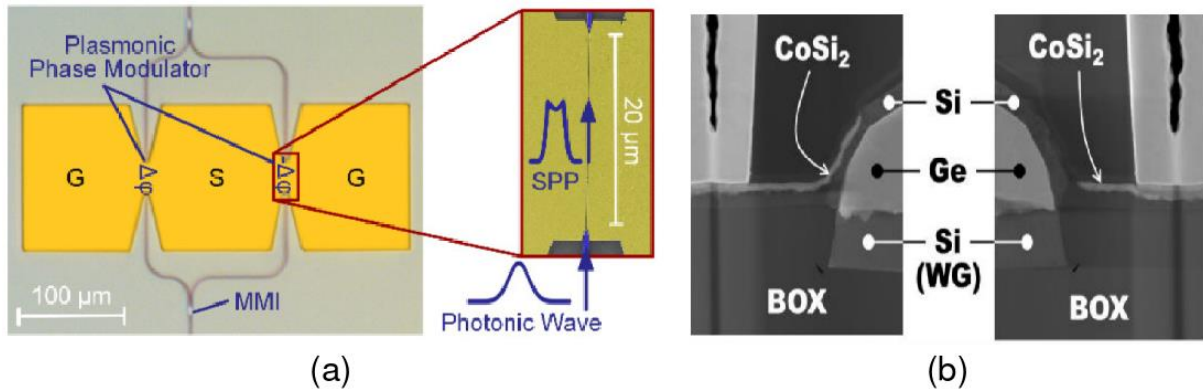


**Fig.2.1.2.** Examples of: (a) Silicon-based modulator using plasmonic dispersion effect<sup>125</sup> and (b) Silicon-based photodetector using Ge<sup>132</sup>.

### 2.1.1c. Photodetector based on silicon photonics

Optical to electrical (O/E) signal conversion using a photodetector is an essential process used for the realization of OEOs. However, due to its bandgap energy, silicon is obviously not a suitable candidate for photodetection at telecom wavelengths. Photodetector fabrication therefore requires the integration of either III/V materials<sup>138,139</sup> or Ge<sup>13</sup>. Hybrid III/V materials on Si can be used but require heterogeneous integration on Si. In contrast, Ge has strong absorption up to beyond 1.55 μm wavelength and this material is already present in current CMOS processes. Ge therefore arises as the best candidate for implementing detection in Silicon photonics. After years of exploration and optimization, the basic brick "germanium detectors" is now very well mastered. State-of-the-art Ge waveguide photodetectors can achieve high responsivity (around 1 A/W), high bandwidth (around 70 GHz), and low dark current simultaneously<sup>132,140</sup> (**Fig.2.1.2c**). In summary, these detectors have the characteristics necessary for their effective integration into a fully integrated opto-microwave loop on silicon.

Beside the three main basic key functions shortly reminded above, Si photonics offers many other devices such as optical amplifiers<sup>141,142</sup>, optical isolators and rotators<sup>143,144</sup>, optical filters<sup>145,146</sup>, (de)multiplexers<sup>147,148</sup>, splitters<sup>149</sup>, etc. The contribution of

these devices brings a bright future for PICs and particularly integrated OEOs. The field of application of silicon photonics therefore are very numerous, including data centers, high performance computers, telecommunications, microwave photonics, quantum computers, sensors and other high-end applications.

We will focus here only on the sensing properties of the silicon platform, taking into account the topics explored in this thesis and the orientation that has been chosen to realize and study optoelectronic oscillators in an index sensor configuration.

Our analysis here will be limited to volume refractive index sensors, the objective being essentially, through optical measurements, to detect the smallest possible variation in refractive index.

## 2.1.2. Silicon photonics for bulk index sensing applications

The detection of biological species in a fast and reliable way is still today an important challenge. In term of biosensing, different principles have been explored, i.e. optical, electrical, magnetic and mechanical ones to quote the main ones. Compared to other analytical techniques, optical biosensors offer several advantages, i.e. absence of risks of electrical shocks or explosion, immunity to electromagnetic interferences, miniaturization capabilities, and possibility of data multiplexing <sup>150</sup>. In general, optical biosensors can operate according to two protocols: fluorescence- based detection and label-free detection <sup>150,151</sup>. In fluorescence-based detection schemes, fluorescence is used as a label to indicate the presence of the target molecule, resulting in an extremely sensitive detection. However, this technique suffers from the laborious labeling processes that may also interfere with the functionalized molecules. Quantitative analysis is challenging due to the fluorescence signal bias, as the number of fluorescence on each molecule cannot be precisely controlled <sup>152</sup>. In contrast, label-free biosensors do not require to label target molecules. Their features are relatively easy and cheap operation allowing to perform quantitative and kinetic measurements of molecular interactions <sup>150,152</sup>. Under the category of label-free detection, several detection methods exist, including refractive index (RI) detection, optical absorption detection and Raman spectroscopic detections.

## 2.1. Integration within silicon photonics

Here, we will limit our discussion in RI based label-free sensor detection. In the principle of RI based label-free sensor detection (**Fig.2.1.3**), the biomolecular interaction taking place at the waveguide surface affects the guiding properties of the waveguide, i.e. a variation of the refractive index, via the modification through the evanescent field. The variation of the refractive index can be evaluated by any of the waveguiding optical properties (intensity, phase, resonant momentum, polarization...). The evaluation of this optical change gives a measure of the quantity of detected molecules.

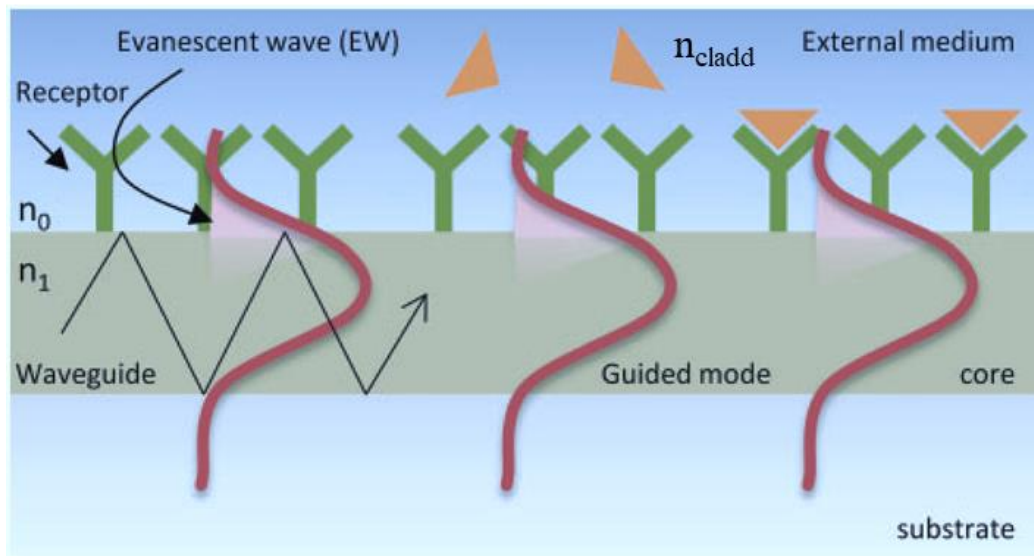


**Fig 2.1.3.** Scheme of the evanescent field sensing <sup>153</sup>.

Today, RI label-free biosensors can be fabricated based on several material substrates, but one of the most popular and promising materials is silicon. Silicon photonics with CMOS-compatibility offers significant large scale capability, allowing for the integration of thousands of sensors on a single millimeter-scale chip <sup>154</sup>, thus devices can be cheaply built through mass production with industrial silicon technologies and they could become the core of portable laboratories. Several silicon photonics devices such as Mach–Zehnder interferometers (MZIs) <sup>155–158</sup>, micro-ring resonators (MRRs) <sup>159–162</sup>, Bragg grating resonators <sup>163–165</sup>, and one-dimensional (1D) or two-dimensional (2D) photonic crystals (PhCs) <sup>166–169</sup> have been developed over the past years for biosensing diagnostic applications. Among them, **SOI ring resonators are the most common configuration used for RI sensing** <sup>170</sup>. The advantage of using ring

resonators compared with other types of RI configurations is the possibility of miniaturization and simplicity.

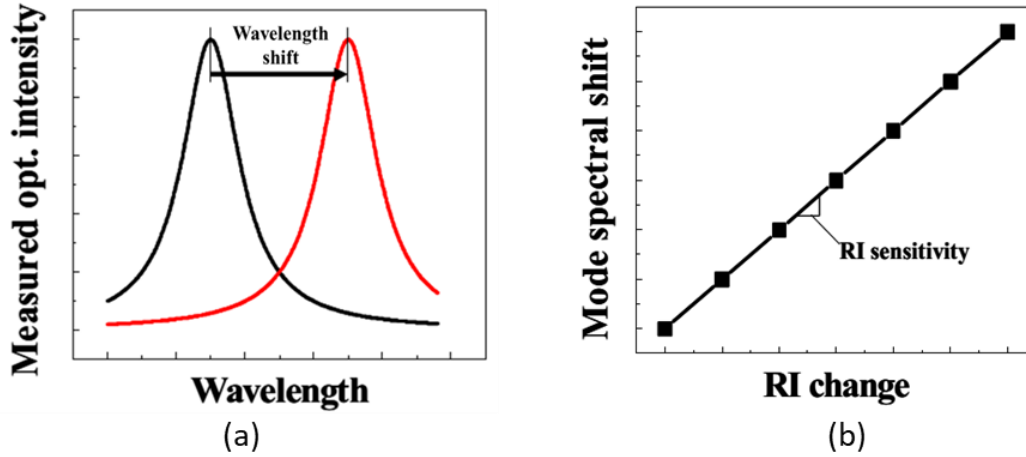


**Fig 2.1.4.** (a) Typical method used in bulk optical refractive index sensors by measuring the wavelength change dependent on the cover refractive index of the sample, (b) The RI sensitivity is determined by the slope of the wavelength shift for known changes in the sample cover material RI.

In addition to the sensing operation, microfluidic channels are often added to the experimental system, for the realization of lab-on-chips. The most common materials used for the fabrication of the micro-fluidic channels is PDMS (*Polydimethylsiloxane*) [151,163,170,171](#). It is a biocompatible, transparent, rubber-like polymer and can be easily patterned using soft lithography, a well-established fabrication method. The incorporation between silicon substrate and PDMS is formed through the oxygen plasma process, in order to create hydrophobic surface properties in both surface of two materials. By doing so, the covalent siloxane bonds (Si-O-Si) is assembled in contact between them.

For typical bulk optical refractive index sensors, changes in the cladding's refractive index (resulting from molecular binding events or concentration changes) change the effective index of the propagating mode. The ratio of the change in effective index of the propagating mode to the changes in refractive index of the cladding medium, is defined as the mode sensitivity,  $S_{mode}$  [172,173](#):

$$S_{mode} = \frac{\delta n_{eff}(n_{clad}, n_{co}, n_{box}, \omega)}{\delta n_{clad}} \quad (2.1.1)$$

## 2.1. Integration within silicon photonics

where  $n_{eff}$  is the effective index of the waveguide,  $n_{clad}$  is the refractive index of cladding medium,  $n_{co}$  is the refractive index of the waveguide core material,  $n_{box}$  is the refractive index of the buried oxide (BOX) material and  $\omega=2\pi f$  is the optical frequency. In case of a resonator device, this change in the effective index, in turn, results in a change in the resonance wavelength  $\lambda_{res}$  of the resonator, which can be measured (**Fig 2.1.4a**). The sensor's refractive index sensitivity is defined as the shift in resonant wavelength as a function of the change in refractive index (RIU) of the cladding [151,152,172,174](#).

$$S = \frac{\Delta\lambda_{res}}{\Delta n_{clad}} \text{ (nm/RIU)} \quad (2.1.2)$$

The sensor's refractive index sensitivity is an important factor used to quantify its performances. However, it does not wholly show the capability of the device to detect and quantify refractive the index changes. To look for the ability to precisely and accurately measure RI changes, the limit of detection (*LOD*) should be also accounted for. Besides, this is the most common parameter used to draw comparisons between different types of bulk index sensors [151,172,173](#).

*LOD* is defined as the smallest spectral shift that the sensor can accurately measure [173](#).

$$LOD = \frac{R}{S} \quad (2.1.3)$$

where  $R$  is the sensor resolution depending on the spectral resolution and the system noise factor of the methodology for measuring the spectral shift in response to a sample.

If infinitely high spectral resolution and zero noise systems were available, the sensor performance could be characterized by the sensitivity alone. However, in real measurements, spectral resolution and system noise are affected by the precision and accuracy of the measurement system including its intrinsic spectral resolution and all possible noise sources (laser RIN, thermal noise, digital noise in case of data processing after signal digitalization, etc.) [173–176](#). Clearly, the way to improve the *LOD* of the sensor is thus to increase the full chain acquisition system spectral resolution and reduce all the noise sources of the system (including the transducer and the acquisition system).

However, this option is somewhat difficult in practice. Indeed, a  $\Delta n$  index resolution results in a wavelength variation in the order of  $\Delta\lambda = \lambda \times \Delta n / n$  in most interferometric optical systems. As a result, for an index detection limit of ( $\Delta n = 10^{-7}$ ), the spectral offset to be detected is already as small as  $\Delta\lambda = 0.1 \text{ pm}$  at  $\lambda = 1500 \text{ nm}$  and can even become smaller for lower target *LOD*. These extremely low orders of magnitude make it difficult to detect direct spectral detection for measuring refractive index variation as the noise sources of acquisition systems most often provide cumulative spectral uncertainties greater than these orders of magnitude. Moreover, in conventional optical sensor systems, the sensing information encoded through the wavelength shift measurement is usually done by using an optical spectrum analyzer (OSA) <sup>177</sup>. However, for a given spectrum, when using an OSA, the higher sensing resolution requires for lower interrogation speed and more time to scan the spectrum range.

These limitations can be solved by modifying the measurement which allows to go back to the refractive index information. Especially, **converting the measurement signal from the optical domain to the electrical one by using an RF carrier frequency as the new measurement can offers an elegant solution for encoding the refractive index information on the RF frequency of a microwave signal** <sup>175,176,178,179</sup>. By converting a wavelength variation in the optical domain to a microwave variation in microwave domain, signal can be real-time monitored by a digital signal processor (DSP) at a high speed and high resolution <sup>176</sup>. In addition, the microwave signal generated by an OEO can also have low phase noise, a high  $Q$  factor, and much higher signal-to-noise ratio <sup>180,181</sup>, therefore the sensor resolution can be improved by using an OEO as a sensor detection for bulk index sensing. Example of this approach can be found in ref <sup>175</sup>, where a highly precise on-chip sensing device with sensing precision approaching  $10^{-8}$  in effective refractive index units was demonstrated. In addition, on-chip optical sensing systems allow the simultaneous measurement of several quantities. In <sup>182</sup>, for example, temperature and refractive index changes with interrogation resolutions of  $2.4 \times 10^{-5} \text{ K}$  and  $9.1 \times 10^{-8} \text{ RIU}$  were demonstrated, respectively. **This approach, which involves the design and realization of opto-microwave loops OEO for bulk index sensing, is at the heart of this thesis work, with a specific focus on**

**the integration of part of OEO within the silicon photonic platform, as described hereafter in this manuscript.**

To conclude this part, the development of OEOs for the generation of microwave signals with low phase noise can be applied to the realization of highly sensitive volume optical index sensors, in which **the measurand is the microwave frequency** whose variations reflect changes in the optical index. All the silicon photonics building blocks necessary for this integration scheme (strictly speaking, excepted the integrated sources), including electro-optical modulators, optical waveguides and resonators, and photodetectors, are available. But all the problems raised by such an ambitious integration scheme have been yet solved and several important milestones have still to be demonstrated.

As indicated in **Chapter 1**, the path that was mainly chosen in this thesis consists in the partial integration of the elements of the loop, essentially that of a ring resonator whose function, combined with the other elements, leads to the realization of an equivalent microwave filter. This is why we specifically develop the principle of operation of ring resonators in the next section.

## 2.2. Silicon micro-ring resonators

Basically, every micro-ring resonator is formed under a waveguide structure. Therefore, in the following of this manuscript, before going into details about ring resonators (RR), some basic introduction about SOI waveguides and their configurations will be given first.

### 2.2.1. Waveguide families

The research field of silicon photonics is now pretty mature and considered as a technology platform for large scale integrated photonic circuits <sup>183,184</sup>. Silicon on insulator waveguides include Si ( $n_{Si}= 3.48$  at  $1.55 \mu\text{m}$  wavelength) on top of  $\text{SiO}_2$  ( $n_{\text{SiO}_2}=1.44$  at  $1.55 \mu\text{m}$  wavelength) and are mainly used in the O and C bands ( $1.3 \mu\text{m} - 1.55 \mu\text{m}$ ) <sup>76,100,185-188</sup>, but have also recently shown promises in the mid-infrared spectral region <sup>189</sup>. SOI waveguides typically consist of a silicon core on top of buried

oxide (BOX). 220 nm thin film SOI wafers is a standard silicon thickness used by multi-project wafer foundries. However, other thicknesses such as 300 nm, 500 nm or 700 nm are also in use. Under the CMOS processes compatibility, various kinds of SOI waveguides have been fabricated either by fully etching Si down to the bottom oxide layer or partially etching it with a timed process stop<sup>184</sup>. Examples of frequently used silicon waveguide structures are illustrated in **Fig.2.2.1**.

Propagating modes in SOI waveguides are found by the solving Maxwell's equations. For many applications, the fundamental (single-mode) transverse electric (TE) or transverse magnetic (TM) modes are preferred. The typical mode profile of some waveguide structures is showed in **Fig.2.2.2**. In SOI waveguides, the high index contrast between silicon and its oxide ( $\Delta n \sim 2.0$ ) allows for downscaling of device footprints to the order of submicron waveguides. In many cases, the height of the core is typically half of the width<sup>190</sup>, thus a typical waveguide core geometry is a  $450 \times 220 \text{ nm}^2$  rectangle. Moreover, high index contrast between the silicon core and its substrate offers for tight bends and close spacing

waveguide geometries and therefore results in dense packing of optical elements on the surface of a chip<sup>76,185,186</sup>.

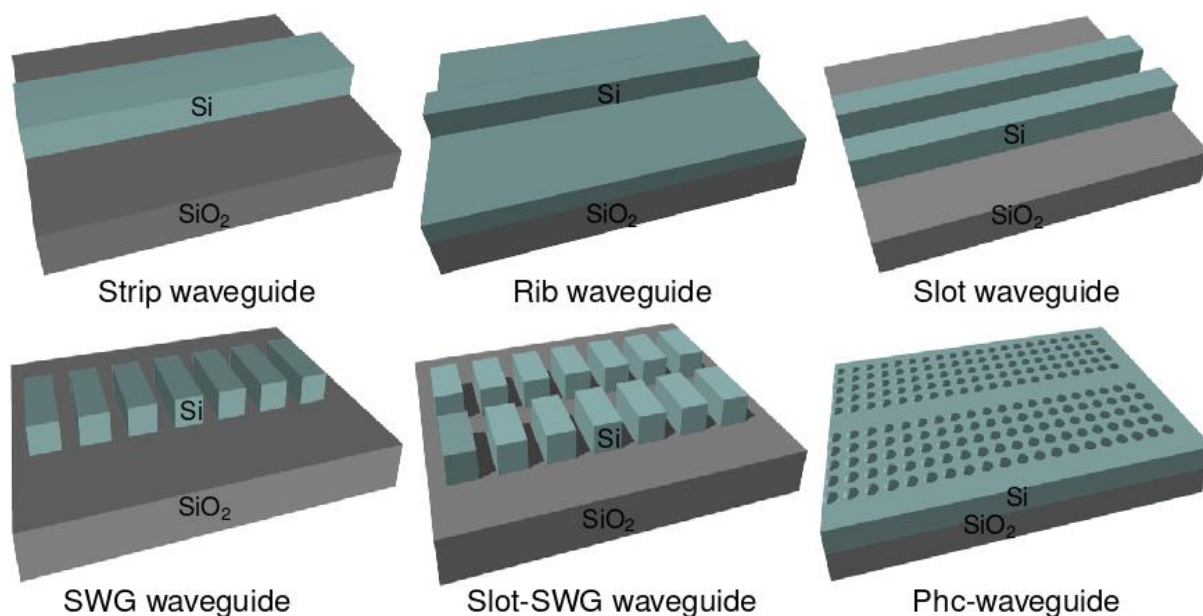


**Fig.2.2.1.** Various types of SOI waveguide structures.

## 2.2. Silicon micro-ring resonators

Silicon strip waveguides, also known as channel waveguides, are the most common building blocks in silicon photonic integrated circuits. In strip waveguides, the modes are well confined in the core region thanks to the high index contrast between silicon and silica. This type of waveguides typically offers tight bending radius, e.g. SOI strip waveguide with bending radius of  $1.5 \mu\text{m}$  has been reported <sup>75</sup>. Rib waveguides, on the contrary, are formed by shallow etched ribs and are often used to reduce waveguide losses due to the reduced interaction of the electric field intensity with the waveguide sidewalls. These waveguides are also widely used for the realization of electrooptic devices such as optical modulators because they allow electrical connections to be made on the waveguide sides <sup>191</sup>.

Slot waveguides have been proposed to confine the electromagnetic field within a subwavelength split and thus serve as a guiding platform for enhancing light/matter interactions. In a slot waveguide, light is confined in the low refractive index region (slot) thanks to the perpendicular electric field discontinuity condition at high index contrast dielectric-dielectric interfaces <sup>192</sup>.

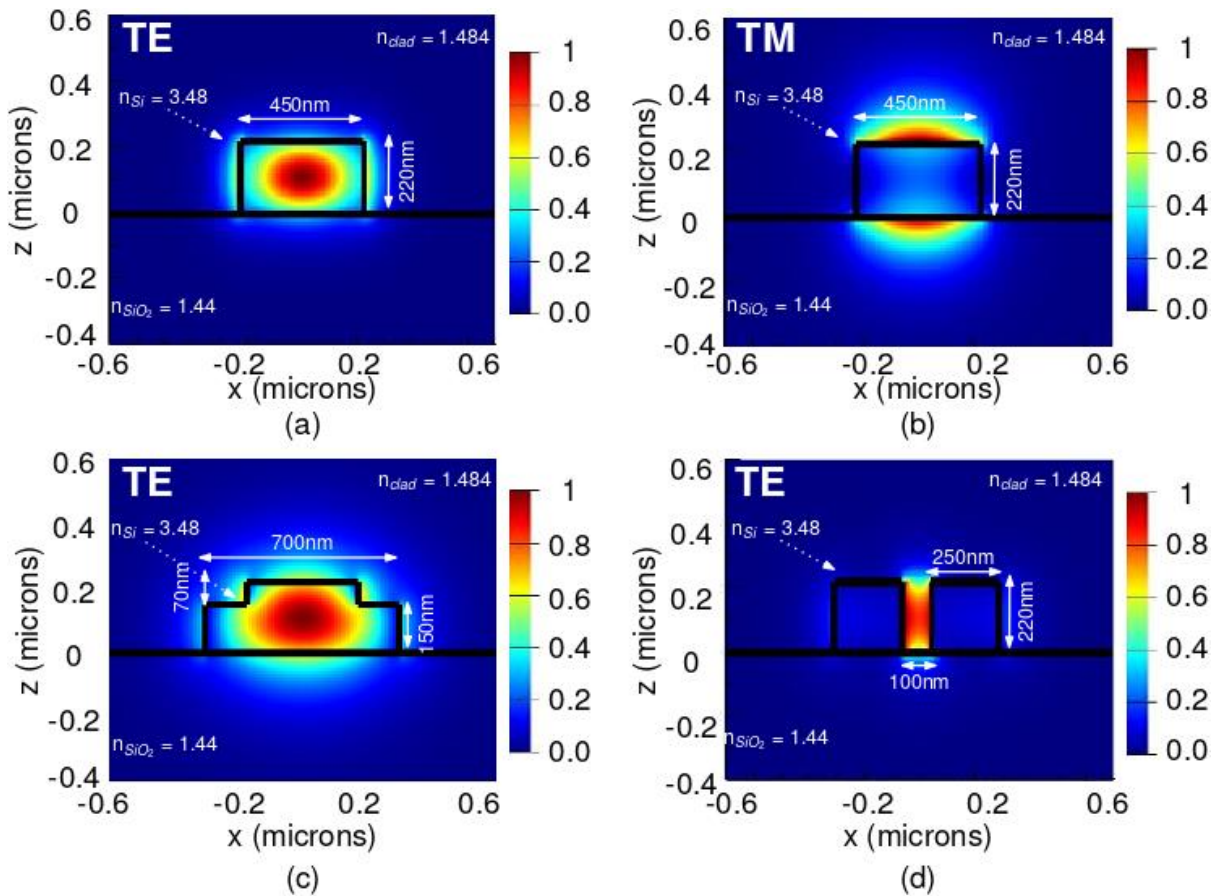


**Fig.2.2.2.** Typical mode profiles of various waveguide structures at 1.55  $\mu\text{m}$  wavelength: (a) and (b) TE and TM modes strip waveguide, respectively, (c) TE mode rib waveguide and (d) TE mode slot waveguide.

These different families of waveguides have advantages and disadvantages, the balance being essentially a compromise between optical confinement of the guided mode and propagation losses. **With regard to the application we are aiming for, namely the realization of bulk optical index sensors, the essential point is to favor a strong interaction of the propagative mode with the cladding material and simultaneously to minimize propagation losses.** In a strip waveguide configuration, target molecules of interest interact with the relatively weak evanescent electric field (TM mode) of the waveguide core <sup>150,158,193</sup>. To increase light-molecule interaction, silicon slot waveguide can be used. In this type of waveguides, a large fraction of the mode resides in the low index cladding where the molecules are located <sup>150,161,194</sup>. However, high sensitivity to sidewall roughness induce higher scattering losses in these structures than in strip waveguides. State of the art is indeed of  $\sim 2$  dB/cm for silicon single mode slot waveguides <sup>195</sup>, while propagation losses as low as  $0.45 \pm 0.12$  dB/cm at 1.55  $\mu\text{m}$  wavelength have been demonstrated for single-mode SOI strip waveguides <sup>195</sup>. The waveguide structure used for sensing application therefore must be chosen in order to take into account the waveguide losses.

By choosing a strong interaction between field and cladding materials and the simplicity of the realization of the waveguides and resonators, **we have opted early in the thesis for TM-polarized strip waveguides.** The relevance of this choice was confirmed recently by an article published in the OSA/Optica journal <sup>196</sup>, which demonstrated, following an exhaustive comparison of SOI waveguide families, that TM polarized strip waveguides correspond to the best possible realization for an application to the detection of refractive index variations in volume.

The ring resonators designed and realized in this thesis have therefore been based on this geometry of optical waveguides and this light polarization.

### 2.2.2. Silicon ring resonators

Ring resonators (RR) are now a basic device in silicon photonics. A RR is a passive device but can become an active one if the integration with an active material or thermal contact is performed <sup>187</sup>. RRs have wide range of applications in many fields such as optical modulators, optical filters, optical sensors, electro-optic devices <sup>76,145,172,197</sup>. In the basis configuration, RR can be described into two main structures, namely all-pass and add-drop RR, as illustrated in **Fig.2.2.3a** and **Fig.2.2.3b**, respectively.

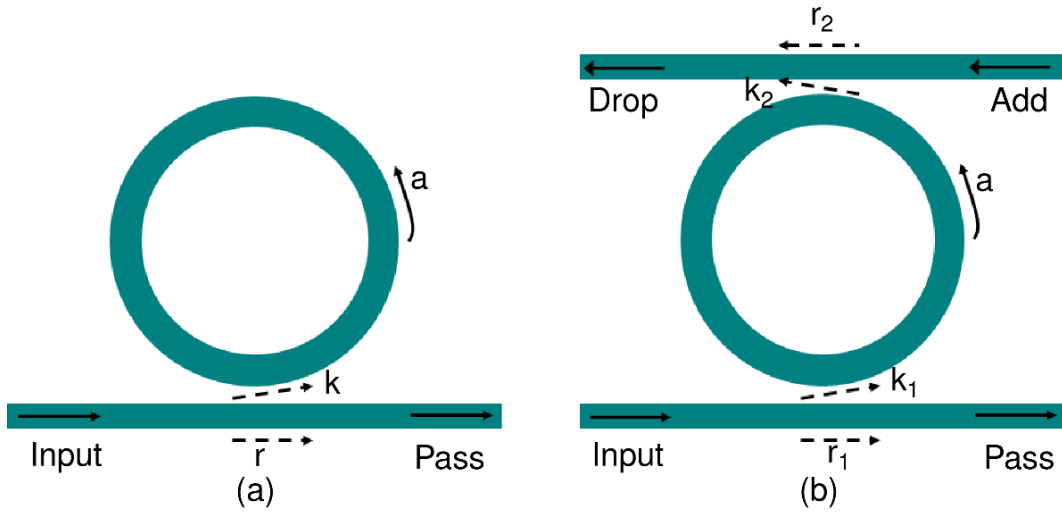


**Fig.2.2.3.** Ring resonator configuration: (a) All-pass and (b) Add-drop RR.

In general, a RR is formed by a circle bended waveguide and a bus waveguide coupled with the ring. When the light path inside the ring corresponds to a round trip phase shift of  $2\pi$ , waves interfere constructively, and the ring is then at resonance. Resonance mode wavelengths are thus given by:

$$\lambda_{res} = \frac{n_{eff} * L_{tot}}{m} \quad m = 1,2,3 \dots \quad (2.2.1)$$

with  $L_{tot}$  is the optical path length of the resonator and  $n_{eff}$  is the waveguide mode effective index.

#### 2.2.2a. Power transmission of an all-pass ring resonators

An all pass RR configuration, as described in **Fig.2.2.3a**, is a simplest configuration of RR, which includes a single side-coupled bus waveguide. Under the

assumption that reflections are negligible, from the ratio of the transmitted and the incident field, we obtain the intensity transmission pass through the ring  $T_n$  <sup>187,198</sup> as:

$$T_n = \frac{I_{pass}}{I_{input}} = \frac{a^2 - 2racos\theta + r^2}{1 - 2arcos\theta + (ra)^2} \quad (2.2.2)$$

with  $a$  the single-pass amplitude transmission, including both propagation losses in the ring and losses in the waveguide/ring directional coupler. It relates to the power

attenuation coefficient  $\alpha$  (dB/cm) as  $a^2 = \exp(-\alpha L_{tot})$ .  $\theta$  is single pass phase shift,  $\theta = \beta L_{tot}$  with  $\beta$  is the propagation constant of the circulating mode,  $\beta = (2\pi n_{eff})/\lambda$ ,  $r$  is the self-coupling coefficient, and  $k$  is the cross-coupling coefficient. Assuming non-coupling losses,  $r$  and  $k$  then satisfy  $r^2 + k^2 = 1$ .

### 2.2.2b. Power transmission of an add-drop ring resonator

An add-drop RR configuration described in **Fig.2.2.3b** consists of two bus waveguides coupled to the ring. The intensity transmission at the through and drop ports of the ring are given by <sup>187,198</sup>:

$$T_{through} = \frac{I_{pass}}{I_{input}} = \frac{r_2 a^2 - 2r_1 r_2 a \cos\theta + r_1^2}{1 - 2r_1 r_2 a \cos\theta + (r_1 r_2 a)^2} \quad (2.2.3a)$$

$$T_{drop} = \frac{I_{drop}}{I_{input}} = \frac{(1 - r_1^2)(1 - r_2^2)}{1 - 2r_1 r_2 a \cos\theta + (r_1 r_2 a)^2} \quad (2.2.3b)$$

If the attenuation is negligible ( $a \approx 1$ ), critical coupling occurs at symmetric coupling ( $k_1 = k_2$ ). For a lossy resonator, critical coupling occurs when the losses match the coupling coefficients such as  $r_2 a = r_1 = r$ .

### 2.2.2c. Spectral characteristics

As explained in **chapter I**, in the aim of this work, **resonances of RR are used to perform optical to electrical conversion**. This process realizes an equivalent microwave photonic filter (MPF) (frequency around 15 GHz as one of the targets of our work). The properties of the MPF therefore is relevant to the optical signal of the RR. For this reason, in the following of this section, the transmission spectrum of RR will be studied, including its figure of merits and the condition required to perform opto / RF

## 2.2. Silicon micro-ring resonators

conversion. The typical transmission spectrum for all-pass (a) and add-drop (b) RR are described in **Fig.2.2.4 (a)** and **(b)**, respectively.

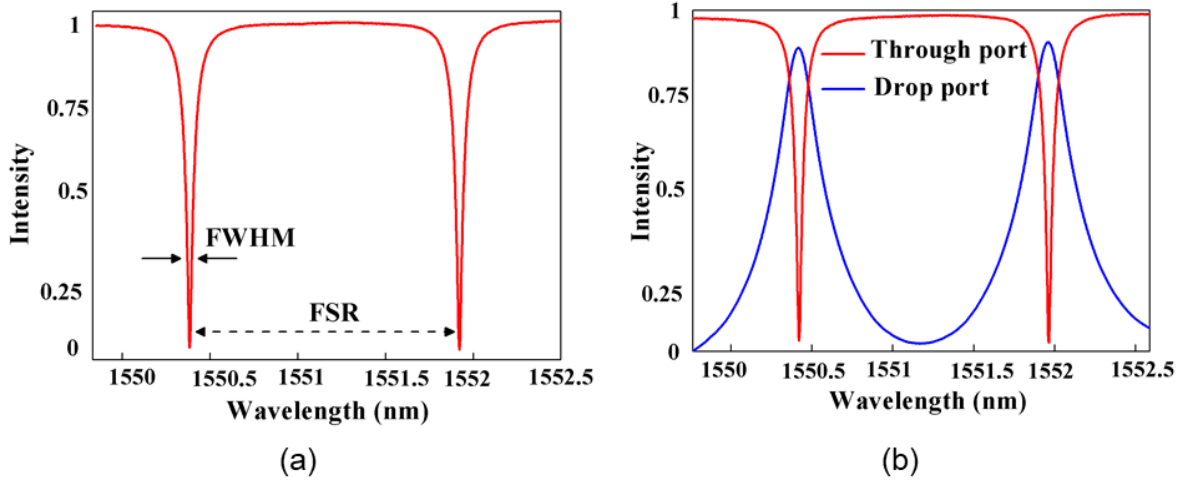


**Fig.2.2.4.** Example of transmission spectrum of (a) all-pass and (b) add-drop RR.

One important figure of merit of the transmission spectra of RR is the **free spectral range (FSR)**, which is defined by the frequency (or wavelength) difference between two successive resonance peaks. FSR takes the following expressions <sup>198</sup>.

$$FSR_{\lambda} = \frac{\lambda^2}{n_g L_{tot}} \text{ (nm)} \quad (2.2.4a)$$

or

$$FSR_f = \frac{c}{n_g L_{tot}} \text{ (Hz)} \quad (2.2.4b)$$

, with  $n_g$  the waveguide mode group refractive index. For the target frequency around 15 GHz and considering  $n_g = 3.1$ , we find  $L_{tot} \approx 6$  mm.

Another important parameter is the resonance width, which is defined as the full width at half maximum (FWHM) or 3 dB bandwidth of the resonance line shape. FWHM can be deduced through the resonance spectrum.

$$\text{For all-pass ring: } FWHM = \frac{(1-ra)\lambda_{res}^2}{\pi n_g L_{tot} \sqrt{ra}} \quad (2.2.5a)$$

$$\text{For add-drop ring: } FWHM = \frac{(1-r_1 r_2 a)\lambda_{res}^2}{\pi n_g L_{tot} \sqrt{r_1 r_2 a}} \quad (2.2.5b)$$

As described in chapter I, the quality factor of a microwave filter  $Q_{RF}$  is an important parameter driving the stability and the performance of the generated

microwave signals. It is noteworthy that the *FWHM* of the optical signal is preserved in the microwave frequency domain <sup>61</sup>. Moreover, the *FWHM* of the optical signal is related with the optical quality factor  $Q_{opt}$  by equation <sup>187</sup>.

$$Q_{opt} = \frac{\lambda_{res}}{FWHM} \quad (2.2.6)$$

From **Eq. (1.1.4)** and **Eq. (2.2.6)**, it is easy to find the equivalent loaded optical quality factor  $Q_{opt}$  related with the  $Q_{RF}$  of the converted signal by  $Q_{RF}/Q_{opt} = f_{RF}/f_{opt}$  (**2.2.7**), where  $f_{opt}$  is the frequency corresponding with the resonance wavelength of the resonator (at about 194 THz). From **Eq. (2.2.7)**, we can see that the equivalent  $Q_{RF}$  of an optical resonator is directly proportional to the optical quality factor  $Q_{opt}$  and to the ratio of  $f_{RF}/f_{opt}$ . Since the targeted frequency  $f_{RF}$  of our work is around 15 GHz (meaning  $f_{RF}/f_{opt} \sim 7 \times 10^{-5}$ ), it is easy to find that in order to obtain the MPF with consideration quality factor  $Q_{RF} > 10$ , the optical resonance needs to have  $Q_{opt}$  at or above  $10^5$ .

The plot of optical quality factors as a function of the resonator length for different light propagation loss levels  $\alpha$  (dB/cm) are shown in **Fig.2.2.5 (a)** and **(b)** for an all-pass and add-drop ring, respectively (assuming  $r_1 = r_2 = r = 0.99$ , and  $n_g = 3.1$  at 1.55  $\mu\text{m}$  wavelength).

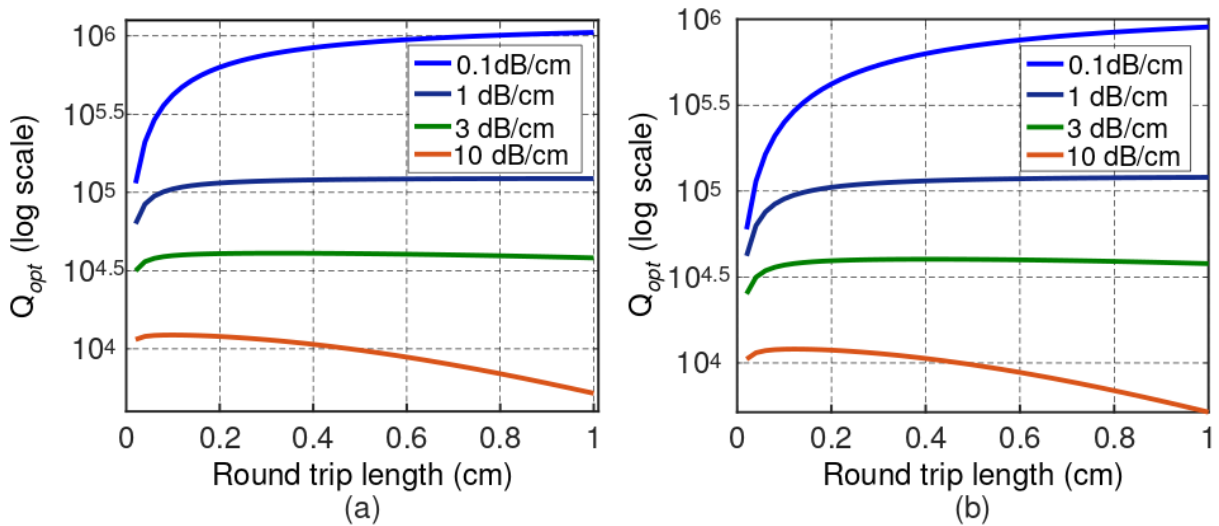


**Fig.2.2.5.** Quality factor as function of perimeter length for different propagation loss in (a) all - pass configuration and (b) add - drop ring configuration.

The physical meaning of the  $Q_{opt}$  factor relates to the number of round-trips made by the energy in the resonator before being lost to internal loss and the bus waveguide.

## 2.2. Silicon micro-ring resonators

Obviously, the best  $Q_{opt}$  values are obtained when the resonator length  $L_{tot}$  is large and round-trips losses are small. However, these two terms, i.e. the propagation losses and the resonator length are not independent since the accumulated propagation losses increase with the resonator length. As can be seen in **Fig.2.2.5**, for small propagation losses (in case of 0.1 dB/cm and 1 dB/cm), the accumulated loss level remains small, thus  $Q_{opt}$  increases when the perimeter length is increased. However, when propagation losses are large (10 dB/cm), the accumulated losses in the ring increase rapidly with resonator length, which then results in the saturation of  $Q_{opt}$ . Moreover, in case of propagation losses at 3 dB/cm, the calculated  $Q_{opt}$  is less than  $10^5$  for both all-pass and add-drop ring resonators at around 6.5 mm of  $L_{tot}$  (approximate resonator length in this work).

From all the above arguments, it can be understood that controlling low propagation losses in long perimeter length resonator is an important task for the realization of an integrated OEO. Efforts have thus been made to improve the fabrication processes in order to reduce loss factors including the waveguide sidewall roughness and the RR directional coupler(s) losses to obtain high  $Q_{opt}$ -resonances. We will discuss in the detail the fabrication of RR in section 2.4 of this chapter.

On the other hand, taking into account the fact that  $Q_{opt}$  describes the amount of energy stored inside the ring, and that this is directly related with the light power transferred from the bus waveguide to the ring in the directional coupler region, we take hereafter a specific interest in the design of the RR directional coupler.

### 2.2.2d. Directional coupler

In the two RR configurations, a directional coupler is used to transfer light from the input waveguide to the ring. This process can be described through the Coupled Mode Theory <sup>198–200</sup>. Here, a simple directional coupler in an all-pass ring configuration is considered.

Basically, the directional coupler consists of two parallel waveguides (**Fig.2.2.6a**), where the coupling coefficient is controlled by both the length of the coupler  $L_c$  and the spacing between the two waveguides  $d$  <sup>184</sup>. When two parallel waveguides are placed in

close proximity, optical power can be exchanged between them <sup>198,200</sup>. The coupling of light between the bus waveguide and the ring can be separated in three types including under-coupling, critical-coupling and over-coupling behaviors. Under-coupling occurs when the resonator round trip loss exceeds the cross-coupling strength ( $k^2 < 1 - a^2$ , i.e.  $r > a$ ). Over coupling occurs when the resonator round trip loss is smaller than the cross-coupling strength ( $k^2 > 1 - a^2$ , i.e.  $r < a$ ). These two behaviors result in less power coupled from the bus waveguide into the ring, which consequently results in less power stored inside the resonator. In the intermediate **critical coupling regime**, when the cross-coupling strength equals the resonator round trip loss ( $k^2 = 1 - a^2$ , i.e.  $r = a$ ), the number of round-trips that light achieves inside the ring is maximized and the ring  $Q_{opt}$  is maximized (see relationship (2.2.5a) that shows that FWHM theoretically vanishes when  $r = a$ ).

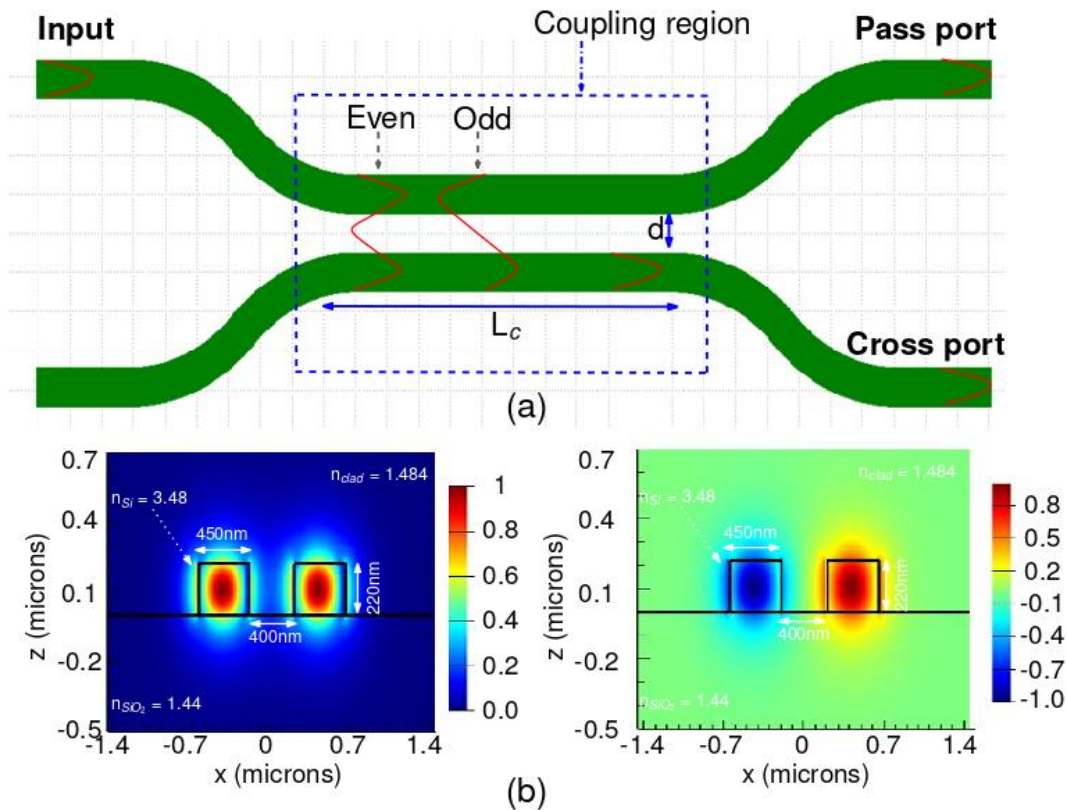


**Fig.2.2.6.** (a) Schematic of the super-mode theory of waveguide directional coupler and (b) example of symmetric (even) and asymmetric (odd) modes calculated from an optical mode solver at  $1.55 \mu\text{m}$  wavelength for a typical SOI waveguide configuration.

The directional coupler waveguide/waveguide coupling behavior can be interpreted as an interference between the symmetric (even) and asymmetric (odd)

## 2.2. Silicon micro-ring resonators

super-modes (**Fig. 2.2.6**). They exist in both TE and TM polarizations. When light in TE (TM) polarization is launched into one input waveguide, the two even and odd (super-) modes are excited simultaneously. In general, the even and odd super-modes possess different propagation constants. If all the power is initially in one waveguide, the field distribution can be represented as one particular superposition of the even and odd super-modes adding coherently in that waveguide's core <sup>184,198</sup>. Since these two super-modes have different phase velocities, over some length, they accumulate an additional relative phase shift of  $\pi$ . In other words, the sum of the modes becomes a difference between the mode fields, so that light is transferred in the nearby adjacent waveguide. This process continues back and forth while the two waveguide cores remain in close proximity (distance  $\sim\lambda/2$ ).

The fraction of power coupled from one waveguide to the another can be expressed as:

$$k^2 = \frac{P_{cross}}{P_{in}} = \sin^2(C_{coup} \cdot L_c) \quad (2.2.8)$$

, where  $P_{in}$  is the input power,  $P_{cross}$  is the power coupled across the directional coupler,  $L_c$  is the coupler length and  $C_{coup}$  is the coupling coefficient. Assuming a lossless coupler and identical coupled waveguides, the fraction of the power remaining in the input waveguide is:

$$r^2 = (1 - k^2) = \cos^2(C_{coup} \cdot L_c) \quad (2.2.9)$$

The coupling coefficient calculated based on “super-modes” analysis (which can rely on simple numerical calculations of the reflective index  $n_{eff1}$  and  $n_{eff2}$  of the first even and odd modes of the set of coupled waveguides) is:

$$C = \frac{\pi \cdot \Delta n_{eff}}{\lambda} \quad (2.2.10)$$

So, finally, the beating length describing the needed length to fully transfer light power from one waveguide to the adjacent twin one is given by  $L_b = \lambda/(2\Delta n_{eff})$  (**2.2.11**).

In case  $L_c/L_b \neq 1$ , light power is not fully transmitted and the self and cross-coupling power transmissions can be rewritten as:

$$k^2 = \sin^2(C_{coup} \cdot L_c) = \sin^2\left(\frac{\pi \cdot \Delta n_{eff}}{\lambda} \cdot L_c\right) = \sin^2\left(\frac{\pi}{2} \cdot \frac{L_c}{L_b}\right) \quad (2.2.12a)$$

$$r^2 = \cos^2(C_{coup} \cdot L_c) = \cos^2\left(\frac{\pi \cdot \Delta n_{eff}}{\lambda} \cdot L_c\right) = \cos^2\left(\frac{\pi}{2} \cdot \frac{L_c}{L_b}\right) \quad (2.2.12b)$$

These relationships, obtained from fairly strong hypotheses (no loss and waveguide/waveguide coupling of light over a well-defined  $L_c$  length whereas in a real directional coupler structure, the proximity zone of the two guides is first progressive before the two guides are parallel to each other), nevertheless give the general shape of the waveguide/ring coupling coefficients and have been useful for the designs performed in this thesis.

Indeed, as indicated above, the realization of an effective microwave bandpass filter MPF condition within the loop of an optoelectronic resonator oscillator requires very high optical quality factors. The relationship (2.2.12b) is then very useful for sizing RR operating close to the critical coupling condition. Recasting  $r = a$  indeed gives:

$$\frac{L_c}{L_b} = \frac{1}{\pi} \cos^{-1}(2 \exp(-\alpha \cdot L_{tot}) - 1) \quad (2.2.13)$$

This relationship thus finally shows that the ring directional coupler coupling length ( $L_c$ ) can be designed according to the expected waveguide losses ( $\alpha$ ).

Thanks to the high index contrast between silicon and its oxide, SOI waveguides with submicron dimensions can be fabricated based on classical techniques, e.g. e-beam lithography and inductive coupled plasma (ICP) or reactive ion etching (RIE). In this case, propagation losses arise due to the interaction of the optical mode with the waveguide sidewall surface roughness. For small micro-ring, the round-trip loss yet remains acceptable in all cases. The ring critical coupling condition then reveals a weak dependence on the exact value of the loss coefficient  $\alpha$ . On the contrary, when the ring radius is large, the round-trip loss  $\alpha \cdot L_{tot}$  grows as soon as the waveguide losses increase, and its precise value can be hardly predicted accurately as it is case to case process dependent, making the critical condition more difficult to fulfil from design guidelines. The approximate critical condition  $L_c/L_b$  calculated for different waveguide loss levels ( $\alpha$ ) and different unfolded ring lengths, considering a SOI waveguide cross-section with

## 2.2. Silicon micro-ring resonators

350 nm waveguide width, 220 nm waveguide height, 1.484 cladding index for the TM mode operating at 1.55  $\mu\text{m}$  wavelength are shown in **Fig.2.7**.

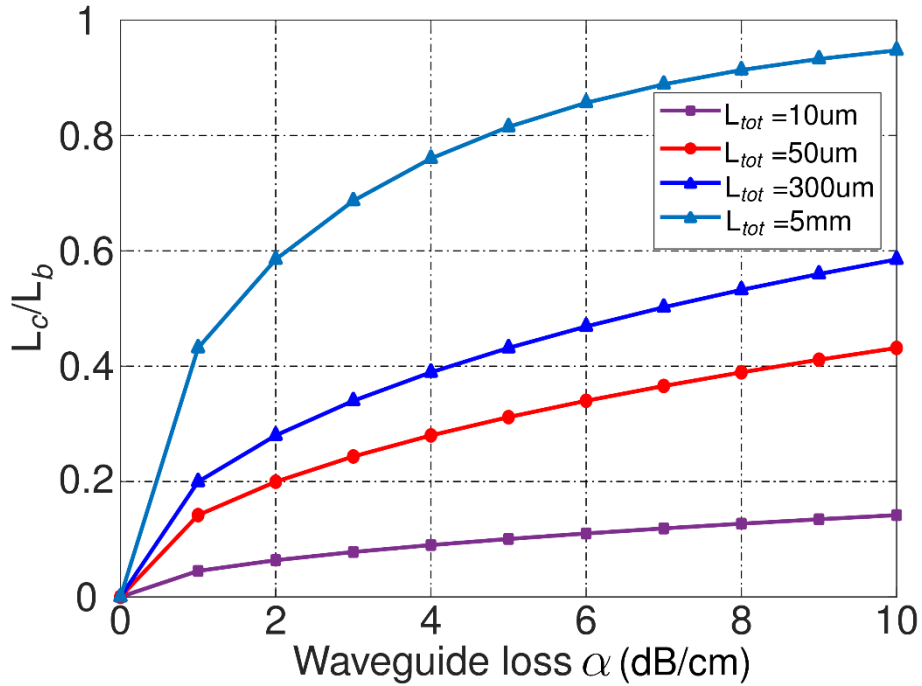


**Fig.2.2.7.**  $L_c/L_b$  ratio corresponding to a RR critical condition calculated from Eq. (2.2.13) as function of waveguide loss and for different resonator lengths.

In the presently studied configuration, it can be seen from **Fig2.2.7** that with the fabrication accuracy that we have for strip waveguides, the most probable  $\alpha$  value are in the 1 dB/cm to 5 dB/cm. In this loss values range, we see that an uncertainty of  $\alpha$ , namely from  $\alpha = 1$  dB/cm to  $\alpha = 4$  dB/cm leads to a variation of  $L_c/L_b$  for  $L_{tot} = 5$  mm from around 0.4 to around 0.84, while the  $L_c/L_b$  variation for  $L_{tot} = 50 \mu\text{m}$  is from around 0.045 to around 0.14. So, overall, in the long ring case, not knowing the exact waveguide loss value can lead to a much strong error in the critical condition. This can explain why critically coupling long

RRs is generally speaking more difficult than for small ones. As explained hereafter in section 2.3, we faced this difficulty by benchmarking our fabrication processes through the fabrication of various  $L_c/L_b$  directional couplers while tuning directional coupling gap to control the beating length around  $\lambda = 1.55\mu\text{m}$ .

In the next section, we describe in a more detailed fashion the simulation and design strategy applied to obtain RR suited to the realization of an optoelectronic oscillator.

## 2.3. Silicon micro-ring resonator design

In the aim of this work, RRs were considered for their integration in OEO loops with an operating frequency at or around 15 GHz and suitable for bulk index sensing application. The design of RR that took into account this guideline is described in the following of this chapter.

### 2.3.1. Waveguide chosen parameters

Starting from a SOI wafer with a 2  $\mu\text{m}$  buried oxide and a 220 nm silicon thin film, a strip waveguide geometry operating in TM light polarization was designed by following two main guidelines: i) Being single-mode and 2) Maximizing the sensitivity to the top cladding material.

As explained in sections 1.3.1 and 2.1.2, in the configuration of a RR integrated within an OEO loop, any refractive index change of the top cladding material ( $n_{clad}$ ) can induce a modification of the loop generated RF frequency through a modification of the RR FSR. The frequency sensitivity to the bulk refractive index can therefore be calculated as follows:

$$S = \frac{\partial FSR}{\partial n_{clad}} \quad (2.3.1)$$

As indicated in section 2.1.2, the possibility for the small detectable bulk refractive index changes is related to a high sensitivity. Therefore, the chosen waveguide parameters were optimized by looking for the possibility of the highest of RR FSR change due to the cladding refractive index change. Accordingly, by using an optical mode solver, we calculated  $S$  as function of waveguide width ( $w$ ) with variation of cladding refractive index in range of 1.3 – 1.4 (refractive index range of the most BioSolutions), assuming a resonator length equal to 5.8 mm (see next section) operating

### 2.3. Silicon micro-ring resonator design

in TM light polarization at around 1.55  $\mu\text{m}$  wavelength. The variation of waveguide width was limited in range 250 – 600 nm for TM-single mode operation.

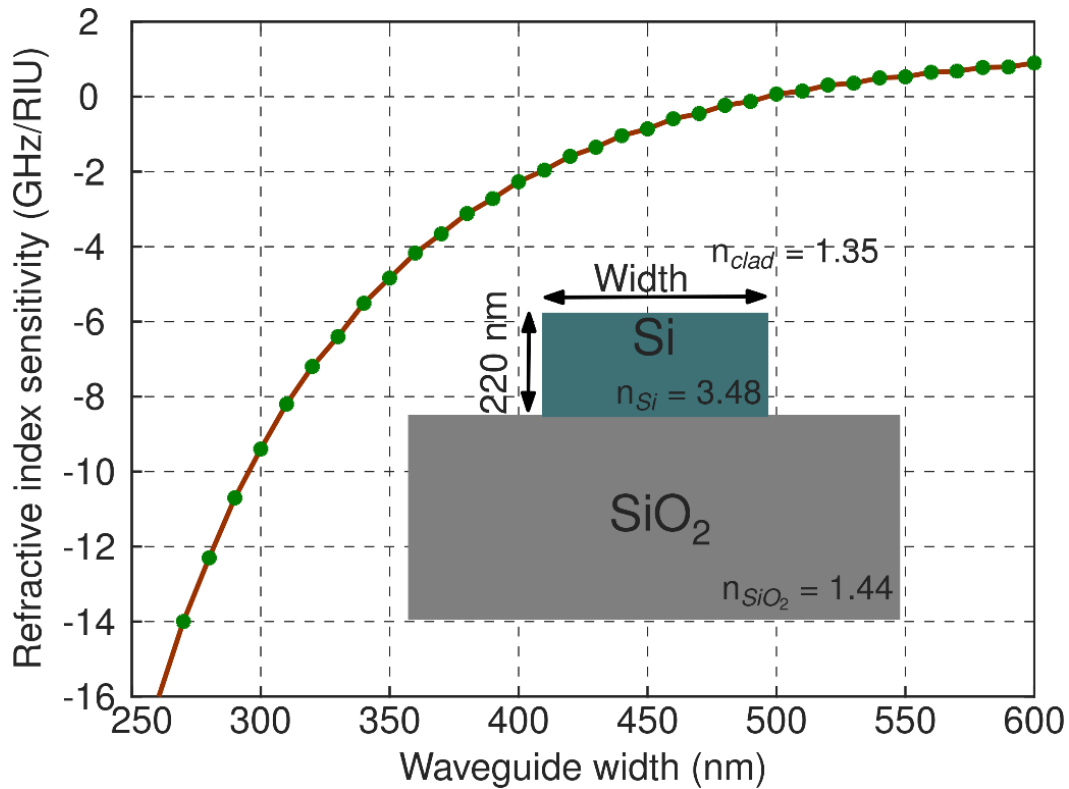
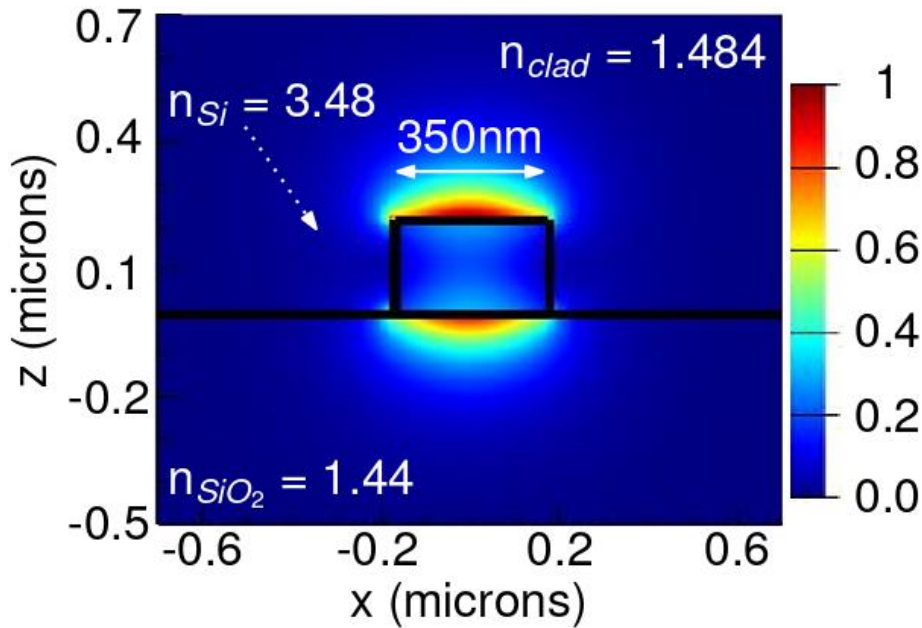


Fig.2.3.1. Refractive index sensitivity as function of waveguide width.

From **Fig.2.3.1**, we observe a frequency sensitivity decrease when the waveguide width increases. The underlying reason is that smaller cross-section waveguides have less confined modes into the core region and a large portion of the evanescent field then spreads outside the core, thus resulting in a stronger interaction with the cladding material. However, an excessive reduction of waveguide core makes the control of the waveguide dimension more difficult <sup>201–203</sup>. For that reason, the **waveguide width was fixed at 350 nm** leading to a theoretical bulk sensitivity of around 4 GHz/RIU.

In the performed experimental studies of RR, the optical signal was first characterized with RR with PMMA as the cover cladding ( $n_{PMMA} = 1.484$  at  $\lambda = 1.55\mu\text{m}$ ). The electric field distribution for the TM mode of the retained strip waveguide is finally shown in **Fig.2.3.2**.



**Fig.2.3.2.** Electric field energy distributed for TM mode of strip waveguide at 1.55  $\mu\text{m}$  wavelength.

At the wavelength of 1.55  $\mu\text{m}$ , the chosen strip waveguide is single mode in TM polarization, with an effective index value  $n_{eff} = 1.671$  and a group index  $n_g = 3.148$ . The confinement factor in the cladding material of this mode was calculated at 20.3 %. For the target frequency around 15 GHz, the **corresponding RR length is of few millimeters**. This constraint leads to a rather unusual long length ring for which controlling low optical losses and minimizing the occupied footprint are not straightforwardly obvious tasks (such a structure can occupy an area around one or few  $\text{mm}^2$ ). Therefore, a structure with small device size would facilitate a higher level of integration. With this aim in mind, we implemented a spiral shape RR, as good candidates to generate long perimeter RR with small footprints.

Because the spiral shape is typically formed by a series of bended curves, bending loss therefore is an important factor contributing to the total loss of the RR. Nevertheless, given the high contrast in the index of SOI optical guides, radii of curvature of more than a few microns lead to a spectacular minimization of guide losses. As a **very conservative value, a bending radius of 20  $\mu\text{m}$  was considered** for the design of the ring resonator in a spiral form.

### 2.3.2. Final design of the RR directional coupler

The main part of the design process for the RR directional coupler has been presented previously in section 2.2.2d. By adapting this methodology to the geometry of the selected strip waveguides, we have first estimated the beating length as a function of the directional coupler gap, as shown in **Fig.2.3.4** and in the **Table 2.3.1**.

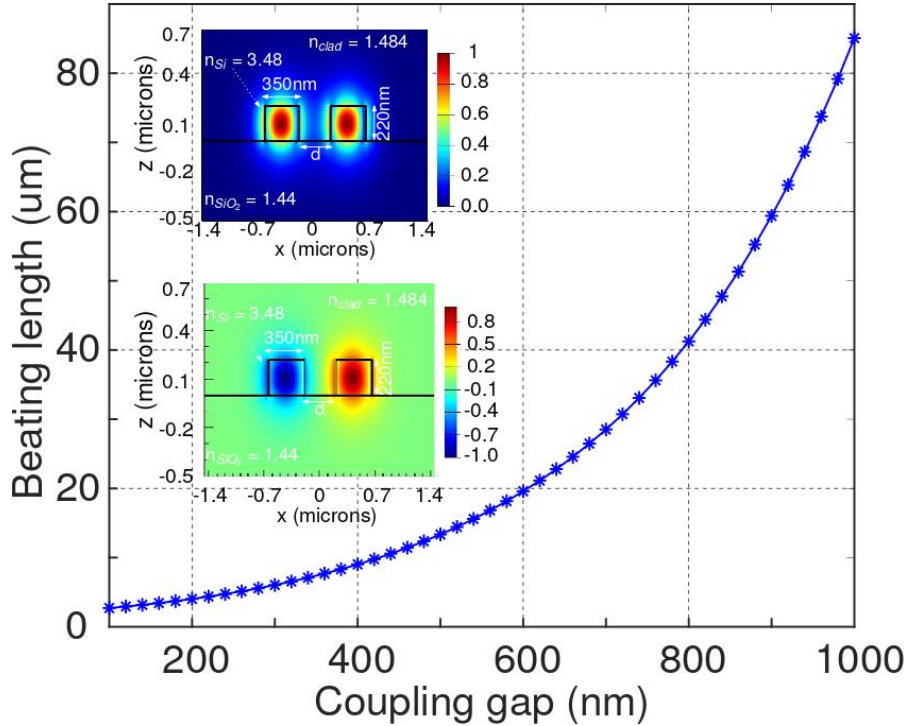


**Fig.2.3.4.** The beating length  $L_b$  calculated as function of coupling gap  $d$  (SOI waveguide geometry:  $h = 220$  nm,  $w = 350$  nm,  $n_{PMMA} = 1.484$ , TM waveguide operate at  $1.55$   $\mu\text{m}$ ).

Using an optical mode solver, we estimated the effective refractive index of the two even and odd TM super-modes in the coupling region, the beating length  $L_b$  being then calculated using Eq. (2.2.11). As observed in **Fig.2.3.4a**,  $L_b$  increases dramatically when the coupling gap increases. Thus, long coupling length is needed for large coupling gaps. For this reason, the intermediate coupling gap in the 200 – 400 nm range was chosen in order to maintain beating lengths at small values and to minimize the directional coupler footprint. **Table 2.3.1** gives detailed beating length values in the 200-400nm gap range.

**Table 2.3.1.** Beating length calculated for different coupling gaps (SOI waveguide:  $h = 220$  nm,  $w = 350$  nm,  $n_{\text{PMMA}} = 1.484$ , TM waveguide operate at  $1.55$   $\mu\text{m}$ ).

Coupling gap (nm)	200	300	400
Beating length ( $\mu\text{m}$ )	4.0	6.0	9.0

**Eq. (2.2.13)** was used to give an order of magnitude of coupling lengths related to coupling gap and possible waveguide losses for an all-pass RR. Based on **Eq. (2.2.15)**, the different coupling lengths related with coupling gaps and the possible waveguide losses were calculated, assuming a resonator length of  $5.8$  mm. A list of devices with different combinations of coupling gaps/coupling lengths were designed while maintaining the total length of the resonator constant to match with the desired FSR, as described in the next section.

### 2.3.3. Full ring resonator design strategy

The spiral shape RR was designed in a maximum footprint of  $500$   $\mu\text{m} \times 500$   $\mu\text{m}$ , for being compatible with the main deflection field of the electron beam lithography system available in our laboratory.

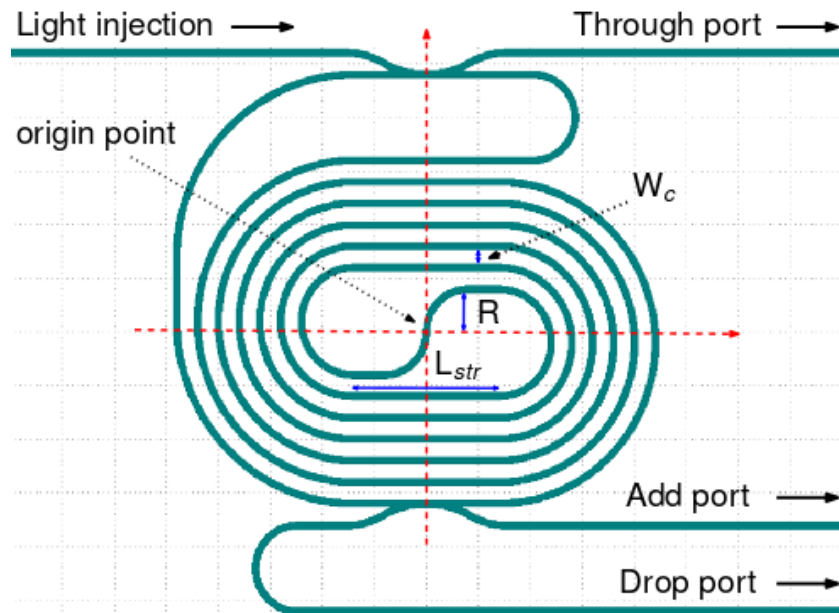


**Fig.2.3.5.** Design structure of spiral add-drop RR,  $R$ : smallest bending radius,  $W_c$ : spacing between two successive turns,  $L_{str}$ : length of straight path length in the spiral shape.

### 2.3. Silicon micro-ring resonator design

We designed the spiral RR by starting around an origin point and defined from it a  $(x,y)$  cartesian coordinate system. Our spiral shape was built up by two interleaved spiral branches which connect together through the straight path length and symmetrically through the  $y$  axis of the Cartesian system. An overview of the final spiral RR retained geometry is shown in **Fig.2.3.5**.

In **Fig.2.3.5**,  $L_{str}$  is the length of the straight path,  $R$  is the smallest bending curve and  $W_c$  is a uniform spacing between two successive turns. The value of  $W_c$  was chosen in order to take into account the proximity effects of the e-beam lithography system which can have an impact when dense patterns with closely positioned features are fabricated<sup>204</sup>. From the fabrication results, we found that with  $W_c$  at  $20\ \mu\text{m}$ , the proximity effect could be avoided. Hence,  $W_c = 20\ \mu\text{m}$  was chosen. As indicated in section 2.3.2, the smallest bending radius  $R$  was also fixed at  $25\ \mu\text{m}$  in order to minimize bending losses. The final design included seven half circles in each side.  $L_{str}$  was fixed at  $102\ \mu\text{m}$  for the final optical path length of  $5.8\ \text{mm}$ .

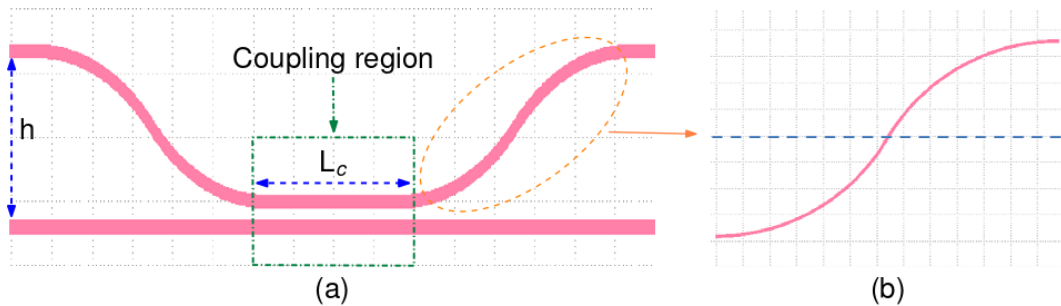


**Fig.2.3.6.** Design structure of the directional coupler.

The coupler shape was designed to allow the flexible modification of coupling length/coupling gaps while maintaining the resonator total length  $L_{tot}$  at a given value. The coupler was formed by using two bended curves connected together through a straight path waveguide and in conjunction with the outermost straight path of the spiral. Each bended curve formed by two opposite bends are showed in **Fig. 2.3.6(b)**. With this design structure, the coupling length  $L_c$  and also the coupling gap  $d$  were easily modified without impact into the spiral length (as can be seen in **Fig.2.3.7**). Thus, a series of RR with a variation of coupling gap/coupling lengths could be made.

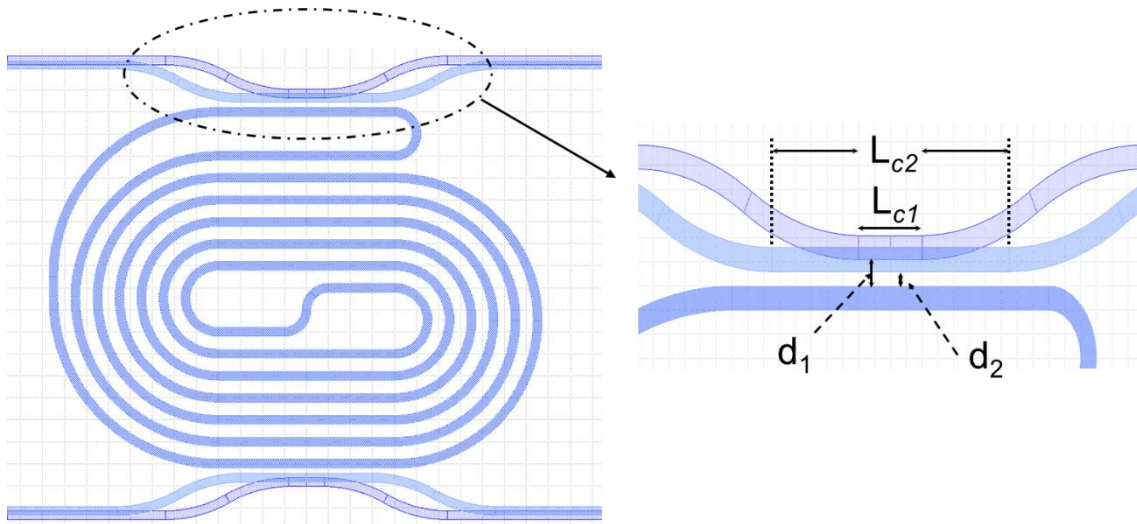


**Fig.2.3.7.** Schematic of spiral RRs illustrate for the flexibility variation of combination of  $L_c/d$  (here  $L_{c1}/d_1$  and  $L_{c2}/d_2$ ) while maintain the spiral length.

## 2.4. Fabrication processing of micro-ring resonators based on the Si technology

In silicon photonics, injection/collection of optical signals into the chip is enabled by edge couplers and Si grating<sup>205–207</sup>. In terms of ease of fabrication, CMOS compatible as well as wafer-scale testability, surface grating couplers are by far the most preferred scheme of the coupling to integrated circuits<sup>208,209</sup>. For that reason, in the full design of our RRs, the grating couplers were used to coupled light to and from optical fiber. A SEM image of grating coupler is shown in **Fig.2.4.3d**. The dimensions of grating couplers were designed for properly obtaining the highest optical transmission at 12.5 dB for TM propagation at 1.55  $\mu\text{m}$  wavelength. Identical gratings were placed at output ports to extract light from the samples. From the gratings, 800  $\mu\text{m}$  tapers were used to guide light to the single mode strip waveguide and from strip waveguide to the output port, respectively. The 350 nm single mode strip waveguide was designed with a length of 8 mm in order to serve the sensing measurement later performed.

Devices were fabricated by following two main steps. The first step was the generation of devices using a series of python codes (mask preparation), and the second

## 2.4. Fabrication processing of micro-ring resonators based on the Si technology

consisted in the sample fabrication itself that was performed at the C2N-Orsay clean room with the strong support of Xavier Le Roux.

### 2.4.1. Description of the passive Si structures fabrication process

The fabrication process flow that was used for the fabrication of the designed ring resonators is shown in **Fig.2.4.1**.

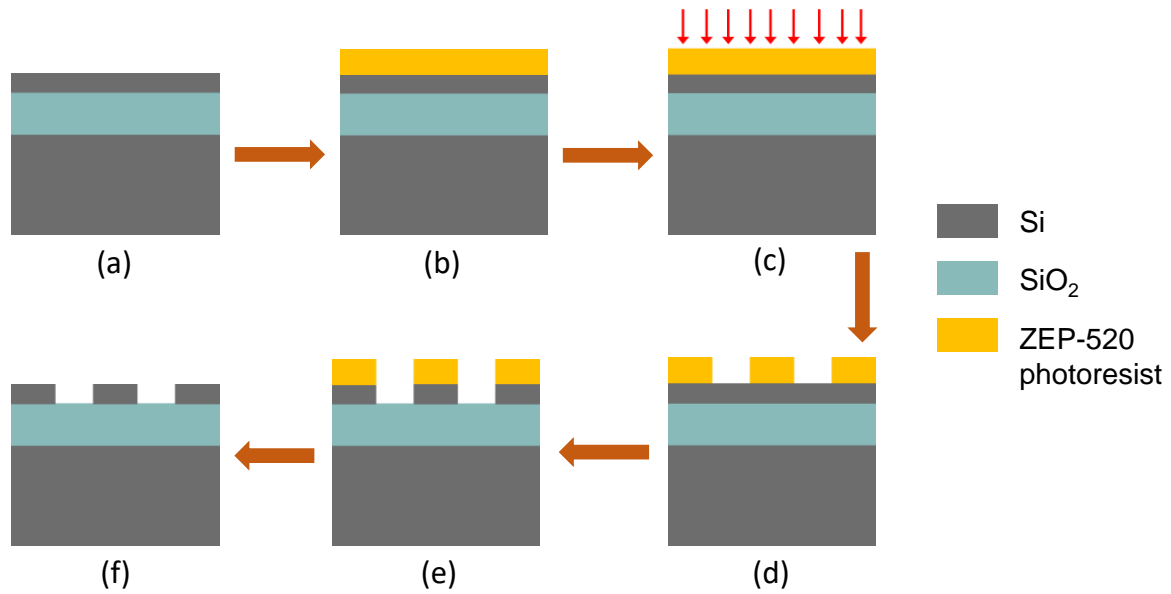


**Fig.2.4.1.** SOI RR fabrication process applied within the C2N clean room for the fabrication of the silicon photonic samples: (a) Preparation of SOI wafer, (b) ZEP-520A photoresist deposition, (c) E- beam lithography, (d) Development, (e) Etching and (f) Cleaning step

Beside optimizing fabrication steps to control fabrication results, the preparation of sample masks was first achieved. In the next section, we describe the method that was used to prepare them.

Fabrication of samples started from a SOI substrate with a 220 nm silicon thickness and a 2 μm buried oxide. First, a positive photoresist ZEP-520A was diluted in anisole and deposited on top of the full 2" wafer by spin-coating at 6000 rpm in order to obtain a uniform thickness of  $\approx 100$  nm (**Fig.2.4.2b**). The wafer was cleaved into small samples with  $2 \times 2$  or  $2 \times 4$  cm<sup>2</sup>. Then, each sample covered with photoresist was heated at 170°C for 3 minutes before the E-beam lithography step (**Fig.2.4.2c**). After E-

### 2.4.1. Description of the passive Si structures fabrication process

beam writing of the patterns, development of the resist by using the ZED-N50 developer for 40 seconds and one more 30 second in mixed solution consisting of Methyl isopropyl ketone (MIPK) + Isopropyl alcohol (IPA) in volume ratio at 1:3 was achieved. Then samples were rinsed by IPA before being dried under nitrogen flow. The development step is illustrated in **Fig.2.4.2d**. Following the development step, its etching step was carried out by using Inductive coupled plasma etching (ICP), as shown in **Fig.2.4.2e**. The features were transferred by an Inductive Coupled Plasma (ICP) reactive ion etching process using Sulfur hexafluoride SF<sub>6</sub> and Octafluorocyclobutane C<sub>4</sub>F<sub>8</sub> gas. The ICP etching process was optimized, taking into account the different coils, the injected gas flux and etching time. The sample was then immersed in Piranha (H<sub>2</sub>SO<sub>4</sub>:H<sub>2</sub>O<sub>2</sub> with the ratio 3:1 in volume) solution to remove all remaining resist traces and one last step of plasma O<sub>2</sub> was applied to eliminate the remaining C<sub>4</sub>F<sub>8</sub> thin film (**Fig.2.4.2f**).

## 2.4.2. Mask preparation for E-beam lithography

E-beam lithography (EBL) is one of the versatile lithographic tools that is widely used to create patterns at the nanoscale. The EBL working principle is relatively simple and very similar to photolithography: a focused beam of electrons is scanned across a substrate covered by an electron-sensitive material (photoresist) that changes its solubility properties according to the energy deposited by the electron beam. Areas exposed, or not exposed according to the tone of the resist, are removed by a development step <sup>210</sup>. The advantage of EBL compared to photolithography is that it does not require masking. Through a Python scripting interface, the geometrical designs of the desired devices with chosen parameters were generated in the form of a *.gds-II* file. The EBL was then used with a proprietary software converter (*nbPat 2.39* in our work) to translate the *gds-II* data into a machine-exposable *.npf* file. The *.npf* file provided pattern manipulation functions such as main-field and subfield fracturing and shape biasing (**Fig.2.4.2**). It also provided a viewer so that the fracturing results could be checked. It is worth noting that taking into account the variation between design and fabrication result, the final devices were designed with 50 nm bigger waveguide widths and 50 nm smaller coupling gaps in order to obtain target parameters after the final fabrication step.

## 2.4. Fabrication processing of micro-ring resonators based on the Si technology

There are two main types of electron beam lithography systems: the point-beam type and the variable-shaped beam ones <sup>211</sup>. Our work used the Nanobeam *nB4* from Nanobeam Limited in UK. It is the point-beam type EBL system <sup>212</sup>. The achieved RR designs were prepared for being fabricated in 500  $\mu\text{m}$  x 500  $\mu\text{m}$  main fields consisting of a 2D grid of 10  $\mu\text{m}$  x 10  $\mu\text{m}$  size subfields. When the system started to operate, the beam was exposed in each subfield until completing one main-field before moving to another adjacent main-field. Because the pattern dimensions needed more than one writing field exposed, the fields were stitched together via stage movement. The deviation from the perfect alignment between consecutive writing subfields or main fields could result into stitching errors, which could consequently affect the waveguide roughness of fabricated waveguides or even their continuity in the worst cases. One possible way to reduce stitching errors (which was verified several times) consisted in to regenerating *.npf* files while ensuring that spiral RR shapes were well located in one main-field (Fig.2.4.2a) and waveguide patterns were located in the center of a subfield (Fig.2.4.2b).

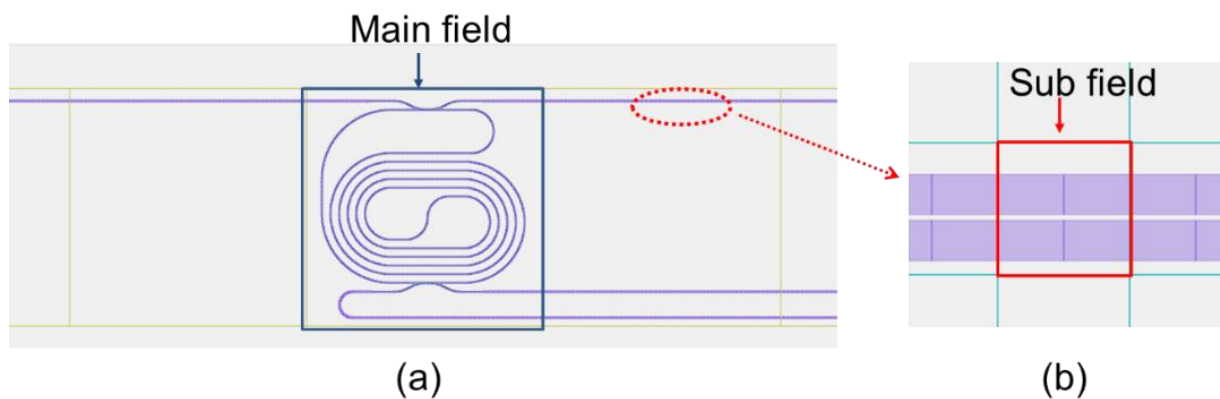


**Fig.2.4.2.** Example of *.npf* file including (a) RR shape inside 500 $\mu\text{m}$ ×500 $\mu\text{m}$  main-field consisting of (b) 10  $\mu\text{m}$  x 10  $\mu\text{m}$  size subfields.

Although *.npf* files were modified in order to reduce fabrication roughness, during fabrication, another problem was also recognized (Fig.2.4.3c), resulting in an un-fully etching of coupling gaps. We observed in fact that the electron beam of our e-beam writer tended to preferentially draw first the smallest lengths or widths of the exposed polygons. The design of coupling regions including  $\mu\text{m}$  long coupling length with only few hundreds nm of coupling gaps, patterns were preferentially exposed initially in the

direction perpendicular to the propagation of light (e.g. along  $y$  in **Fig.2.4.3a**). If any defect occurred during the writing process, the beam writing could jump-up without exposing some small regions, a discontinuity along the coupling gap or simply by the appearance of defects leading to surface roughness responsible for high propagation losses could occur (**Fig.2.4.3c**). To avoid these defects, we tried to guide the beam writing along the propagation of light (e.g. along  $x$  in **Fig.2.4.3b**). To do so, a list of successive polygons with  $x$  size lengths smaller than the  $y$  size ones to form the coupling region (**Fig.2.4.3b**) was made. This approach was systematically applied through the Python scripting interface. The SEM image in **Fig.2.4.3d** shows a fabricated result after having applied this method as an example proof of the final correct result.

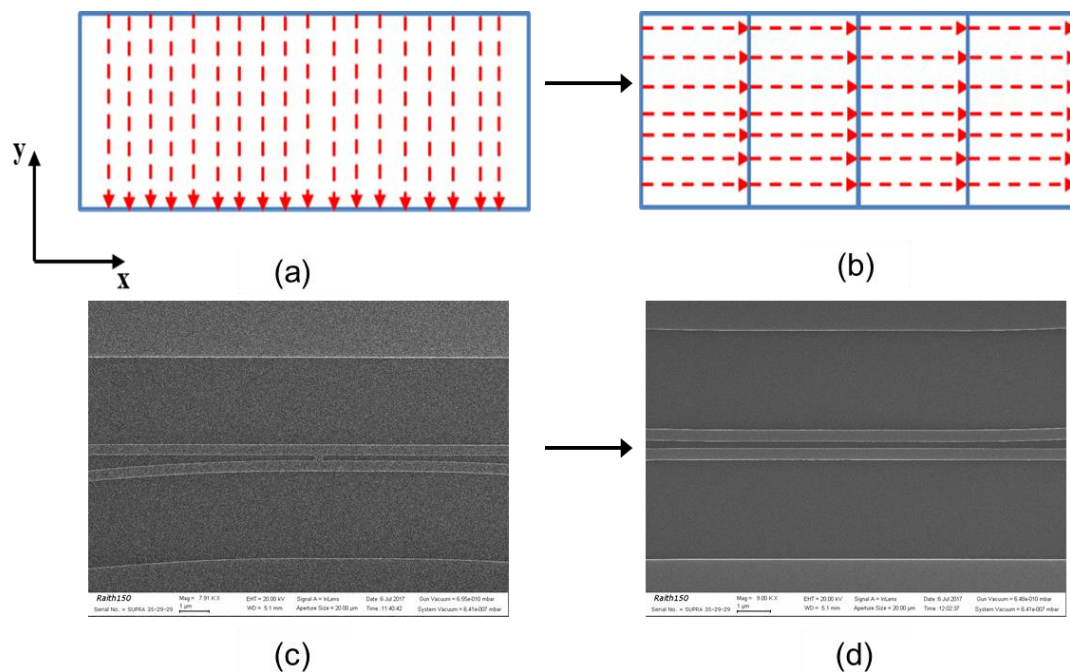


**Fig.2.4.3.** (a) and (b): Assume the writing mechanisms of e-beam lithography system along the coupling path length, the red line describes a direction of the beam moving stage, (c) Fabrication error in the coupling region, (d) Successful fabrication result after applying the empirical method to control the beam writing.

## 2.4.3. Fabrication results

Typical fabricated devices are illustrated in **Fig.2.4.4**. The main designed devices are shown in **Fig.2.4.4a**, each of them having different association coupling lengths/coupling gaps. We finally obtained uniform waveguide devices with a

## 2.4. Fabrication processing of micro-ring resonators based on the Si technology

waveguide width measured at 365 nm. The small difference observed between fabrication results and targeted waveguide width can be explained by fabrication imperfections. The zoom-in view shows that in the coupling region and grating coupler area, good fabrication results were obtained, i.e. qualitatively satisfying the targeted requirements.

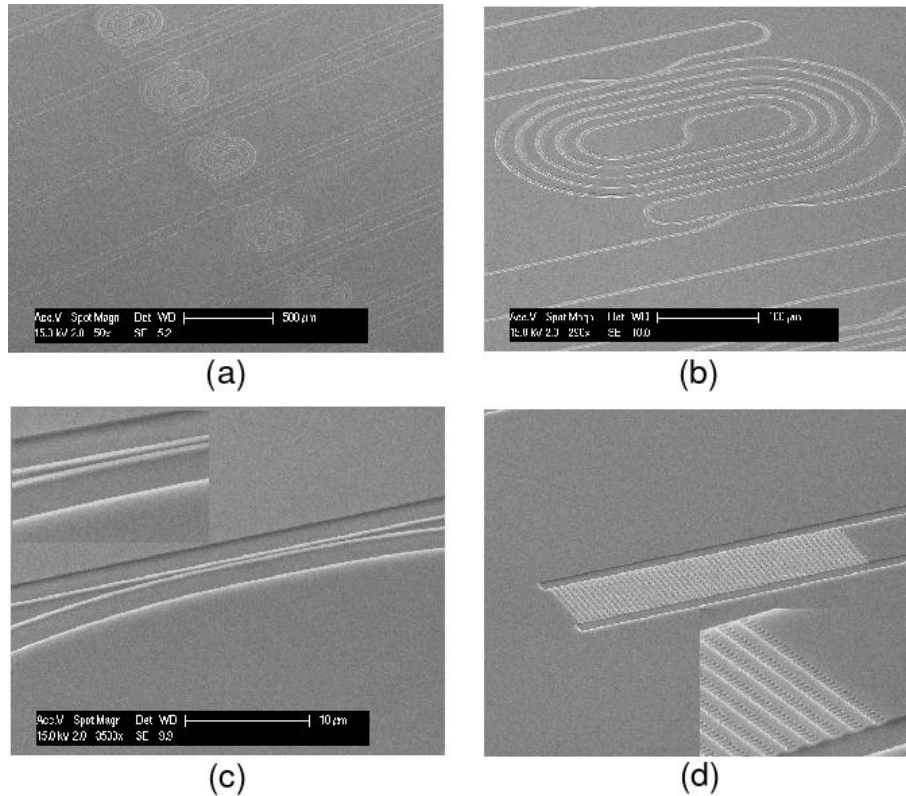


**Fig.2.4.3.** Fabrication result of spiral SOI RR. (a) of spiral rings fabricated in the sample, (b) zoom-in in one device, (c) Detail of coupling region, (d) Detail of grating coupler.

## 2.5. Optical characterization of spiral ring resonators

To confirm all the fabrication steps described above, optical characterizations of the photonic chips and ring resonators were then carried out. Light was injected and collected using the chip grating couplers. The grating angle was optimized for TM polarized waveguide mode excitation at 1550 nm wavelength (**Fig.2.5.2a**). The experimental setup for optical characterization of silicon RRs is shown in **Fig.2.5.1**.

## 2.5. Optical characterization of spiral ring resonators

Cleaved fibers were used for light input and output coupling and the fibers were mounted on a precision 3-axis translation stage. All devices were tested using a continuous wave (CW) tunable external laser beam coupled to the input waveguide through the input grating coupler with a properly adjusted coupling angle and extracted the same way from an output grating. For initial alignment, a CCD camera was used to position the fiber above the grating. Our experimental setup used CT400 All-Band Optical Component Tester as power detector. During the experiment, the signal at the output of the laser was first sent to the CT400 and then to a polarization controller before being coupled into the device through the grating coupler. Polarization controller was used to set the proper polarization at the input grating coupler. The output fiber was connected to the CT400 setup. CT400 collected signals from both the laser output and the device output. The collected signals then were sent to the computer in order to analyze the optical transfer function. The optical transfer function was determined by comparing the intensity of the output signal and the one received from output fiber. The employed setup comprised an automatic sweep and switch feature offering a nearly continuous (resolution of 1 pm) laser wavelength tuning in the 1500 nm -1600 nm wavelength range directly controlled through a computer interface.

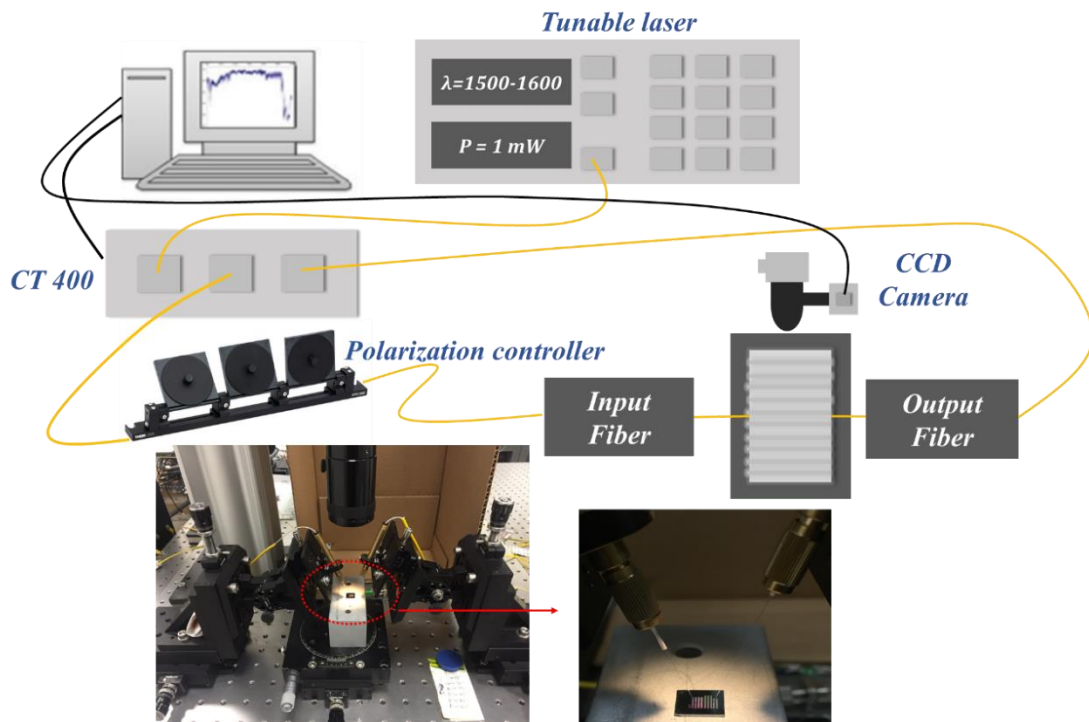


**Fig.2.5.1.** Experimental setup for optical characterization of Silicon RR.

## 2.5. Optical characterization of spiral ring resonators

We first measured the coupling efficiency of gratings. To do so, we performed transmission measurements on a waveguide with a grating coupler at both ends. Nearly adiabatic tapers were used to connect grating couplers with a single mode waveguide. The length of the taper was chosen as 800  $\mu\text{m}$  and the total distance between two grating couplers was 1cm.

A typical obtained experimental result is shown in **Fig.2.5.2a**.

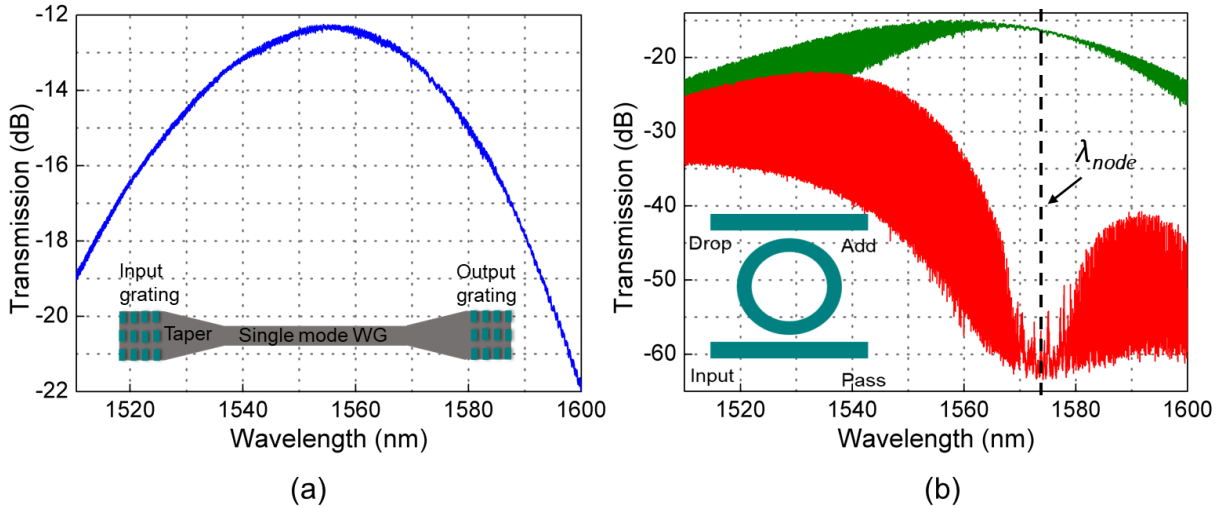


**Fig.2.5.2.** (a) The coupling efficiency as a function of a wavelength for nominal grating coupler designs and (b) Typical transmission spectral of a spiral RR (coupling gap  $d = 400$  nm, coupling length  $LC = 7 \mu\text{m}$ ).

The observed bell shape in **Fig.2.5.2a** is the signature of the grating spectral response. The measured 1 dB bandwidth is approximately 30 nm. Note that the target FSR of RR in this work is around hundred picometers, a small range variation around 1 nm wavelength is enough for this work, meaning that the bell shape grating spectral response does not raise any issue in the work carried out hereafter. The maximum fiber to fiber measured transmission level was estimated to -12.5 dB at 1.55  $\mu\text{m}$  wavelength for TM propagation. Due to the long length waveguide used to connect two grating couplers, the waveguide loss could not be neglected in the calculation of the single grating coupler losses. Coupling loss for one coupler was finally estimated as around 23 %. Although that this value is enough for our experiment, by optimizing the design, this coupling efficiency still could be improved.

A typical transmission of the add-drop RR is shown in **Fig.2.5.2b**. We see that at specific wavelength  $\lambda_{node}$ , i.e. at 1.573  $\mu\text{m}$ , no resonance mode is constructed inside the spiral RR. This is because at this wavelength, intensity input light is passing through access waveguide in the coupling region without being transferred into the ring. This behavior was explained in <sup>198,213,214</sup> and can be seen as a consequence of the impact of coupling length  $L_C$  (in related with coupling gap  $d$ ) into the fraction of power coupled in the input waveguide. In case when the coupling length  $L_C$  is equal to an even multiple of beating length  $L_b$ , based on **Eq. (2.2.12a)**  $k$  vanishes, hence, physically light does not see the ring at all. In other situations, when the coupling length  $L_C$  is equal to an odd multiple of beating length  $L_b$ , then based on **Eq. (2.2.12b)**,  $r$  equals 0. In this case, light goes into the ring in the first pass and out in the output port, there is no beam splitting and no possible destructive interference or resonance. To summarize, when the chosen coupling length  $L_C$  is equal to multiple of beating length  $L_b$  at specific wavelength  $\lambda_{node}$ , no resonance peak is constructed at  $\lambda_{node}$ . As the beating length  $L_b$  also is a function of the coupling gap  $d$  (see **2.2.2.4**), for fixed coupling length  $L_C$ , the specific value of  $\lambda_{node}$  corresponding to the spectrum node of the drop port optical transmission can be made varied as a function of  $d$ .

To calculate the waveguide losses, we used the method introduced by Shijun Xiao in <sup>215</sup>, which allows to quantify losses in resonators and bends without uncertain contributions from fiber coupling in/out or waveguide cleaved facets.

**Table 2.5.1.** Losses parameters of our RR.

$L_{SRR}$ (cm)	$\lambda_0$ (nm)	FSR (nm)	$L_c/d$ ( $\mu\text{m}$ )	$-10\log_{10}(\gamma_t)$ (dB)	$\delta\lambda_d$ (nm)	$k_p^2$	Round trip losses (dB/round trip)	Intrinsic losses (dB/cm)	Loaded $Q$ ( $\times 10^5$ )	Intrinsic $Q_i$ ( $\times 10^5$ )
0.57	1550	0.134	10.8/0.4	3.5	0.0089	0.27	1.37	2.4	<b>1.72</b>	<b>2.7</b>

By using the transmission spectra at both the through and drop RR ports, we deduced the minimum transmission of the through port ( $\gamma_t$ ) and the  $-3$  dB bandwidth ( $\delta\lambda_d$ ) of the drop-port at the resonance wavelength  $\lambda_0$ . The fraction of optical power

### 2.5. Optical characterization of spiral ring resonators

losses (such as bending, absorption and surface scattering due to roughness losses) per round-trip in the micro-resonator  $k_p^2$  was determined as  $k_p^2 = 2\pi \times \delta\lambda_d \sqrt{\lambda_t} / FSR$ , and the total propagation losses were calculated as  $-10\log_{10}(1-k_p^2)$  dB/round-trip. After that, the intrinsic quality factor was obtained as  $Q_i = (2\pi\lambda_o) / (FSR \times \kappa_p^2)$ . The obtained parameter values are summarized in **Table 2.5.1**.

The zoom-in in the transmission spectrum illustrated in **Fig.2.5.2b** is showed in **Fig.2.5.3**.

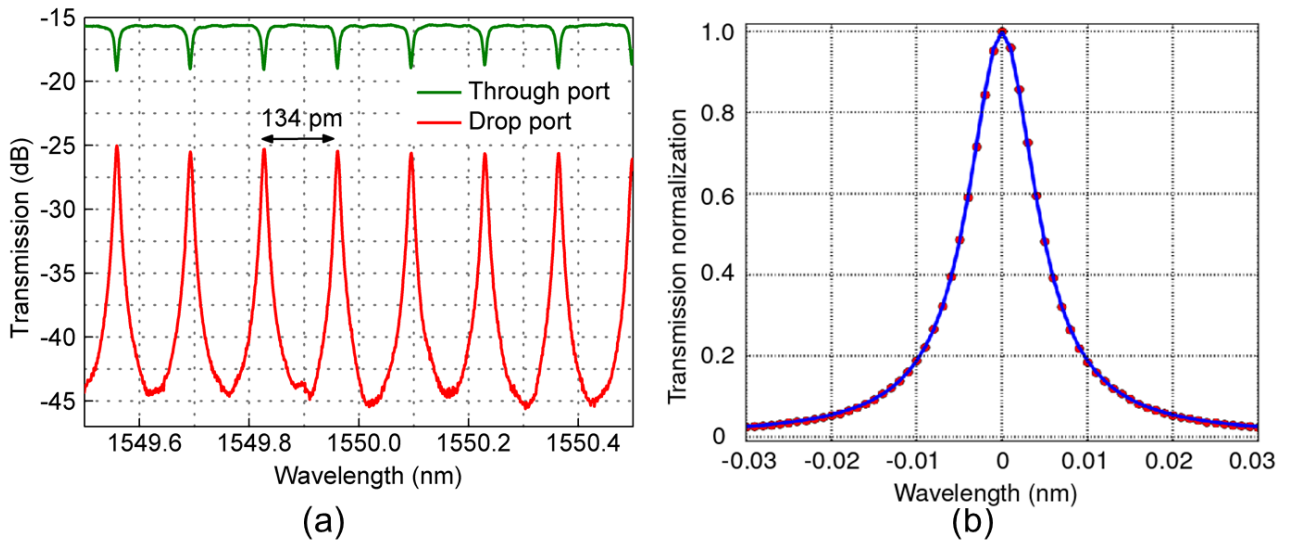


**Fig.2.5.3.** (a) The zoom-in in the optical transmission and (b) the Lorentzian fitting for the resonance peak (coupling gap  $d = 400$  nm, coupling length  $L_c = 7$   $\mu\text{m}$ ).

The observed FSR from all the tested devices were found at around  $FSR_{freq} = 16$  GHz, typically ranging from 14GHz to 16GHz. We used Lorentzian fitting to calculate the quality factors of RR (as can be seen in **Fig.2.5.3b**). Measured extinction ratio and quality factors, obtained from Lorentzian fits, are shown in **Fig.2.5.4** for a 400 nm coupling gap. It is seen that by changing the coupling length, a micro-ring drops port extinction ratio varying from 7 dB to 20 dB was monitored as well as **loaded quality factor  $Q$  ranging from  $3.3 \times 10^4$  to  $1.72 \times 10^5$** . The highest extinction ratio and also the highest quality factors were obtained for the spiral ring with  $L_c$  and  $d$  equal to 7  $\mu\text{m}$  and 0.4  $\mu\text{m}$ , respectively.

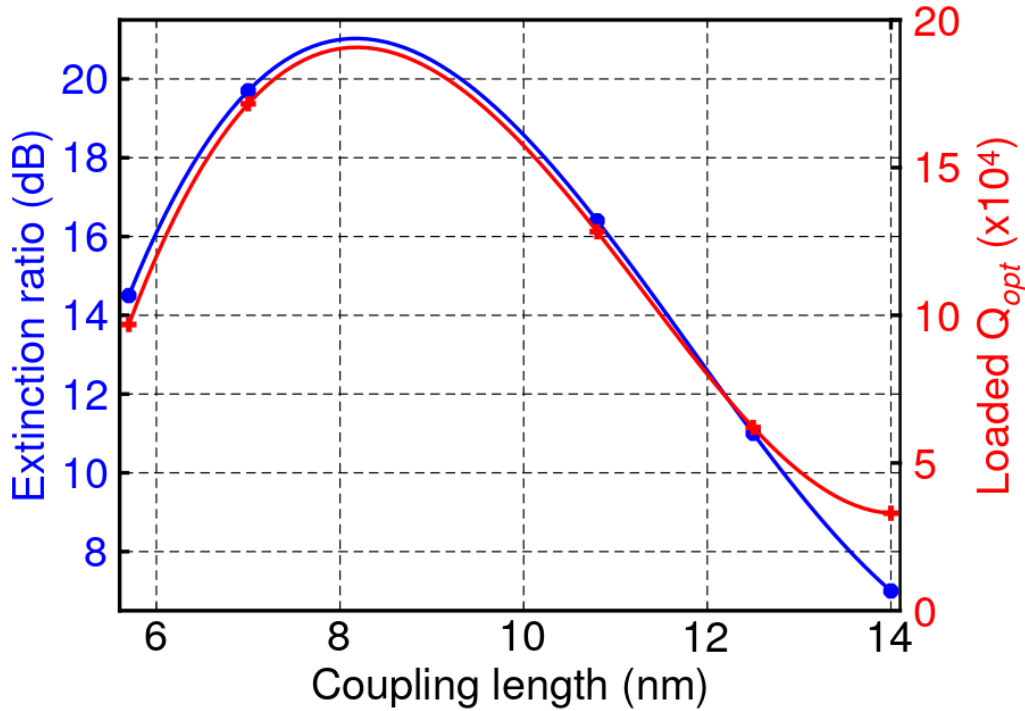


**Fig.2.5.4.** Variation of the micro-ring drop port extinction ratio and loaded quality factor  $Q$  depending on the coupling length (here for a coupling gap  $d = 400$  nm) at 1550 nm wavelength (marker: experimental results and line curve: fitting curve).

To summarize, by optimizing the combination of variation of  $L_c/d$ , we have been able to reach the target optical quality factor of at least  $10^5$  (see 2.2.2.c) with a ring resonator FSR around 16GHz, thus favorably preparing the use of integrated Si micro-resonators in the opto-microwave loop of the opto-electronic oscillators studied in this manuscript. Note that in order to increase the resonator  $Q$ , a larger width strip waveguide at 550 nm was also fabricated by using the same methods. By doing so, we observed  $Q_{opt}$  of  $3.1 \times 10^5$  at 1550 nm wavelength.

## 2.6. Conclusion

To summarize the works presented in this chapter, **photronics integration circuits (PIC) are discussed here**. We first briefly introduce the three main key devices for the realization of PICs and particularly of integrated OEOs, including on-Si lasers, modulators, and photodetectors, briefly summarizing their properties and describing the current state of the art related to their integration in Si photonics. An interesting domain application using silicon micro-RR device as bulk index sensor detection is discussed.

## 2.6. Conclusion

The limitation of classical resonant optical integrated sensors and the way to solve this problem, i.e. by converting optical signal to the microwave domain is explained, which then leads to a **particular focus on the thesis field, namely the integration of a silicon ring resonator into the loop of an optoelectronic oscillator for the generation of microwave signals and its application to bulk index sensing.**

In this chapter, we have covered the principle, the design, the fabrication and the characterization of integrated ring resonators. First, we have started with a quick overview of RR. After that, by optimizing the design and fabrication processes, we have obtained the integrated ring resonators with properties satisfying the targeted required of an FSR of around  $\sim 15$  GHz with an optical quality factor  $Q_{opt}$  above  $10^5$ . Two sets of spiral ring resonators with different waveguide widths of 365 nm and 550 nm were fabricated and characterized. The highest loaded optical quality factor obtained have been  $1.72 \times 10^5$  and  $3.1 \times 10^5$  at 1550 nm wavelength for 365 nm and 550 nm waveguide widths, respectively.

The integration of these ring micro-resonators into the loop of optoelectronic oscillators will be presented in the next chapter.

# 3

## Investigation of OEO Configurations Including Silicon Ring Resonators

This chapter aims to the integration of silicon ring resonators into OEO closed loop systems. We will describe here two different configurations of the OEO loop, comprising a laser source, an intensity modulator, a photodetector, an add-drop silicon ring resonator, optical and RF amplifiers and a RF coupler for closing the loop. Three main studies concerning the open loop, closed loop configuration, and application for refractive index sensing measurement will be presented and discussed in this chapter.

Following the results discussed in **Chapter 2**, we will first investigate the integration of a millimeter-long spiral SOI ring resonator into the OEO loop. The insertion of a millimeter-long silicon ring resonator into an OEO loop is a possible and interesting path for the direct synthesis of microwave signals. However, this approach faces a difficult problem, mainly for controlling low propagation losses in long perimeter length resonators corresponding to the targeted oscillation frequency. For that reason, in the second part of this chapter, we will propose a new OEO configuration which allows to be released from the opto-geometric constraints of requiring a very long ring resonators, the RF oscillation frequency being no longer controlled by the  $FSR_\lambda$  of the ring. Moreover, a wideband tunable oscillation signal, without any degradation in the signal quality for an increasing oscillation frequency, is observed based on this approach. The details of the proposed OEO configuration will be discussed in the second part of this chapter.

## 3.1. Direct insertion of a millimeter -long silicon ring resonator into an optoelectronic oscillator loop

As it has been presented in **chapter 2**, a millimeter length silicon RRs with  $FSR_v$  in the range of GHz and an optical quality factor higher than  $10^5$  ( $1.72 \times 10^5$  and  $3.1 \times 10^5$  at 1550 nm wavelength for 365 nm and 550 nm waveguide widths, respectively) have been successfully demonstrated. Since the required conditions for the integration of a silicon RR have been achieved, the insertion of this device into the opto-RF loop of OEOs can be performed.

### 3.1.1. Study of the realized microwave photonic filter

In a standard approach to closed looped systems, the study of the open loop provides valuable information about its closed loop behavior. Our approach was, therefore, to start with a study of the opto-microwave quadrupole obtained by opening the OEO loop between the output of the RF coupler and the input of the RF modulator. Because of the optical ring-resonator acting as a filter, this quadrupole behaves as a microwave bandpass filter and can be considered as a photonic microwave filter (MPF). And as a quadrupole it can be characterized by a vector network analyzer (VNA).

The experimental setup, which is shown in **Fig. 3.1.1**, is based on the final structure of the final OEO setup, as shown in **Fig. 3.1.3**. The VNA is placed in between the RF coupler and the electro-optical modulator, so the obtained  $S_{21}$  parameter of the RF quadrupole includes the contribution of the loop optical part.

The experimental setup made use of a continuous wave (CW) tunable laser TUNIC-T100S provided by Yenista Optics Company, for which an output power of 4 dBm was set for the experiment. The modulator was a Mach-Zehnder intensity modulator (IM), MXAN-LN20 from Photline Company. It is made of Lithium-Niobate and presents an RF bandwidth of 20 GHz and optical insertion losses of 2.7 dB at 1.55  $\mu\text{m}$  wavelength. The

modulator DC half-wave voltage was set at  $V = 3.55$  V. The photodetector (PD) was a XPDV2140R from U2T company with a cut-off frequency around 45 GHz and a responsivity of 0.6 A/W at 1.55 $\mu$ m wavelength. An optical EDFA pre-amplifier with output power at 16 dBm was also added at the output of the drop port of the silicon RR to boost the loop gain and reach the needed gain threshold condition for the generation of oscillations. An additional amplification section was made in the RF domain (see “G” in **Fig.3.1.1**), which included a set of 3 amplifiers, the ABL1800-33-3020 provided by Wenteq microwave Corp. with a total maximum gain of 60 dB. In the performed open loop characterizations, a 10 dB RF coupler, C117-10 from Narda ATM was used. The main coupled output was used for the oscillator loop and the attenuated output being used for spectrum analyzer monitoring. In this experiment, the coupled output was connected to the Port 2 of the network analyzer (VNA HP-8510). For any of the next described experimental characterizations, the best optical RR configuration was chosen, i.e. mainly speaking with the largest optical quality factor  $Q_{opt}$ .

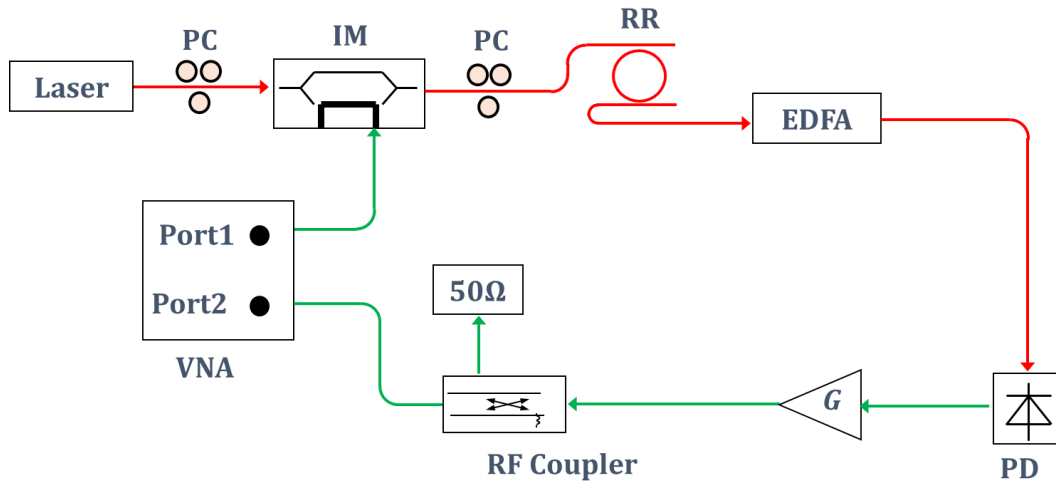


**Fig. 3.1.1.** Schematic of the studied configuration to characterize the open loop microwave response of the OEO, i.e. to study the realized equivalent microwave bandpass filter MPF. PC: Polarization controller, IM: Intensity modulator, RR: Ring resonator, EDFA: Erbium-doped amplifier, PD: Photo-detector, G: RF amplifier, VNA: Vector network analyzer.

In terms of chosen waveguide parameters, a spiral ring resonator including 550 nm width waveguides (coupling gap  $d = 400$  nm and coupling length  $L_c = 40$   $\mu$ m) was considered, leading to a Free Spectral Range of  $FSR_\lambda = 112$  pm or  $FSR_\nu \sim 14$  GHz. For this device,  $Q_{opt} = 3.1 \times 10^5$  was obtained at  $\lambda = 1.55$   $\mu$ m but simultaneously with high

### 3.1. Direct insertion of a millimeter -long silicon ring resonator into an optoelectronic oscillator loop

fiber to fiber insertion loss of 38 dB. Shifting the operating wavelength at  $\lambda = 1.54 \mu\text{m}$  was responsible for a moderate drop of  $Q_{opt}$  down to  $2.2 \times 10^5$  with yet a much lower fiber to fiber insertion loss level of around 25 dB. Experiments were thus carried out at  $1.54 \mu\text{m}$  wavelength.

In the experimental setup, the sample was placed on a Peltier temperature controller to prevent the resonator from being affected by temperature variation and the laboratory room environment was kept at a constant temperature. The response of MPF was given by the transmission coefficient  $S_{21}$  measured by the VNA. To do so, a scanning RF signal came out from port 1 of the VNA, feeding the IM and linearly modulating the laser carrier. The laser carrier was first locked onto the center of one of the RR resonance modes while RF output was collected on port 2 of the VNA. During the experiment, the VNA was set with a span from 2 GHz to 19 GHz, an output power of 10 dBm and with 801 measurement points, which was the maximum value for the available VNA, a HP8510.

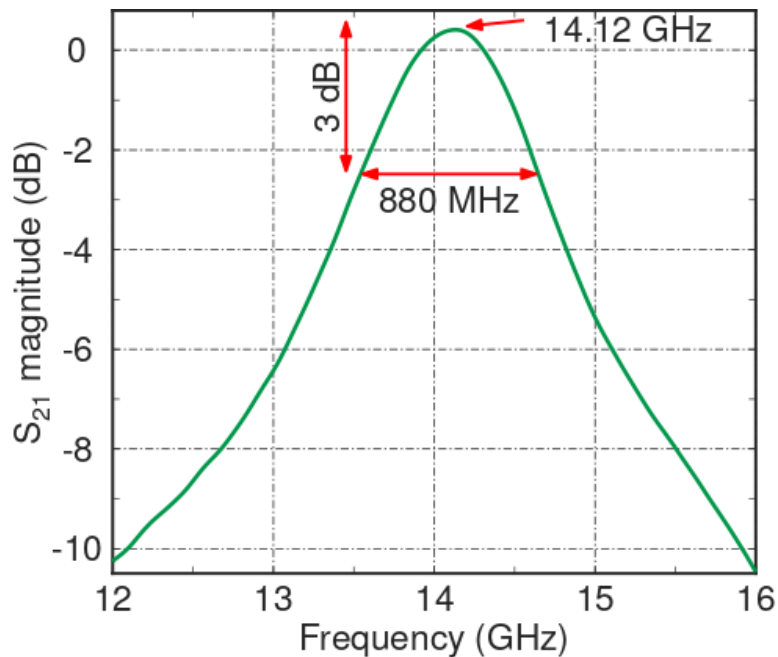


**Fig.3.1.2.**  $S_{21}$  transmission coefficient's magnitude deduced from the integration of Silicon spiral RR.

From the collected data, we managed to calculate both the open loop gain and phase. However, due to large scan bandwidth (2-19 GHz) and the limited number of testing points (801), the sweep step was 12.5 MHz, i.e. not enough to precisely

determine the phase change of the  $S_{21}$  transmission coefficient. **Fig. 3.1.2** shows the  $S_{21}$  coefficient's magnitude deduced from the experimental data.

As it can be seen in **Fig.3.1.2**, the frequency response of the MPF was observed around 14.12 GHz, in good agreement with the optical  $FSR_v$  of the resonator. Moreover, the  $S_{21}$  maximum transmission peak was obtained at 0.5 dB, meaning that its overall gain was larger than the loss, thus satisfying the gain condition of the loop.

From **Fig. 3.1.2**, we deduced a quality factor of the equivalent MPF microwave filter,  $Q_{RF} \approx 16$ . Since the optical quality factor of the RR is  $2.2 \times 10^5$  at 1540 nm wavelength (194 THz), a direct application of the frequency scaling ratio between the optical and RF quality factors, namely  $Q_{RF} = (f_{RF}/f_{opt}) \times Q_{opt}$  (**Eq. (2.2.7)** in **chapter 2**) leads to  $Q_{RF} \approx 16$ . The good consistency, resulting from an indirect calculation of  $Q_{RF}$  from the optical quality factor and its direct measurement in the open loop, thus provided a validation of the experimental measurements.

To conclude this part, the open loop configuration of OEO based on silicon spiral RR was studied, showing a sufficient gain higher than the loss. The study of OEO based on such silicon spiral RR in closed loop configurations is described in the next step.

### **3.1.2. Opto-electronic oscillator based on a millimeter-long silicon ring resonator**

In the study of the closed OEO configuration, the VNA was removed and we came back to the standard OEO full closed-loop configuration. The related experimental setup schematic is displayed in **Fig.3.1.3**. Every condition was maintained as in the open loop characterization step. An Agilent PSA-E4446A electrical spectrum analyzer (ESA) was used to analyze the output RF signals.

3.1. Direct insertion of a millimeter -long silicon ring resonator into an optoelectronic oscillator loop

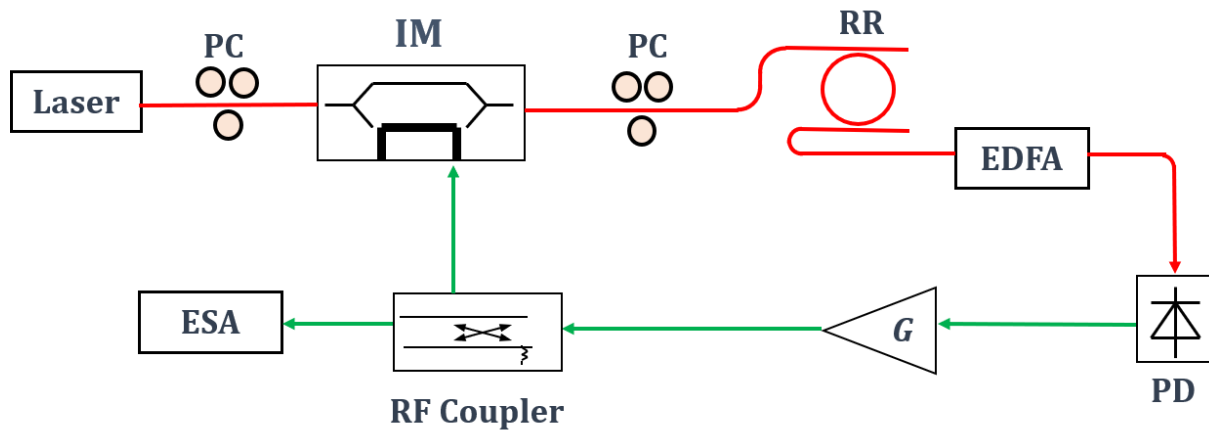


Fig. 3.1.3. Experimental setup schematic of the OEO based on a silicon spiral RR.

### 3.1.2a. Oscillation signal properties.

A typical generated signal is shown in Fig.3.1.4, with a span of 12 MHz and a frequency resolution bandwidth of 2.7 kHz. An oscillation frequency of 14.1198 GHz was reported in the performed single shot acquisition mode of the RF spectrum analyzer, thus in good agreement with the open loop results presented in section 3.1.1.

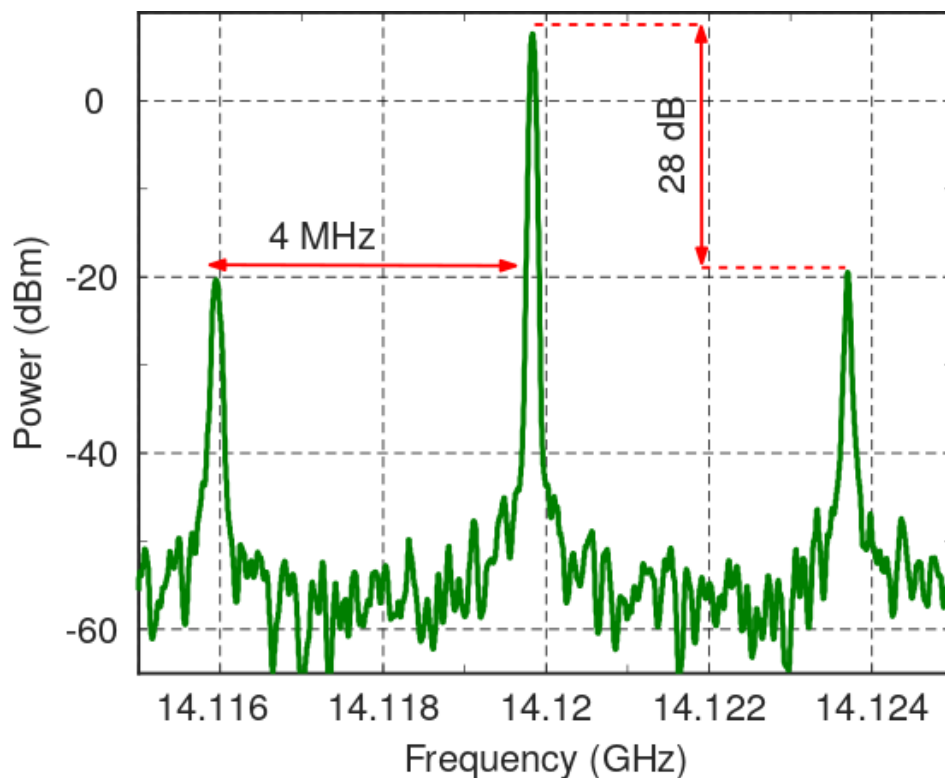


Fig.3.1.4. Spectrum of the signal generated by the OEO based on spiral Silicon RR.

### 3.1.2. Opto-electronic oscillator based on a millimeter-long silicon ring resonator

Simultaneously, we also observe the presence of two other peaks with a mode spacing of 4 MHz in the collected electrical spectrum and a mode suppression of around 28 dB was obtained for the next dominant mode. We questioned the origin of these peaks and it appeared to us that, in fact the OEO, as it was built, does not correspond exactly to a complete integration scheme. At this stage of the progress, the RR was inserted into the loop, but different remaining sections of optical fiber were used to connect the various elements of the optical part of the system (3 m and 1 m fiber sections in the modulator and photodetector, respectively). In addition, an EDFA was present in the optical path and optical fiber inside the PC and fiber used to connect each building block. Therefore, a total fiber length remains inside the system of approximately a few tens of meters.

Under the closed-loop condition, light propagates through the whole loop but the presence of an optical fiber of a few tens of meters, in addition to the ring resonator, actually changes somewhat the nature of the loop. In the presence of a fiber, a pure delay is introduced, and the resonator's filter transfer function is therefore combined with the delay found in a conventional optical fiber OEO. Globally speaking, the oscillator, as a whole, cannot be classified entirely neither as a filtering oscillator nor as a pure delay oscillator but presents a kind of hybrid character. Moreover, the conventional OEO has a fundamentally multi-mode behavior, with mode spacing described by **Eq. 1.2.7** (see **chapter 1**). As a result, where one would expect a single-frequency oscillation, additional frequency lines are present. The consistency of this hypothesis could be tested by evaluating the length of optical fiber that is deduced from the relationship  $L_{Fiber} = c/(n.FSR_{osc})$ , where  $c$  is the velocity of light in vacuum and  $n$  is effective refractive index of optical fiber. Doing so leads to an optical fiber length of around 52 m, i.e. in close consistency with the fiber length developed in the setup as illustrated above. This multimode frequency behavior is not disturbing as it is well identified and would be removed in case of a fully integrated version of an OEO.

We checked the properties of the loop by opening and closing it a large number of times in order to check the repeatability of the birth of RF oscillations. These verification tests were successful. In addition, all the acquired spectra gave rise to oscillation lines close to 14.12 GHz, but without strictly overlapping each other. A fluctuation of the

### 3.1. Direct insertion of a millimeter -long silicon ring resonator into an optoelectronic oscillator loop

central oscillation line of a few tens of kHz was indeed observed. In order to evaluate the fluctuations of the RF oscillation spectral line, we measured the OEO spectrum by keeping the analyzer trace in Max-Hold mode to record the accumulation of the moving stage of the oscillation signals. The result is shown in **Fig.3.1.5a** for a measuring time of around a few minutes. Under these conditions, a flat signal spectrum with a bandwidth of 34.4 kHz was observed at the center frequency around 14.1198 GHz. This curve can actually be considered as the envelope of contributions such as those in **Fig.3.1.4**, made at different times between the RF center oscillation frequency of which being shifted by a few kHz. These shapes come from the analyzer resolution bandwidth and from both amplitude and phase noises. Different noise sources mainly come from the laser frequency noise and the RF amplifiers noise. In particular, the laser frequency noise can be converted into amplitude noise inside the resonator and constitutes a source of noise for the complete OEO loop <sup>216-219</sup>. Indeed, the oscillation signal is created with the frequency equal to the distance between the carrier, which is locked onto one resonance mode, and the two modulation sidebands matching with an adjacent resonance of this mode. If the laser wavelength suffers small fluctuations, the distance between the carrier and the modulation sideband can slightly change, which consequently affects the variations of the generated RF frequency. In a previous work <sup>94</sup>, authors have shown fluctuations in the oscillation frequency of approximately 1 MHz.

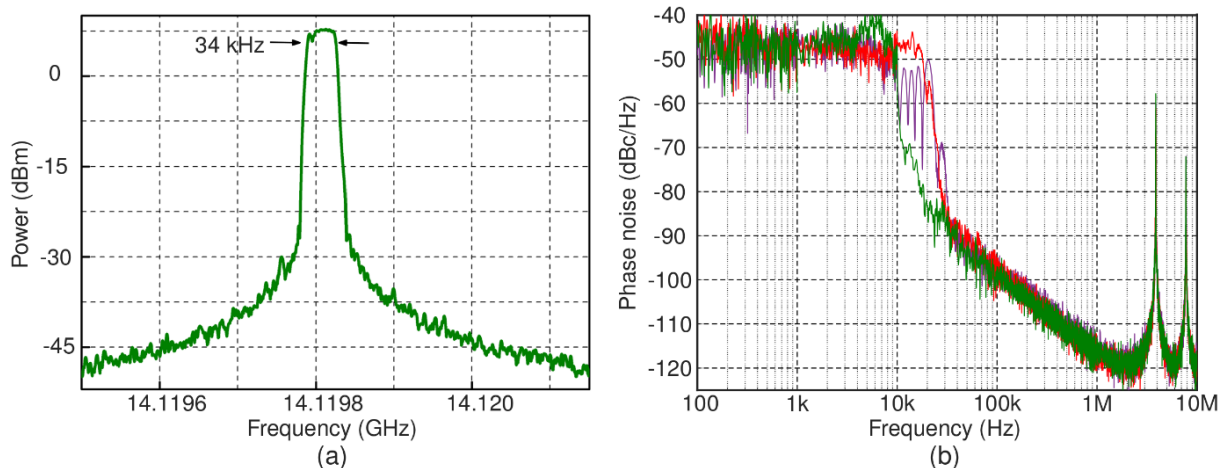


**Fig. 3.1.5.** (a) RF spectrum of the signal generated by the OEO acquired in the Max-Hold mode of the RF spectral analyser. (b) Phase noise measurement of the generated oscillation frequency collected several times.

### 3.1.2. Opto-electronic oscillator based on a millimeter-long silicon ring resonator

Finally, the phase noise measurement was performed by using the automatic setup of the E4446A RF analyzer, working in the "Phase Noise" mode to evaluate the stability and the quality of the generated signal. The analyzer phase noise floor of the analyzer was -145 dBm. The experiment was repeated several times and the results were overlaid. The related results are shown in **Fig.3.1.5b** for several detected signals.

In this operating mode, the RF analyzer performs a real-time calculation of the phase noise through the autocorrelation of the phase to get the spectral power density at an offset frequency away from carrier referenced (oscillation frequency) <sup>18</sup>. For the complete process, the oscillating frequency has been observed at the beginning of this process. The measurement process being conducted for one range of offset frequency after another, it takes some time during which the oscillation frequency can fluctuate as it can be seen in **Fig.3.1.5a**, thus flawing the phase measurement. One example can be seen in **Fig.3.1.5b**. The curves are rather flat, low and not really reproducible with a level of  $\sim -50$  dBc/Hz at offset frequency lower than 35 kHz from the carrier, in agreement with the Max-Hold mode accumulation of RF spectra shown in **Fig.3.1.5a**. This curve is related to the fluctuations of the oscillation signal, as indicated in the previous observation but also with the measurement method.

Beyond  $\sim 35$  kHz offset frequency from the RF carrier, the fluctuations of the spectral line are less important, and the signal becomes more stable which is indicated by a good overlap between all the generated signals. The phase noise level dramatically decreases to recover a slope of -20 dB/decade or the  $1/f^2$  behavior resulting from white noise in the oscillator as introduced by Leeson in <sup>16</sup>, and this part of the curve is reproducible. Accordingly, we obtained a phase noise of -100 dBc/Hz at 100 kHz offset frequency from the carrier. In a recent study dedicated to the integration of OEO in Si photonics <sup>96</sup>, a rather similar plateau phase noise behavior was observed at  $-80$  dBc/Hz between 1 kHz and 100 kHz offset from the carrier while an oscillation frequency around 7 GHz was reported. An improvement in noise behavior near the carrier would require specific treatment of all elements of the looped system chain. In addition, we obtained other peaks at 4 MHz and 8MHz in the phase noise spectrum, which correspond to the distance between the oscillation signal and its adjacent 1<sup>st</sup> and 2<sup>nd</sup> modes (see **Fig.3.1.4**).

### 3.1. Direct insertion of a millimeter -long silicon ring resonator into an optoelectronic oscillator loop

The noise performance of the generated signal may be further lowered through several improvements:

- 1) The low quality ( $Q_{RF}$ ) of the equivalent microwave photonic filter MPF which is directly linked with the optical quality factor  $Q_{opt}$  of the resonator. Previous research in fiber ring resonator based OEO has indicated that the OEO noise is inversely proportional to the optical quality factor  $Q_{opt}$  of the resonator and can be expressed as <sup>5</sup>:

$$L(f_m) = 20 \cdot \log \frac{f_{opt}}{2\sqrt{2}Q_{opt} \cdot f_m} + 10 \log (NCR) \quad (3.1.1)$$

where  $f_m$  is the noise modulation frequency (offset frequency) and  $NCR$  is the optical noise to carrier ratio. One can clearly see that increasing  $Q_{opt}$  could contribute to make the loop noise decrease.

- 2) The fluctuations of the supply current applied to the EDFA <sup>220</sup>. The pump current variation can lead to a change of the overall loop gain, which can lead to power fluctuations and increase the phase noise of the generated microwave signal.
- 3) RF noise sources are inherently present in the loop due to the presence of the components inside the loop such as the photodetector and the RF amplifiers. Previous investigations have thoroughly estimated the contributions of these elements <sup>221</sup> and a lot of optimization work would have to be done in this spirit and with these tools in order to fully integrate an ultra-low phase noise (e.g.,  $\ll -120$  dBc/Hz at 1MHz) OEO on a silicon chip.

#### 3.1.2b. Impact of the light source on the oscillation signal quality.

As mentioned above, the stability of the laser source is one of the important factors responsible for the performances of the generated signal by the whole opto-RF loop. Our study was therefore further extended here in this direction.

Following the previously carried out experiments achieved with the tunable laser TUNIC-T100S, new tests were carried out with a telecom qualified distributed feedback diode (DFB) laser which was known to provide better stability source in comparison

### 3.1.2. Opto-electronic oscillator based on a millimeter-long silicon ring resonator

with a commercial tunable laser. The available laser was the DFB-1905 LMI (from Alcatel), operated at around  $1.54 \mu\text{m}$  wavelength. Two feeding currents were applied one to the laser diode and the other one to a Peltier cooler embedded inside the laser module, for a fine tuning of the source wavelength. By doing so, matching the laser wavelength with one of the resonance peaks of the RR was easily achieved. Once the laser wavelength was well stabilized on the center of the resonance peak, the applied currents to the laser and Peltier module were kept unchanged. By closing the loop, oscillations were generated as previously, and phase noise characteristics were monitored. **Fig.3.1.6** represents the phase noise spectral measurement of the OEO with the two different laser light sources, the tunable (red color) and DFB (blue color) ones, respectively.

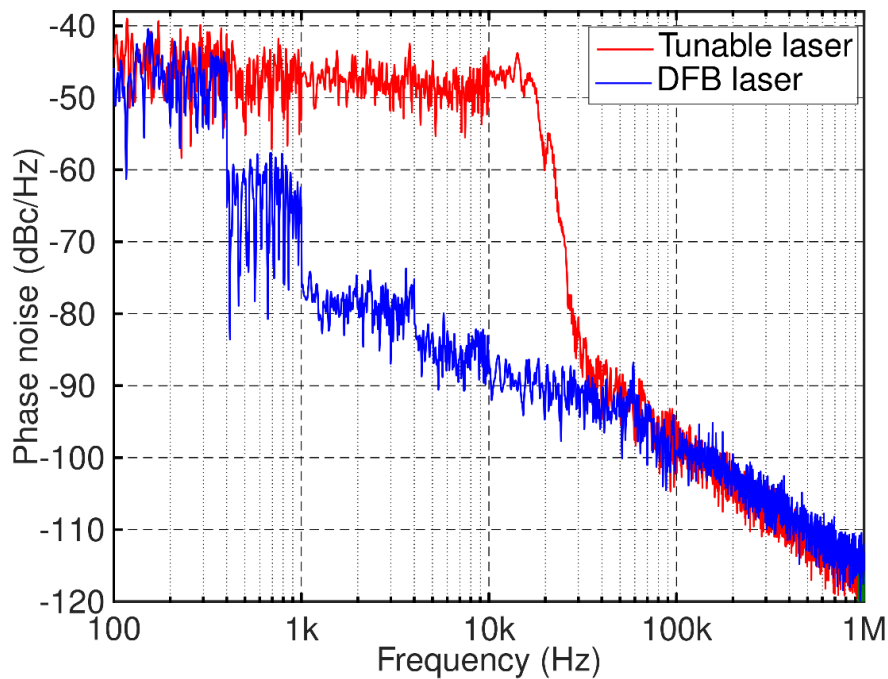


**Fig.3.1.6.** Phase noise spectral of OEO based on silicon RR for the two different lasers.

It is obvious to see from **Fig.3.1.6** that in both cases, the phase noise curves follow a  $1/f^2$  slope behavior for large offset frequency from the carrier. However, the use of a more efficient laser leads to a very significant improvement in noise in the 1-~40 kHz spectral range relative to the carrier. i.e. in case of using the DFB laser. The observed flat region in each phase noise spectrum (which as described above, is related with the fluctuation of the created signal) is moved down to 1 kHz. This value is much smaller

### 3.1. Direct insertion of a millimeter -long silicon ring resonator into an optoelectronic oscillator loop

than what has been obtained with the tunable laser. Significantly, 40 dB of noise level reduction at 1 kHz offset frequency was observed when the DFB laser was used, thus resulting in a slope of  $1/f$  of noise behavior for the offset frequency between 1 and 100 kHz <sup>16</sup>. This result is a confirmation that the laser plays an important role in the noise performances of the realized OEOs. The phase condition to obtain the oscillations is based on the phase shift in the microwave domain, which is depending on the phase shift created in the optical domain by the resonator, a noteworthy highly dispersive element. Given the role of dispersion in enhancing laser frequency noise, the use of a very frequency-stable laser is probably a prerequisite for further improvement in the quality of the generated signal in the future.

To conclude this part, we have investigated the insertion of silicon spiral ring resonators into the opto-RF loop of OEOs. The gathered experimental results report a good agreement between the optical  $FSR_{\lambda}$  of ring resonators, open loop gain measurements and closed-loop oscillation frequencies of around 14 GHz.

Overall, the performed implementation demonstrates that the direct integration of a mm-long spiral shape silicon ring resonator is a reliable approach for the realization of integrated on-chip OEOs and thus can open up a new range of applications of this loop. The experimental studies carried out have highlighted the important influence of all noise sources in the loop for getting low noise signals. The roles of the laser and amplifiers (optical and RF) are probably the most important ones. In the current state of the components that have been assembled for the oscillation of the loop, and after inserting a millimeter ring resonator into it, a phase noise of the order of - 100 dBc/Hz has been measured at 100 kHz of the carrier based on the quality factor resonators of the order of  $2 \cdot 10^5$ . At the same time, a very significant improvement in noise in the 1 to 40 kHz offset band relative to the carrier was achieved by using a DFB telecom laser.

In terms of performance, the investigated route also gives room to another progress direction. The experimental results we report are based on ring resonator with a quality factor of about  $10^5$ . SOI ring resonators with higher quality factors of up to  $1.7 \times 10^6$  have already been demonstrated <sup>222</sup>. Such a quality factor would almost yield an eight-fold performance improvement compared to our realization, which would reduce the

### 3.1.3. Refractive index measurement based on mm-long Si RR integrated into an OEO loop

bandwidth of the equivalent microwave filter and lower the phase noise of the OEO. Moreover, the perspective of the full OEO system integration on a single chip could help to further scale down the loop phase noise properties.

In the next section, we present the application of the realized OEO loop for bulk index sensing, consistently with the thesis objectives presented in part 2.1.2 of chapter 2.

### 3.1.3. Refractive index measurement based on mm-long Si RR integrated into an OEO loop

The main objectives of this part have been presented in part 2.1.2 of chapter 2. To summarize quickly and starting now from a working optoelectronic oscillator RF loop well and truly oscillating, the challenge here is to evaluate how the generated RF frequency is sensitive to the refractive index of the layer present on top of the resonator.

Silicon RR with 350 nm strip waveguides were considered to provide a better sensitivity if compared with the 550 nm strip ones (see part 2.3.1). The optical characterization of the device has been discussed in part 2.5 of chapter 2, with  $FSR_{\lambda} = 134$  pm or  $FSR_{\nu} \sim 16$  GHz.

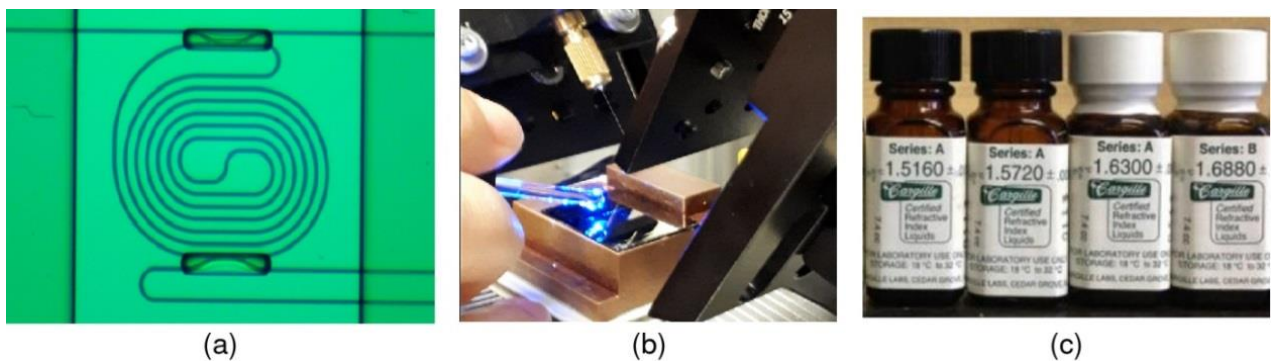


**Fig.3.1.7.** (a) Spiral RR with the opened window for sensing detection, (b) Capture picture showing the set of available refractive index liquids, and (c) List of used refractive index liquids.

### *3.1. Direct insertion of a millimeter -long silicon ring resonator into an optoelectronic oscillator loop*

In order to prepare the samples for sensing measurements centered on the silicon ring resonator of the OEO, the 2  $\mu\text{m}$  height PMMA top cladding layer was opened in order to create a window along the area of the spiral RRs. To do so, a *.gdsII* file containing area to expose was first prepared through a Python script interface. After that, this file was transferred to the Raith 150 system <sup>223</sup>, which consisted mainly of a scanning electron microscope (SEM) integrated with hardware for doing lithographic electron beam exposures. For the exposure step, the sample was first loaded into SEM, and here all operations such as focusing, adjusting and alignment were done. The working distance was set at 5.5 mm. The computer then run the Raith 150 software to start the exposure, with an exposure voltage set to 20 kV. The total exposure time was 36 minutes. After the lithography step, the development process was conducted by using a mixed solution composed of Isopropyl alcohol (IPA) + water in volume ratio at 3:1 for 6 minutes <sup>224</sup>. In the last step, the sample was cleaned by plasma O<sub>2</sub> to eliminate the remaining organic solution. The fabrication result is illustrated in **Fig. 3.7a**. In order to properly localize the liquid interaction of index/structure in a dedicated volume, the sensing window was fabricated by keeping two specific regions (the coupling ones) in an area of 170 x 40  $\mu\text{m}$  while removing all the covered cladding cover on the rest of the ring (as it can be seen in **Fig. 3.7a**).

To investigate the refractive index sensing of the OEO based on silicon RR, a list of refractive index liquids provided by Cargille Labs <sup>225</sup> matching the values of 1.516, 1.572, 1.63 and 1.688 were used (**Fig.3.1.7c**). Experimentally, a little amount of refractive index liquid was dropped on top of the sample to fulfil the opened window (**Fig.3.1.7b**). Two successive experiments were separated by a cleaning process step using isopropanol, then a new liquid was drop cast afterwards, the overall process was repeated several times.

In the particular studied configuration, the full RR was not fully covered by the liquid index since the coupling regions of 170  $\mu\text{m}$  length were still protected by the PMMA top layer (**Fig.3.1.7a**), this length being yet much smaller than the total 5.8 mm perimeter length of the whole structure. With this strategy, we sought to measure the frequency variations induced by the FSR variation of the ring due to surface index perturbation. Detecting this index variation from the RF frequency changes, we have

### 3.1.3. Refractive index measurement based on mm-long Si RR integrated into an OEO loop

been able to estimate the index sensing property of the loop based on the mm-long spiral RR.

Keeping the same condition as in the previous step, the oscillation signal was indeed observed for the closed OEO loop. After a new cleaning and liquid drop cast, the loop newly oscillated, and we could observe an RF frequency change. Unfortunately, quantitative measurements by this approach were spoiled by the mode hopping effect during the experiments. The occurring of the mode hopping comes from the fact that spurious oscillation peaks are presented under the oscillation condition of the loop (as explained in 3.1.2). The loop then may lock each time on a slightly different mode coming from fiber section. It was therefore not possible to attribute for sure the frequency shift to the effect of the new index.

This problem was circumvented by using another measurement technique based on the open loop configuration of the OEO. Indeed, open loop measurements being not affected by mode hopping, it was possible to retrieve index variations. This approach allowed somewhat to test the OEO loop in its final configuration after integration of all its elements and thus without any optical fiber section.

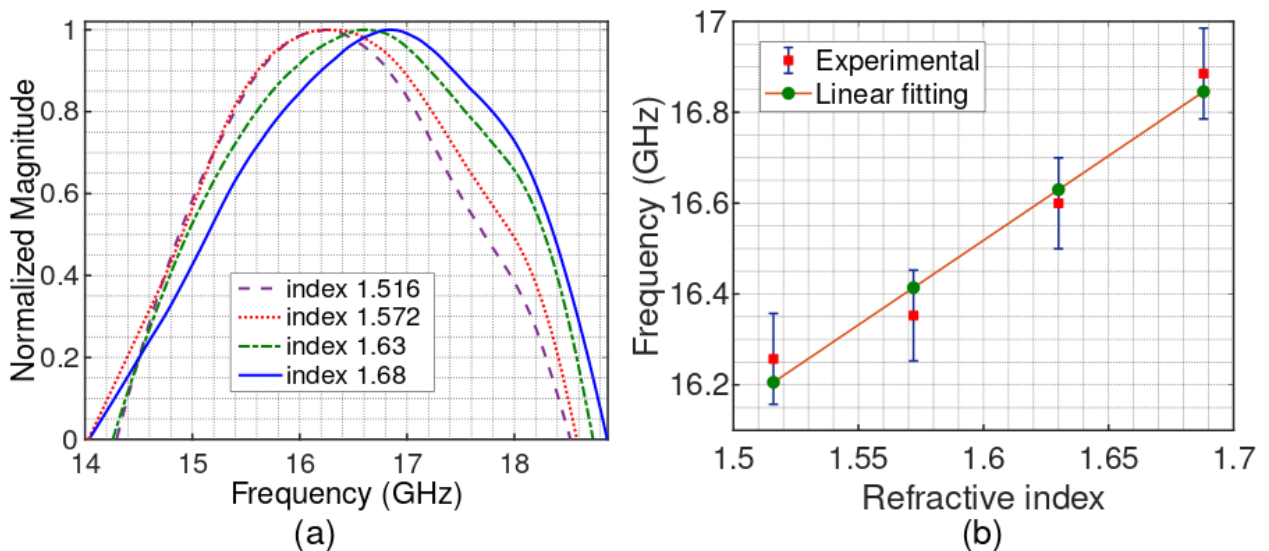


**Fig. 3.1.8.** (a) Plot of the normalization of  $S_{21}$  when differences cladding index values are used and (b)  $S_{21}$  center frequency changed as a function of the refractive index unit.

The experimental setup is the same as the one described in **Fig.3.1.1** of this chapter. It allowed us to export the  $S_{21}$  transmission coefficient of the open loop and to follow

### 3.1. Direct insertion of a millimeter -long silicon ring resonator into an optoelectronic oscillator loop

its evolution as a function of the cladding liquid index. This approach was therefore applied here by proceeding successively for the different index liquids indicated above.

**Fig.3.1.8a** reports the obtained  $S_{21}$  evolution as a function of the bulk top cladding refractive index, while **Fig.3.1.8b** reports the deduced change of the MPF frequency response peak as a function of the liquid refractive index. In the refractive index range explored (1.516-1.688), a quasi-linear evolution of the central frequency of the MPF filter was observed from 16.25 GHz to 16.88 GHz. Calculating the curve slope, a sensitivity  $S$  of around 3.72 GHz/RIU was obtained. This encouraging result shows the potential of the complete structure for index detection. As it was introduced in section **2.1.2** of **chapter 2**, the sensor limit of detection (LOD) is defined by the ratio between the sensor resolution  $R$  and the sensor sensitivity  $S$  ( $LOD = R/S$ ).  $R$  depends on the spectral resolution and system noise factor of the methodology for measuring the spectral shift in response to a sample. In the studied OEO, as illustrated in **3.1.2a** and **b**, the generated signal could be observed with a quite stable phase noise at around 40 kHz offset frequency from the carrier, meaning that it is possible to distinguish two different signals with 40 kHz difference in frequency or in other terms the measurement resolution  $R$  of the system can be estimated at 40 kHz. From these simple orders of magnitude, a minimum refractive index variation around  $LOD \approx 10^{-5}$  can be inferred.

To conclude, the OEO loop configuration studied in this section, i.e. including a millimeter-long ring resonator, proves to be an attractive approach for the bulk detection of index variation. But in case of other applications (for example radars, wireless communications, optical signal processing, electronic warfare system, and modern instrumentation), it could be also interesting to be able to tune the oscillation frequency [220,226](#). The approach developed in the following section essentially pursues this objective.

## 3.2. Wideband tunable microwave signal generation based on silicon photonic resonator

We propose here a new configuration of the OEO system that allows to create a wideband tunable oscillation signal without any degradation in the signal properties when the oscillation frequency increases. This chapter starts with the explanation of the working principle of the proposed approach. The tunability will be confirmed thereafter with the aim to develop sensing applications. We will then explore the proposed option through the study of refractive index variation detection.

### 3.2.1. Principle of operation

In the previous structure, the microwave signal was generated by the beating of the optical carrier and of a sideline of an intensity modulated optical signal, both being selected by the optical transfer function of an add-drop resonator. That is possible under the condition that the RR  $FSR$  must precisely match the frequency difference between the carrier and sideline frequencies ( $FSR_\nu$  in range of few ten of GHz or  $FSR_\lambda$  in range of hundreds of pm). In order to avoid the very low  $FSR_\lambda$  value required, another possible solution is to limit the use of the ring resonator to select only one lateral line of the signal from the intensity modulator. The optical carrier can, in fact, be brought directly to the input of the photodetector. By this way, the beating between the optical frequencies necessary for the synthesis of an RF signal can be created. The basic schematic and principle of operation of the proposed OEO are depicted in **Fig.3.2.1**.

In the proposed tunable OEO configuration, shown in **Fig.3.2.1**, the optical signal coming from the laser light source (frequency  $f_0$ ) is separated into two arms. One is connected directly to the photodetector (PD), while the other feeds an intensity modulator (IM) followed by a silicon ring resonator (RR) in an add-drop configuration. In this scheme, the input signal of the PD always comprises a part of the un-modulated laser light beam. At the initial stage, the modulator output signal grows, just seeded by white noise existing inside the loop. If one modulation output signal can go through the optical transfer function of the resonator at frequency  $f_R$ , this signal can then be

### 3.2. Wideband tunable microwave signal generation based on silicon photonic resonator

combined with the optical carrier ( $f_0$ ) at either its left or right sides to generate a beating signal at frequency  $f_b$  at the input of the PD. If the distance between the optical carrier ( $f_0$ ) and the signal at  $f_R$  falls within the working range of the loop, the generated beating signal can be converted as a RF frequency  $f_{RF}$  ( $f_{RF} = f_b = |f_0 - f_R|$ ) at the output of the PD. At the second round-trip of the loop, the generated RF signal is sent back to the modulator. At this stage, only one single sideband

modulation signal can match the RR resonance peak at frequency  $f_R$  (see **Fig.3.2.1b**). The RR now serves as an optical bandpass filter, selecting only one sideband lobe of the modulated signal. The signal goes to the PD at the second-round trip of the loop, creating again an RF signal with frequency  $f_{RF}$ . After this point, the loop oscillates with an oscillation frequency at  $f_{RF}$ .

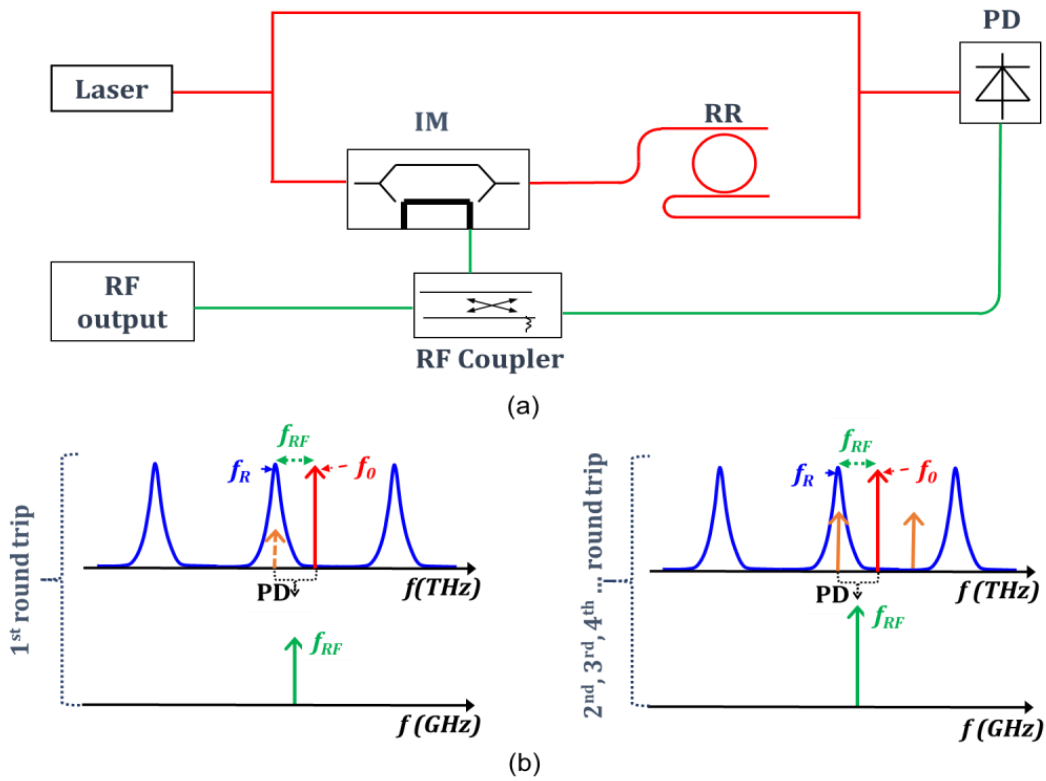


**Fig. 3.2.1.** (a) Basic schematic and (b) Principle of operation of the proposed tunable OEO. In (a), IM: Intensity modulator, RR: Ring resonator and PD: Photodetector. In (b), the red curve corresponds to the optical carrier (or laser source frequency); the orange curve illustrates the sideband lobes of the modulated signal, the blue curve indicates the optical transfer function of the RR and the green one represents the generated RF frequency  $f_{RF}$ .

The main idea behind this approach is to control the frequency of the microwave signal by the wavelength spacing between the laser source and the resonance of the resonator. Since this spacing can be changed either by sweeping the wavelength of the laser or by shifting the resonance peak of the RR, this approach yields a simple tunability mechanism. An important advantage of the proposed solution is also to be able to free itself from the opto-geometric constraints of making a very long ring resonator, the RF frequency no longer being controlled by the *FSR* of the ring. The rings used in this last approach are described in the following section.

### 3.2.2. Silicon ring resonator design and fabrication

In the studied OEO configuration, the oscillation frequency can be generated by positioning the laser wavelength at either left or right side of the resonance peak. If the distance between laser wavelength and these peaks are in the working range of the loop, it is possible to create two oscillation frequencies. This happens when the *FSR* of the RR is equal or smaller than twice the maximum working frequency of the loop (19 GHz in our case). To simplify the following experiment, the design of the RR has been made in order to allow only one oscillation signal to be generated under the working condition of the loop. To do so, the *FSR* of the resonator has been chosen with a value much higher than the maximum frequency supported by the loop.

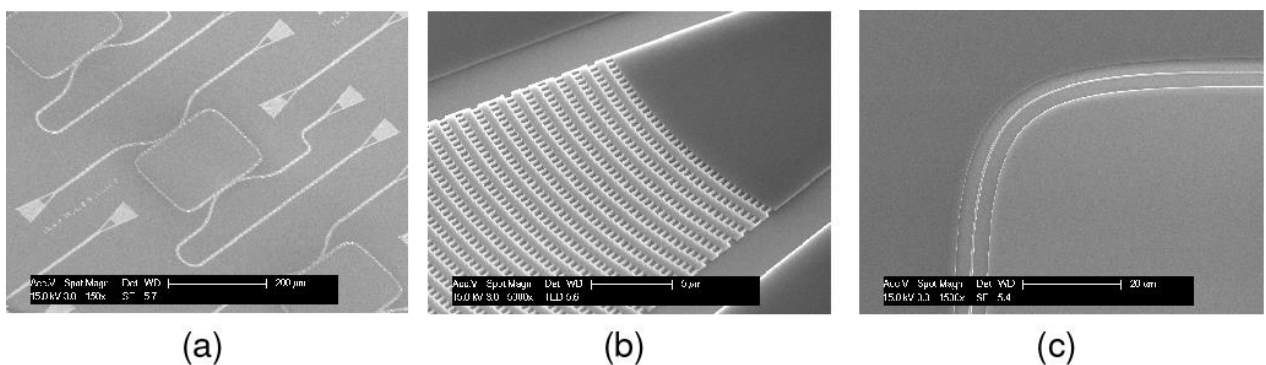


**Fig.3.2.2.** (a) Scanning electron microscope image of the fabricated silicon RR, (b) Grating coupler and (c) Bending curve.

The fabrication of the add-drop RR started with a 220 nm thick Si thin film on top of a 3 μm buried oxide layer. A 450 nm wide strip waveguides designed to operate in a

### 3.2. Wideband tunable microwave signal generation based on silicon photonic resonator

transverse-magnetic (TM) polarization at 1.54  $\mu\text{m}$  has been made for the purpose of sensing application. The resonator length  $L$  was chosen at 1 mm. Accordingly, the  $FSR_\lambda$  (defined by Eq. (2.2.4b)) was calculated at 77 GHz ( $n_g = 3.9$  at 1.54  $\mu\text{m}$  wavelength). In the RR design, an adiabatic bend was introduced (Fig.3.2.2c) in order to reduce the losses coming from the mode mismatch at the transition between the straight waveguide and the circular bend. The detail of the design construction of an adiabatic bend can be found in <sup>203</sup>. Light was injected and extracted again from the chip using a surface grating coupler. Fig.3.2.2b shows the detail of the used grating coupler, the design of which was made with some modifications in grating parameters (duty cycle, grating width and grating period) compared with the previous gratings used in chapter 2 and in part 3.1 of this chapter in order to increase the transmission level and also to reduce the grating section footprint.

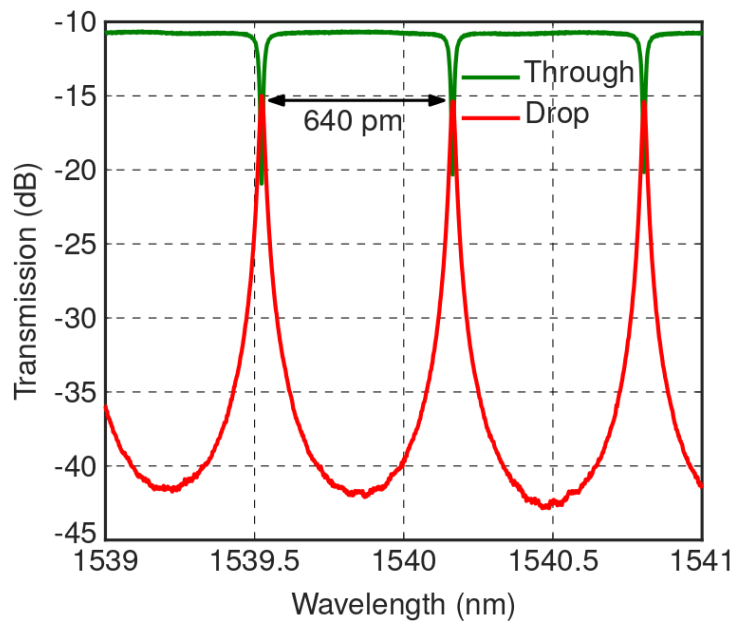


**Fig.3.2.3.** Experimental optical transmission of the silicon RR (coupling gap: 300 nm, coupling length: 4.5  $\mu\text{m}$ ).

The grating coupler was optimized for TM mode propagation and the fiber to fiber optical transmission was estimated to - 10.5 dB at 1540 nm wavelength. We used the same method explained in chapter 2 to design the add-drop RR. Several devices with different combinations of coupling-lengths / coupling-gaps were designed to search for the highest possible optical quality factors. The RRs were fabricated by using the same

processes as the ones described in section 2.4. A typical transmission spectrum measured at both the through and drop ports of the RR with a 300 nm coupling gap and a 4.5  $\mu\text{m}$  coupling length is shown in Fig.3.2.3. An  $FSR_\lambda$  of 640 pm, corresponding to  $FSR_\nu \approx 77$  GHz, was obtained, while the RR quality factor  $Q_{opt}$  estimated to around  $8.1 \times 10^4$ . The implementation of this device into the proposed tunable OEO configuration is presented in the next section.

### 3.2.3. Generation of an oscillation signal

As in the case of the spiral RR classical OEO, we evaluated the implementation of the new RR into the proposed modified OEO both in open and closed loop configurations, respectively.

#### 3.2.3a. Proposed OEO in open loop configuration

A methodology very similar to the one presented above was applied to the new studied configuration. The considered experimental setup is shown in Fig.3.2.4. The frequency response was characterized by using again the vector network analyzer (VNA-HP8510), that was placed between the RF coupler and the electro-optical modulator.

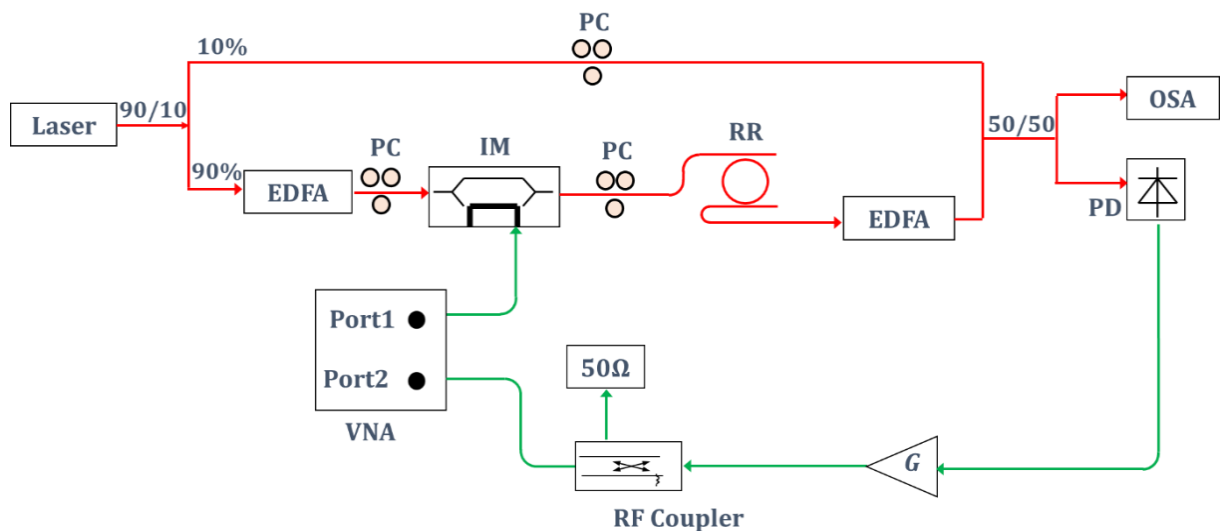


**Fig.3.2.4.** Experimental setup of the proposed tunable OEO in open loop configuration. OSA: Optical spectrum analyzer. PC: Polarization controller, IM: Intensity modulator, RR: Ring

### 3.2. Wideband tunable microwave signal generation based on silicon photonic resonator

resonator, EDFA: Erbium doped amplifier, PD: Photodetector, G: RF amplifiers, VNA: Vector network analyzer, OSA: Optical spectrum analyzer.

We used a 90/10 optical splitter to separate the intensity of the light source coming from the CW tunable laser, in which 90 % of the optical power was sent to the Erbium doped amplifier (EDFA) followed by the IM, the RR and a second EDFA. After that, a 50/50 optical combiner was used to collect the signal from the output of the second EDFA and the 10% optical power source signal, respectively, as shown in **Fig.3.2.4**. In the experimental setup, a polarization controller (PC) was used in the upper arm of the splitter in order to properly control the polarization matching between the laser source and the signal going out from the second EDFA. At the output of the 50/50 optical combiner, a second coupler (also 50/50) was placed, one arm of which being connected to an optical spectrum analyzer (OSA) in order to observe the laser or resonance wavelength, and the other arm being connected to PD. The final setup also included as in the previous system the series of RF amplifiers with a total maximum gain of 60 dB, the 10 dB RF coupler and the VNA.

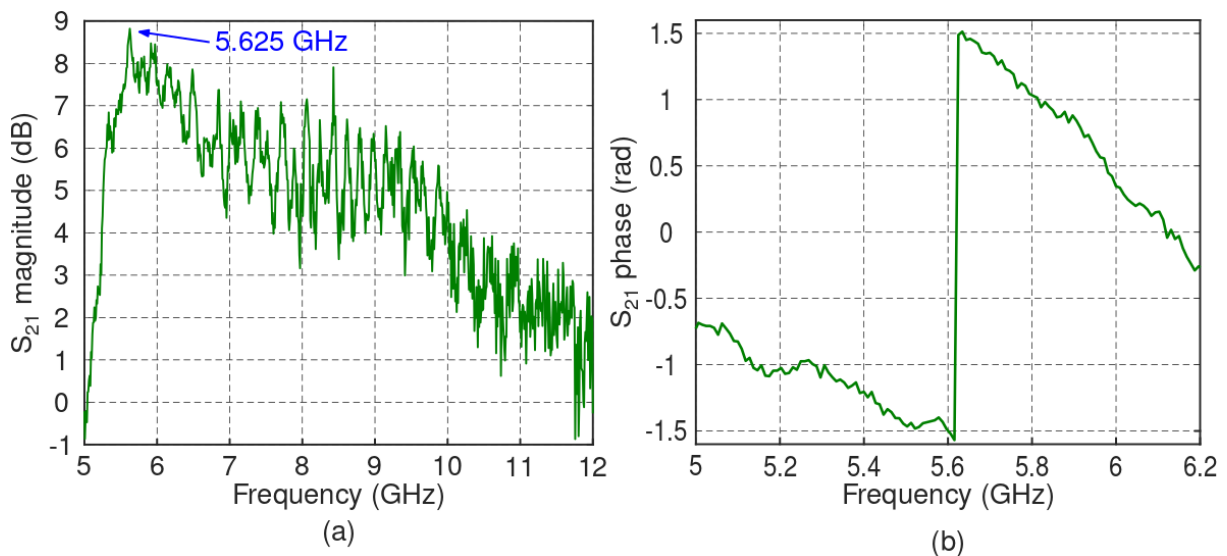


**Fig. 3.2.5.** (a)  $S_{21}$  transmission coefficient's magnitude of the beating frequency between laser and resonance wavelength, (b)  $S_{21}$  transmission coefficient's phase focus around highest magnitude value.

The applied frequency from the VNA was swept between 5 GHz and 12 GHz with the maximum available of 801 measurement points. During the experiment, the

resonance frequency of the RR  $f_R$  was first measured by an OSA. Then, the laser wavelength  $f_0$  was been tuned close to this resonance peak, the beating frequency between them was therefore allowed. The  $S_{21}$  transmission coefficient magnitude and phase monitored for the response of this beating in the microwave domain are shown in **Fig. 3.2.5**. The maximum gain was obtained at 5.625 GHz frequency. Simultaneously,  $S_{21}$  transmission coefficient phase also crosses 0 at 5.625 GHz frequency. In view of these two conditions, the generation of oscillations at this frequency could, therefore, be anticipated. Subsequently, we closed the loop, the VNA was replaced by an electronic spectrum analyzer, 90% of electrical power from the output of RF coupler being sent directly to the modulator the remaining 10% being sent to the ESA. All the other experimental conditions were kept unchanged.

#### 3.2.3b. Proposed OEO in closed loop configuration.

After closing the loop, we noted the presence of oscillations in different configurations, and this, in a reproducible way. **Fig.3.2.6** illustrates a typically obtained electrical spectrum of a generated microwave signal corresponding to the open loop configuration results reported in the previous section. As visible, an oscillation frequency at 5.625 GHz was achieved, the ESA being configured with a frequency span of 6.5 GHz and a resolution bandwidth of 200 kHz. Thanks to the wide span, a higher-order harmonic at 11.2 GHz is also observed (harmonic 2), which is caused by nonlinearities in the OEO loop <sup>14,96</sup>. The zoomed-in view of the 5.625 GHz signal, within a frequency span of 12 MHz with a resolution bandwidth of 2.2 kHz, is shown in **Fig. 3.2.6b**. Spurious oscillation peaks coming from the impact of the fiber sections used inside the loop are observed ( $\pm \sim 3.7$  MHz), in similarity with the results obtained for the fixed frequency OEO configuration based on the spiral silicon RR (see **3.1.2**).

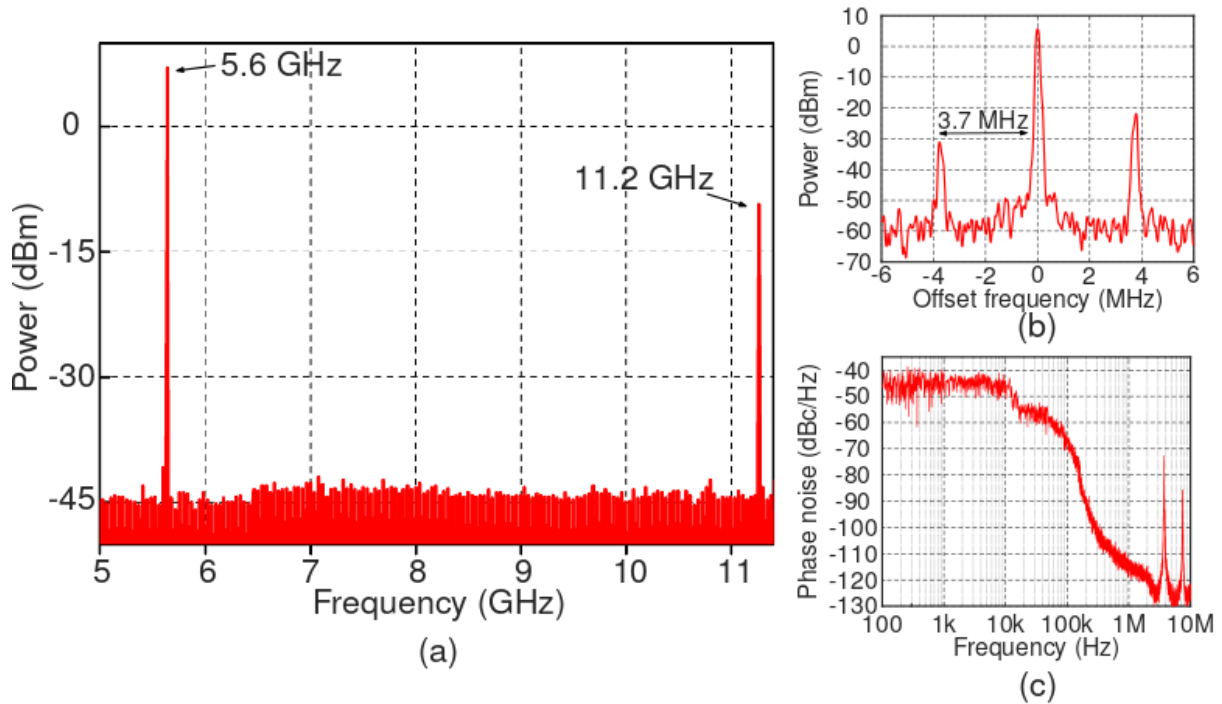


**Fig. 3.2.6.** (a) Oscillation spectrum of the generated signal based on our proposed approach, (b) zoom-in view and (c) Phase noise characteristic of the created signal.

**Figure 3.2.6c** shows the phase noise of the generated signal. As in the case of OEO based on spiral RR, a flat level around  $-45$  dBc/Hz was obtained for the phase noise spectrum. However, in this case, the flat region extended up to  $100$  kHz, which may be induced by the use of the second EDFA that probably resulted in broadening the optical signal and finally increasing the fluctuation range of the generated signal. A noise level of  $-115$  dBc/Hz at  $1$  MHz offset frequency from the carrier was obtained. Moreover, the other oscillation modes could also be seen in the phase noise spectrum at  $4$  and  $8$  MHz from the carrier, as in the case of the OEO based on a long spiral RR.

### 3.2.4. Tunable oscillation signal

After characterizing the OEO in both the open loop and closed loop configurations, we move to the main key advantage resulting from the new structure: the possibility to tune the oscillation frequency in a wide range. In order to demonstrate the wide tunability of the proposed approach, we swept the laser wavelength while keeping the resonance peak unchanged. To do so, the RR sample was placed on a Peltier module to keep a constant temperature, thereby preventing resonant wavelength shifts produced

by temperature changes. The RR resonance wavelength at 1541.25 nm was first observed from the OSA. Then, the laser wavelength was scanned between 1540.10 nm and 1540.20 nm.

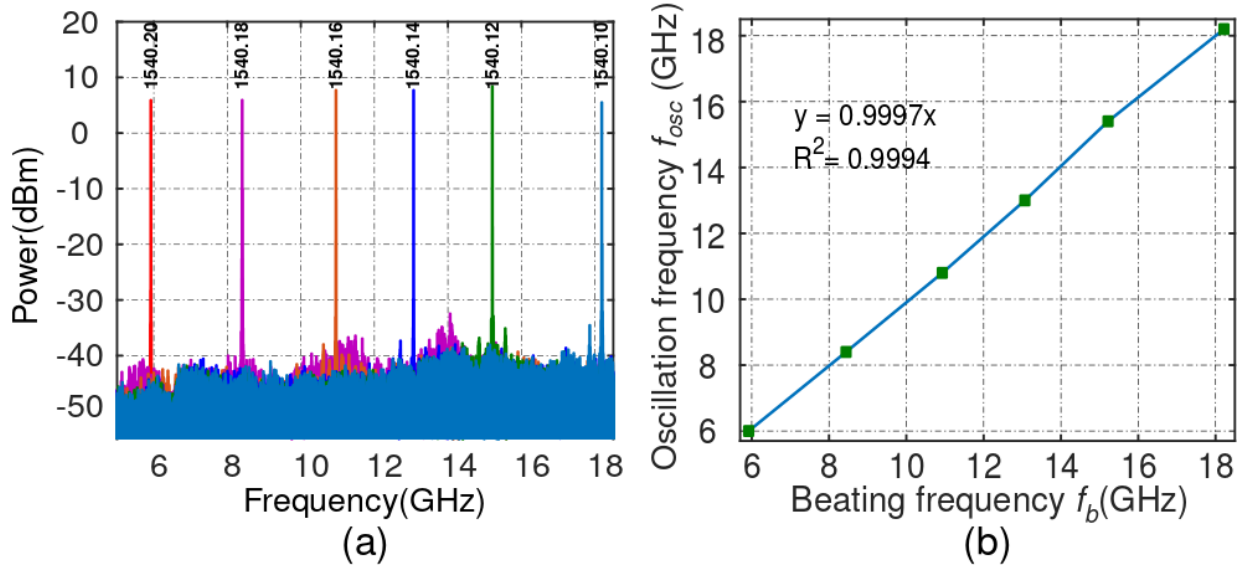


**Fig.3.2.7.** (a) Oscillation frequency generated with different laser wavelengths and (b) Plot of the oscillation frequency depending on the beating frequency, i.e.  $f_b = |f_o - f_R|$ .

Figure 3.2.7 plots the fundamental tone of the oscillation spectrum obtained by changing the laser wavelength. These experimental results demonstrate a very wide frequency tunability for a Si-based OEO, ranging from 5.9 GHz to 18.2 GHz. Note that the tuning range is only limited here by the bandwidth of the microwave amplifier used inside the loop.

From the corresponding frequency of the laser and resonance wavelength, we calculated the beating frequency, i.e.  $f_b = |f_o - f_R|$ . The evolution of the oscillation signal ( $f_{osc}$ ) as a function of the beating frequency is shown in **Fig.5b**. The oscillation frequency clearly follows the beating frequency, showing a nearly perfect linear evolution with the modification of the laser frequency separation from the RR resonance frequency (regression coefficient  $\approx 0.9997$ ). Note that in this case the laser frequency is placed in right side of the resonance peak, which explains why the oscillation signal frequency increases with the decreasing laser frequency.

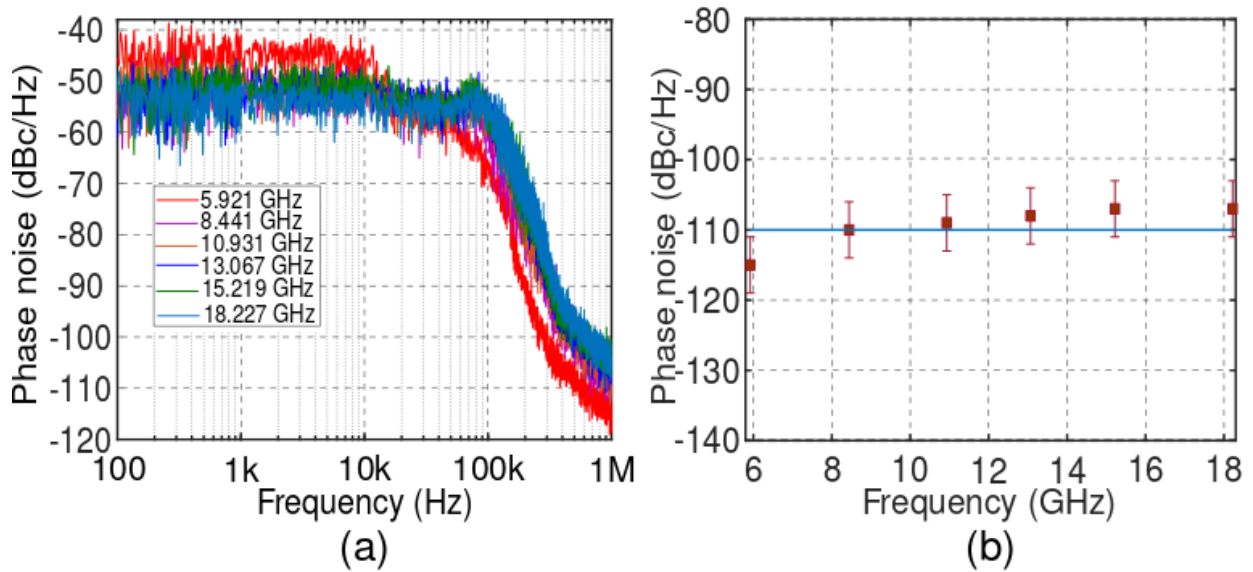


**Fig.3.2.8.** (a) Phase noise characteristic for differences generated signals and (b) Observed phase noise level at 1 MHz offset frequency from carrier.

To evaluate the performance of the modified tunable OEO, its phase noise characteristics were measured for all the generated signals. The related results are shown in **Fig.3.2.8**. Remarkably, no degradation of the phase noise is observed for increasing oscillation frequencies. **Fig.3.2.8b** represents the deduced noise level at 1 MHz offset frequency from the carrier for all the curves illustrated in **Fig.3.2.8a**. It is clear that the phase noise of the generated microwave signals is maintained around -110 dBc/Hz at the offset frequency of 1 MHz, which verifies the key advantage of an OEO to have a constant phase noise with an increasing oscillation frequency <sup>134</sup>.

### 3.2.5. Application to index sensing

Since the proposed OEO configuration had an oscillation frequency dependent on the refractive index environment of the RR waveguides, we have tested its characteristics for application in measuring optical index variations <sup>97,227</sup>. In this operating mode, the laser frequency is kept (ideally) fixed and the drift of the resonator resonance under the effect of a top cladding material index modification is detected.

We have chosen a simple way to implement this index change by changing the sample temperature, and thus indirectly the local temperature of the ring resonator. Given the difficulty in accurately measuring this local temperature, we did not attempt

to estimate its precise value. The study of the transmission spectrum of the RR using an add-drop configuration allowing to detect a shift induced by thermal effect, we focused on the estimation of the index variation that could be deduced from the modification of the optical spectrum <sup>97</sup>. During the experiment, the optical characterization of the RR and the electrical characterization of the loop based on the RR were simultaneously collected. The experimental setup shows in **Fig.3.2.9**.

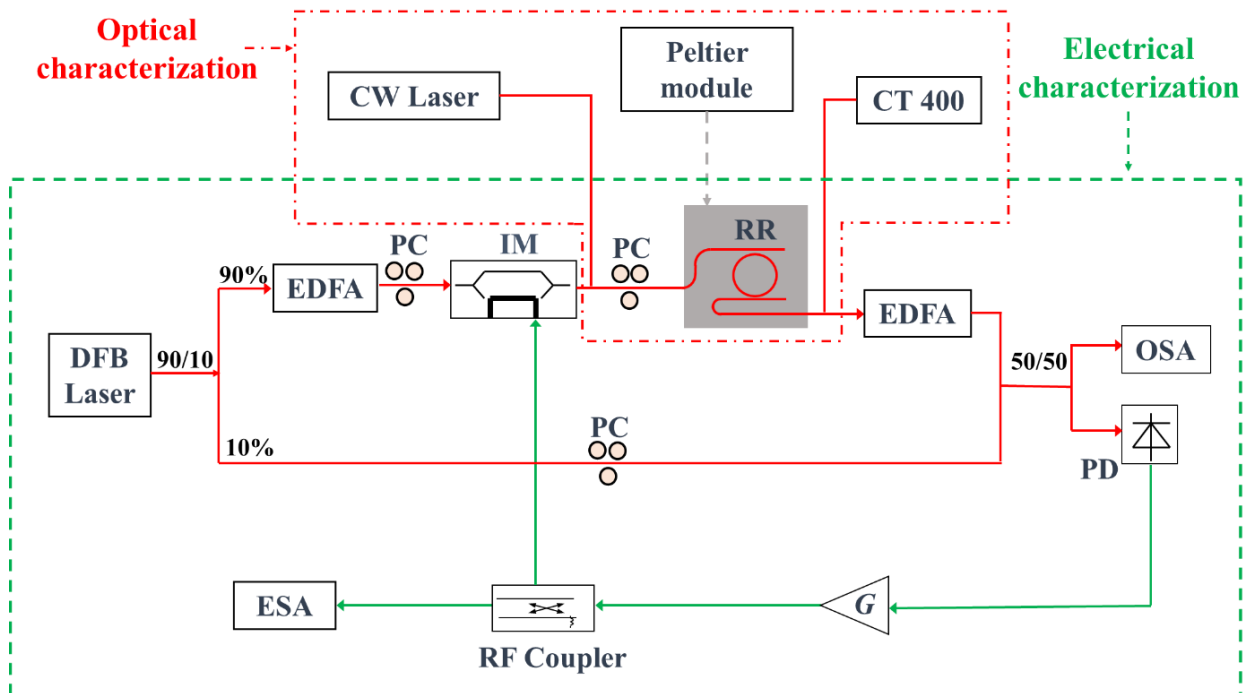


**Fig.3.2.9.** A proof of concept experiment setup dedicated to refractive sensing based on a proposed OEO.

The temperature of the RR was changed by tuning the current injected into a Peltier module placed under the sample. In order to reach a sustain local-temperature of the RR,

the measurement was started 5 min after each switching temperature point in the Peltier (in the range from 25°C to 30°C). The RR was first characterized in the optical domain by using tunable external laser (TUNIC-T100S). Right after the optical characterization, the closed loop OEO including the RR was measured. In the carried-out closed-loop experiment, a distributed feedback (DFB) diode laser (model 1905 LMI) operated at around 1.54  $\mu\text{m}$  wavelength was used in order to provide the most stable

light source as possible (see **3.1.2**). The plot of the collected signals is shown in **Fig.3.2.9**. At first

glance, a fairly strong RF frequency change can be observed from ~11 GHz to ~18.5 GHz.

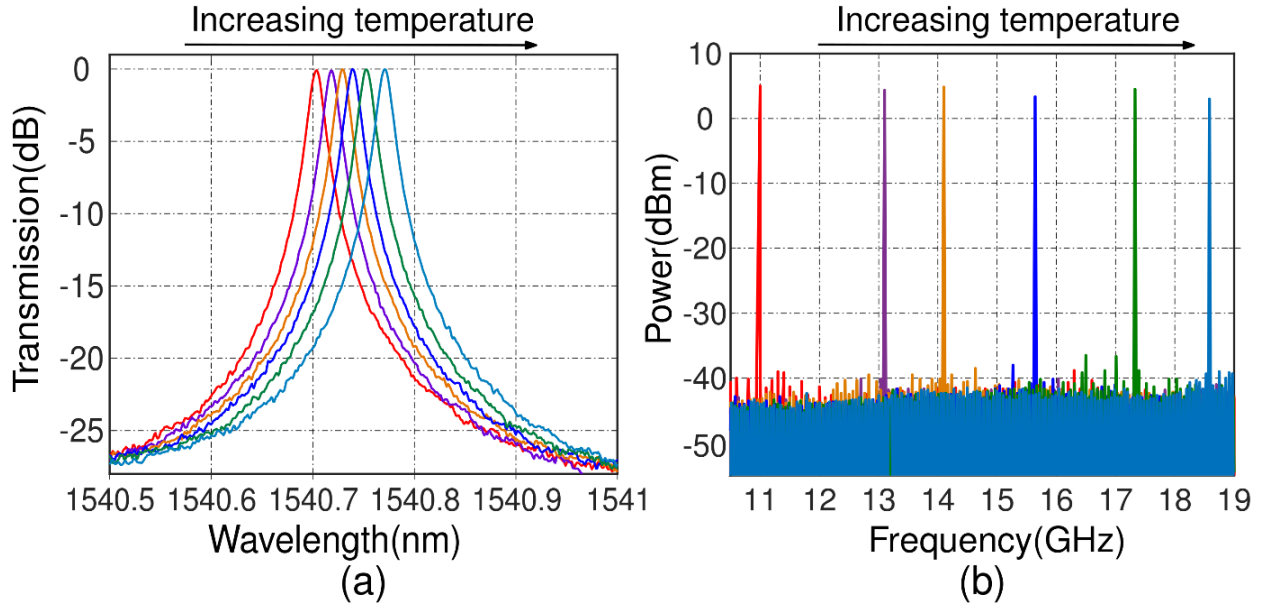


**Fig.3.2.10.** (a) Optical transmission and (b) Electrical spectrum depending on temperature.

A resonant wavelength shifted toward longer wavelengths with increasing temperature is seen, which is in agreement with the preceding theoretical and experimental analysis for SOI ring resonators<sup>97,228</sup>. Meanwhile, the generated oscillation signal frequency increases. With the objective of estimating the frequency detection sensitivity by RIU (e.g. in Hz-or-GHz/RIU), we first estimated the variation of the optical index from the collected optical spectra. This was done through the relationship between an RR resonance wavelength ( $\lambda$ ) and the effective index ( $n_{eff}$ ) are described by Eq. (2.2.1) (see section 2.2.2 of chapter 2) and can be rewritten as below:  $\lambda_{res} = \frac{n_{eff} \cdot L_{tot}}{m}$ , where  $L_{tot}$  is the optical path length and being fixed (1 mm),  $m$  is the resonance mode order which is also fixed. From Eq. (2.2.1), we deduced:  $\Delta n_{eff} = n_{eff} \frac{\Delta \lambda}{\lambda}$  (3.2.1).

It is noteworthy that, for the case described in section 3.1.3 of this chapter, the variations of the RF frequency were only depending on the cladding index changes. Here, by changing the temperature of the device, the material index values of the complete waveguide, including Si, SiO<sub>2</sub> box and cladding, are changed. Therefore, in the present studied configuration, the refractive index of the waveguide  $n_{eff}$  was

### 3.2. Wideband tunable microwave signal generation based on silicon photonic resonator

considered for evaluating the sensing property. From a vectorial optical mode solver, the waveguide refractive  $n_{eff}$  around 1.76 at 1.54 $\mu\text{m}$  wavelength was calculated. Considering the first detection resonance wavelength and its related oscillation frequency as a reference point, the change in refractive index was deduced by using **Eq. (3.2.1)**. The difference in oscillation frequency was also estimated. The deduced variation of the oscillation signal as a function of refractive index change is plotted in **Fig.3.2.11**.

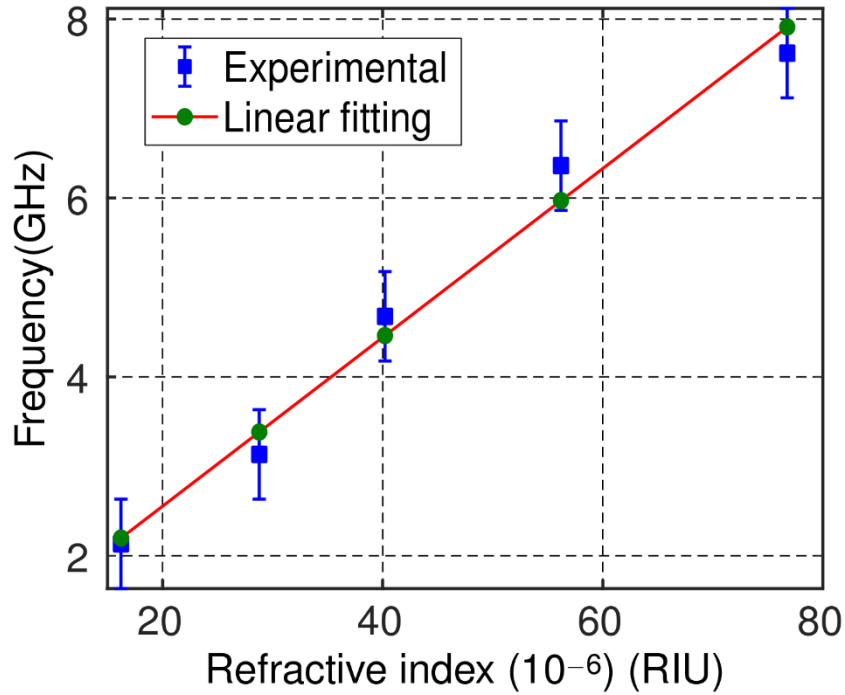


**Fig.3.2.11.** Calculation of oscillation changes versus refractive index variations.

By using a linear fitting procedure, a slope of 94350 GHz/RIU was obtained. This value is 40 times order of magnitude better than that has been obtained in <sup>182</sup> with the similar approach to study refractive index sensing by detecting frequency changes. In term of the limit of detection (LOD), we relied on results presented in section 3.2.2 that reported a stable phase noise level around -110 dBc/Hz at 1 MHz offset frequency from the carrier. A system resolution  $R$  of 1 MHz was thus considered. Then, based on Eq. (2.1.3), the limit of detection LOD was estimated at approximately  $10^{-8}$  RIU. To the best of our knowledge, this is the smallest refractive index LOD which has been reported by using an OEO scheme. It should be noted that for this first demonstration, the resonator geometry was not yet fully optimized to get the largest shift

of resonance wavelength due to temperature/refractive index changes. Our result, therefore, keeps improvement margin for future investigations.

### 3.3. Conclusion

In this chapter, studies of OEO opto-RF loops including silicon ring resonators are reported. Two different configurations of OEO based on long/short silicon ring resonators have been proposed and studied, showing a promising path for generating microwave signals as well as for applications to refractive index sensing.

In the first configuration, an mm-long spiral RR (~6mm) based OEO was studied in both open and closed loops. The microwave signal was generated under the beating between the optical carrier and a modulation sideband signal, both being selected by the optical transfer function of an add-drop resonator. Experimentally, by positioning the optical carrier on one of the transmission peaks of the RR, a good agreement between the optical  $FSR_{\lambda}$  of the RR and the microwave photonic filter frequency and the closed loop oscillation frequency was demonstrated. In the implemented example, it was around 14.12 GHz. A phase noise level at -100 dBc/Hz at 100 kHz offset frequency was evaluated for the generated oscillation signal. OEO phase noise properties have been investigated and proposals have been made to improve the noise performances of the loop. In particular, the contribution of the light source, i.e. CW and DFB laser, into the stability of the generated signal has been highlighted. The reported experimental results show that the use of a more stable laser could lead to a very significant improvement in a signal noise property. Significantly, in comparing with OEO based on CW laser, a 40 dB of noise level reduction at 1 kHz offset frequency was observed when DFB laser was employed. These results illustrate the importance of the CW light source of the opto-RF loop on the quality of the generated signal. Finally, the application of the OEO based on a long spiral RR was explored. The sensing property of the studied structure was quantified to around 3.72 GHz/RIU for a refractive index variation in the range of 1.572 to 1.688.

### 3.3. Conclusion

In a second configuration, a tunable OEO structure including a more compact silicon ring resonator has been introduced. The originality of the proposed approach lies in the way in which the RF frequency is produced. In order to remedy to the non-tunability of the previous approach, it was decided to make the RR drop port signal beat directly with the laser optical carrier. To our knowledge, this solution has not been implemented previously in the literature. In practice, in this approach, it is sufficient to position the optical carrier near a resonance of the ring to generate an oscillation. The oscillation RF signal is created under the beating between the laser light source and the single sideband modulation signal selected by an add-drop ring resonator working as an effective optical bandpass filter. By changing the wavelength spacing between the optical source and the resonance wavelength, a tunable RF oscillation signal was realized. The tunability range of this approach is extremely high, essentially limited in our case by the bandwidth of the amplifiers used inside the setup. In the implementation we have carried out, a tunability from 5.8 GHz to 18.2 GHz was demonstrated. A phase noise level of - 110 dBc/Hz at 1 MHz offset frequency from the carrier was obtained for all generated signals, showing the possibility to generate high oscillation frequencies with the same phase noise level. We then applied this approach to refractive index sensing application. An index limit of detection of  $10^{-8}$  RIU was derived in case of a system resolution limited at 1 MHz. As a whole, the reported results by the two approaches contribute to show the potential of integrated OEO for microwave signal generation and index sensing application.



# Conclusion and Perspectives

The work presented in this manuscript describes an overall study dedicated to the insertion of silicon add-drop ring resonators (RR) into several optoelectronic oscillator (OEO) systems for the generation of microwave signals. This thesis proposes a contribution to the future realization of fully integrated optoelectronic oscillators on silicon substrates.

Taking into the fact that the silicon photonics technology can nowadays offer most of the needed integrated functions for the realization of complex integrated opto-microwave circuits, the RRs presented in this work were designed and fabricated using silicon on insulator SOI substrates.

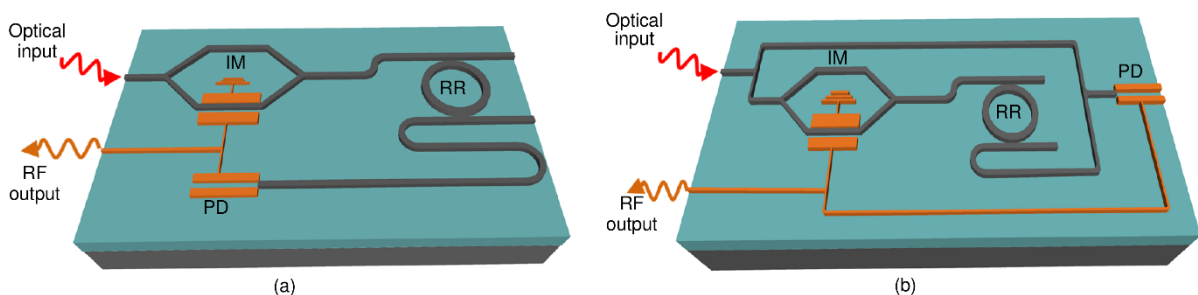
Two different configurations of OEO based on silicon add-drop RR have been proposed and studied in this manuscript.

In the first approach, a long length micro-ring resonator (~6 mm) in the shape of a spiral has been directly employed as an effective RF frequency filter (when combined with a simple quadratic detection) in order to generate an oscillation signal with a frequency equal to its free spectral range FSR. In this configuration, the RR was optimized to satisfy the target required of an FSR ~15 GHz, while our efforts and optimization have led to optical quality factors  $Q_{opt}$  typically above  $10^5$ . The implementation of the RR insertion within an OEO loop made of external (bulky) elements was succeeded. The demonstrated experiments have shown a good agreement between the optical FSR of the RR and the generated frequency. The OEO was characterized both in open loop and closed loop configurations, respectively. With an oscillation frequency of 14.12 GHz, a phase noise level of -100 dBc/Hz at an offset of 100 kHz from the carrier was demonstrated. In this first configuration, the sensitivity of the generated signal frequency with respect to bulk index cladding (covering the RR region) was estimated experimentally. A change of the RF frequency with different cladding liquids was observed, and the sensing property of the

studied closed loop system was quantified to around 3.72 GHz/RIU for a refractive index variation in the 1.512 to 1.688 range.

In the second approach, an oscillation signal was created under the beating between the laser light source and the single sideband modulation signal selected by an add-drop ring resonator working as an effective optical bandpass filter. Compared with the previous one, this approach showed a strong advantage in a flexible wideband signal tunable frequency. By changing the wavelength spacing between the optical source and the RR nearest resonance wavelength, either by sweeping the laser wavelength or shifting the resonance peak of the RR, a tunable RF signal was realized. In the implementation we have carried out, a tunability from 5.9 GHz to 18.2 GHz was demonstrated, being only limited by the working operation of the RF amplifier used within the realized setup. A phase noise level of -110 dBc/Hz at 1 MHz offset frequency was obtained for all generated signals, showing the possibility of creating high oscillation frequencies with the same phase noise level. We then applied this approach to index sensing application. An index limit of detection of  $10^{-8}$  RIU was then derived by considering system resolution of 1 MHz.

As a perspective of this work, the integration of all the elements of the opto-microwave loop is a direct objective. This task is ambitious in terms of the technological means to be implemented but, in principle, within reach since all the elements are already present "off the shelf". The artist impression following ideas of this work would be seen in the figure below.



Artist impression of (a) spiral silicon ring resonator based OEO and (b) tunable OEO based on silicon RR.

In term of RF signal performance, one important step is to further optimize the fabrication processes in order to reduce the waveguide loss. In the presented work,

devices were realized with waveguide losses around 2 dB/cm. Reducing this loss to or lower than 1 dB/cm could bring great help to improve the optical quality factor of RR and accordingly reduce the bandpass of the equivalent microwave bandpass filter. In parallel with that, improving the laser light source stability would also be an important task to further minimize the loop overall phase noise. This task can be done by using better laser performance or using a frequency-locked loop for locking the optical light source.

Regarding refractive index sensing, the carried-out work brings an initial demonstration that the application of OEO loops to monitor ultra-low index changes is a promising path. The next step should consider the fabrication and integration of microfluidic channels on top of RRs. The microfluidic device can be made by traditional Polydimethylsiloxane PDMS material or newly discovered material such as an off-stoichiometry-thiol-ene OSTE. With the help of the microfluidic channels, a further step – surface functionalization of bio-solutions on top of silicon devices could be studied. The final result including fully integrated silicon low cost OEO chips combining microfluidic channels could give rise to laboratory experiments and even commercial products.



# References

1. Marrison, W. A. The Evolution of the Quartz Crystal Clock\*. *Bell Syst. Tech. J.* **27**, 510–588 (1948).
2. Yao, X. S. & Maleki, L. High frequency optical subcarrier generator. *Electron. Lett.* **30**, 1525–1526 (1994).
3. Maleki, L. The Opto-Electronic Oscillator (OEO): Review and recent progress. in *EFTF 2012 - 2012 European Frequency and Time Forum, Proceedings* 497–500 (2012). doi:10.1109/EFTF.2012.6502432
4. Bagnell, M. & Delfyett, P. J. Optoelectronic Oscillator Using an Ultra-High Finesse Fabry-Perot Etalon as a Photonic Filter for Low Phase Noise at High Oscillating Frequencies. in *2013 IEEE International Topical Meeting on Microwave Photonics (MWP)* (2013). doi:10.1109/JLT.2013.2294944
5. Saleh, K., Merrer, P. H., Llopis, O. & Cibiel, G. Optoelectronic oscillator based on fiber ring resonator: Overall system optimization and phase noise reduction. *2012 IEEE Int. Freq. Control Symp. IFCS 2012.* 537–542 (2012). doi:10.1109/FCS.2012.6243650
6. Saleh, K., Fernandez, a., Llopis, O. & Cibiel, G. Fiber ring resonators with Q factors in excess of  $10^{10}$  for time and frequency applications. *2013 Jt. Eur. Freq. Time Forum Int. Freq. Control Symp.* 33–36 (2013). doi:10.1109/EFTF-IFC.2013.6702282
7. Matsko, A. B., Maleki, L., Savchenkov, A. A. & Ilchenko, V. S. Whispering gallery mode based optoelectronic microwave oscillator. *J. Mod. Opt.* **50**, 2523–2542 (2003).
8. Volyanskiy, K. *et al.* Compact optoelectronic microwave oscillators using ultra-high Q whispering gallery mode disk-resonators and phase modulation. *Opt. Express* **18**, 22358 (2010).
9. Marpaung, D. *et al.* Integrated microwave photonics. *Laser Photonics Rev.* **7**, 506–538 (2013).
10. Marpaung, D., Yao, J. & Capmany, J. Integrated microwave photonics. *Nat. Photonics* **13**, 80–90 (2019).
11. Fang, Z., Chen, Q. Y. & Zhao, C. Z. A review of recent progress in lasers on silicon. *Opt. Laser Technol.* **46**, 103–110 (2013).
12. Reed, G. T., Mashanovich, G., Gardes, F. Y. & Thomson, D. J. Silicon optical modulators. *Nat. Photonics* **4**, 518–526 (2010).

13. Piels, M. & Bowers, J. E. *Photodetectors for silicon photonic integrated circuits. Photodetectors: Materials, Devices and Applications* (Elsevier Ltd, 2016).  
doi:10.1016/B978-1-78242-445-1.00001-4
14. Yao, X. S. & Maleki, L. A Light-Induced Microwave Oscillator. *TDA Prog. Rep.* 42-123 47–68 (1995).
15. Khanna. Microwave oscillators: the state of the technology. *Microw. J.* **49**, 22–28 (2006).
16. Leeson, D. B. A Simple Model of Feedback Oscillator Noise Spectrum. *Proc. IEEE* **54**, 329–330 (1966).
17. Pozar, D. *Microwave Engineering Fourth Edition*. Wiley (2005). doi:TK7876.P69 2011
18. Rubiola, E. *Phase Noise and Frequency Stability in Oscillators*. Cambridge: Cambridge University Press (2008). doi:10.1017/CBO9780511812798
19. Std, I., Standards, I., Committee, C. & Board, I. S. *IEEE Standard Definitions of Physical Quantities for Fundamental Frequency and Time Metrology— Random Instabilities IEEE-SA Standards Board*. (1999).
20. <https://www.mwrf.com/components/6-types-resonators-used-across-rfmicrowave-universe>.
21. Neyer, A. & Voges, E. High-frequency electro-optic oscillator using an integrated interferometer. *Appl. Phys. Lett.* **40**, 6–8 (1982).
22. Logan, R. T., Maleki, L. & Shadaram, M. Stabilization of Oscillator Phase Using a Fiber-Optic Delay-Line. in *Forty-Firh Annual Symposium On Frequency Control* 508–512 (1991).
23. Yao, X. S. & Maleki, L. Opto-Electronic Microwave Oscillator. *Opt. Photonics News* **13**, 1725–1735 (1996).
24. Yao, X. S., Maleki, L. & Eliyahu, D. Progress in the opto-electronic oscillator - a ten year anniversary review. in *2004 IEEE MTT-S International Microwave Symposium Digest (IEEE Cat. No.04CH37535)* **1**, 4–7 (2004).
25. Eliyahu, D., Seidel, D. & Maleki, L. Phase Noise of a High Performance OEO and an Ultra Low Noise Floor Cross-Correlation Microwave Photonic Homodyne System. in *2008 IEEE International Frequency Control Symposium* 811–814  
doi:10.1093/annonc/mdu259
26. Eliyahu, D., Sariri, K., Taylor, J. & Maleki, L. Optoelectronic oscillator with improved phase noise and frequency stability. in *Photonic Integrated Systems* **4998**, 139–147 (2003).

27. X. Steve Yao, Maleki, L., Ji, Y., Lutes, G. & Tu, M. Dual-loop opto-electronic oscillator. in *1998 IEEE International Frequency Control Symposium* 545–549 doi:10.1109/freq.1998.717952
28. Eliyahu, D. & Maleki, L. Low phase noise and spurious level in multi-loop opto-electronic oscillators. in *Proceedings of the 2003 IEEE International Frequency Control Symposium and PDA Exhibition Jointly with the 17th European Frequency and Time Forum* 405–410 (2003). doi:10.1109/freq.2003.1275126
29. Devgan, P. A Review of Optoelectronic Oscillators for High Speed Signal Processing Applications. *ISRN Electron.* **2013**, (2013).
30. Bánky, T., Horváth, B. & Berceli, T. Optimum configuration of multiloop optoelectronic oscillators. *J. Opt. Soc. Am. B* **23**, 1371–1380 (2006).
31. Cho, J. H., Kim, H. & Sung, H. K. Reduction of spurious tones and phase noise in dual-loop OEO by loop-gain control. *IEEE Photonics Technol. Lett.* **27**, 1391–1393 (2015).
32. Yao, X. S. & Maleki, L. Multiloop optoelectronic oscillator. *IEEE J. Quantum Electron.* **36**, 79–84 (2000).
33. Zhou, W. & Blasche, G. Injection-locked dual opto-electronic oscillator with ultra-low phase noise and ultra-low spurious level. *IEEE Trans. Microw. Theory Tech.* **53**, 929–933 (2005).
34. Okusaga, O. *et al.* Spurious mode reduction in dual injection-locked optoelectronic oscillators. *Opt. Express* **19**, 5839 (2011).
35. Hong, J., Li, Z., Liu, A., Yao, S. & Wang, X. New kind of injection-locked oscillator and its corresponding long-term stability control. *Appl. Opt.* **54**, 8187 (2015).
36. Lelievre, O. *et al.* Ultra low noise 10 GHz dual loop optoelectronic oscillator: Experimental results and simple model. in *2016 IEEE International Frequency Control Symposium, IFCS 2016 - Proceedings* (2016). doi:10.1109/FCS.2016.7546719
37. Sotom, M., Benazet, B. & Maigna, M. A flexible telecom satellite repeater based on microwave photonic technologies. in *International Conference on Space Optics — ICSO 2006 technologies* **10567**, 105672A1-7 (2006).
38. Pan, S. *et al.* Satellite Payloads Pay Off. *IEEE Microw. Mag.* 61–73 (2015).
39. <http://www.oewaves.com/micro-oeo>.
40. Panasiewicz, J. A photonic BPSK modulation with 2 . 5 GHz RF signal from a microwave optoelectronic oscillator. in *International Microwave and Optoelectronics Conference* (2015). doi:10.1109/IMOC.2015.7369209

41. Ilgaz, M. A. & Batagelj, B. Opto-electronic oscillator in the mm-W range for 5G wireless and mobile networks: Design challenges and possible solutions. in *2017 International Conference on Optical Network Design and Modeling (ONDM)* 1–5 (2017). doi:10.23919/ONDM.2017.7958522
42. Alsharif, M. H. & Nordin, R. Evolution towards fifth generation (5G) wireless networks: Current trends and challenges in the deployment of millimetre wave, massive MIMO, and small cells. *Telecommun. Syst.* **64**, 617–637 (2017).
43. Mitchell, J. E. FiWiN5G - Fiber-Wireless Integrated Networks for 5th Generation delivery. *Int. Conf. Transparent Opt. Networks 2016-Augus*, 2016–2019 (2016).
44. Agiwal, M., Roy, A. & Saxena, N. Next Generation 5G Wireless Networks: A Comprehensive Survey. *IEEE Commun. Surv. Tutorials* **18**, 1617–1655 (2016).
45. Yin, B. *et al.* High sensitivity axial strain and temperature sensor based on dual-frequency optoelectronic oscillator using PMFBG Fabry- Perot filter. *Opt. Express* **25**, 14106–14113 (2017).
46. Zou, X. *et al.* Optoelectronic oscillators (OEOs) to sensing, measurement, and detection. *IEEE J. Quantum Electron.* **52**, (2016).
47. Zou, X. *et al.* Optical length change measurement via RF frequency shift analysis of incoherent light source based optoelectronic oscillator. **22**, 14905–14912 (2014).
48. Cui, P. *et al.* Absolute Distance Measurement Using an Optical Comb and an Optoelectronic Oscillator. *IEEE Photonics Technol. Lett.* **30**, 744–747 (2018).
49. Yin, B. *et al.* High-sensitivity temperature sensor based on an optoelectronic oscillator. *Opt. Express* **38**, 14106–14113 (2012).
50. Zhu, Y., Jin, X., Chi, H., Zheng, S. & Zhang, X. High-sensitivity temperature sensor based on an optoelectronic oscillator. *Appl. Opt.* **53**, 5084 (2014).
51. Liu, J., Wang, M., Tang, Y. & Yang, Y. Switchable Optoelectronic Oscillator Using an FM-PS-FBG for Strain and Temperature Sensing. *IEEE Photonics Technol. Lett.* **29**, 2008–2011 (2017).
52. Nguyen, L. D., Nakatani, K. & Journet, B. Refractive index measurement by using an optoelectronic oscillator. *IEEE Photonics Technol. Lett.* **22**, 857–859 (2010).
53. Kong, F., Member, S., Romeira, B., Zhang, J. & Member, S. A Dual-Wavelength Fiber Ring Laser Incorporating an Injection-Coupled Optoelectronic Oscillator and Its Application to Transverse Load Sensing. *J. Light. Technol.* **20**, 1784–1793 (2014).
54. Kong, F., Li, W. & Yao, J. Transverse load sensing based on a dual-frequency optoelectronic oscillator. *Opt. Lett.* **38**, 2611–3 (2013).

55. Ozdur, I., Mandridis, D., Hoghooghi, N. & Delfyett, P. J. Low Noise Optically Tunable Opto-Electronic Oscillator With Fabry-Perot Etalon. *J. Light. Technol.* **28**, 3100–3106 (2010).
56. Kim, J. M. & Cho, D. Optoelectronic oscillator stabilized to an intra-loop Fabry-Perot cavity by a dual servo system. *Opt. Express* **18**, 14905–12 (2010).
57. Bagnell, M., Davila-Rodriguez, J. & Delfyett, P. J. Millimeter-wave generation in an optoelectronic oscillator using an ultrahigh finesse etalon as a photonic filter. *J. Light. Technol.* **32**, 1063–1067 (2014).
58. Saleh, K., Llopis, O. & Cibiel, G. Optical scattering induced noise in fiber ring resonators and optoelectronic oscillators. *J. Light. Technol.* **31**, 1433–1446 (2013).
59. Ward, J. & Benson, O. WGM microresonators: Sensing, lasing and fundamental optics with microspheres. *Laser Photonics Rev.* **5**, 553–570 (2011).
60. Savchenkov, A. A. *et al.* Whispering-gallery mode based opto-electronic oscillators. *2010 IEEE Int. Freq. Control Symp. FCS 2010* 554–557 (2010).  
doi:10.1109/FREQ.2010.5556268
61. Saleh, K. *et al.* Phase noise performance comparison between optoelectronic oscillators based on optical delay lines and whispering gallery mode resonators. *Opt. Express* **22**, 32158 (2014).
62. Nguimdo, R. M. *et al.* Phase noise performance of optoelectronic oscillators based on whispering-gallery mode resonators. *IEEE J. Quantum Electron.* **51**, 1–6 (2015).
63. Coillet, A. *et al.* Microwave Photonics Systems Based on Whispering-gallery-mode Resonators. *J. Vis. Exp.* 1–9 (2013). doi:10.3791/50423
64. Leinse, A., Sales, S., Marpaung, D. & Roeloffzen, C. Integrated microwave photonics. (2012).
65. Mishra, V. & Gupta, S. Microwave Photonic Filter : A Systematic Literature Review. *Int. J. Adv. Res. Comput. Commun. Eng.* **6**, 628–634 (2017).
66. Capmany, J. & Novak, D. Microwave photonics combines two worlds. *Nat. Photonics* **1**, 319–330 (2007).
67. Iezekiel, S. *et al.* RF Engineering Meets Optoelectronics. *IEEE Microw. Mag.* 28–45 (2015).
68. Ławniczuk, K. *et al.* Open access to technology platforms for InP-based photonic integrated circuits. *Adv. Opt. Technol.* **4**, 157–165 (2015).
69. Smit, M. *et al.* An introduction to InP-based generic integration technology. *Semicond. Sci. Technol.* **29**, (2014).

70. Pérez, D. *et al.* Multipurpose silicon photonics signal processor core. *Nat. Commun.* **8**, 1–9 (2017).
71. Fandiño, J. S., Muñoz, P., Doménech, D. & Capmany, J. A monolithic integrated photonic microwave filter. *Nat. Photonics* 1–7 (2016). doi:10.1038/nphoton.2016.233
72. Roeloffzen, C. G. H. *et al.* Low-loss Si<sub>3</sub>N<sub>4</sub> triplex optical waveguides: Technology and applications overview. *IEEE J. Sel. Top. Quantum Electron.* **24**, (2018).
73. Augustin, L. M. *et al.* InP-Based Generic Foundry Platform for Photonic Integrated Circuits. *IEEE J. Sel. Top. Quantum Electron.* **24**, (2018).
74. Blumenthal, D. J. *et al.* Planar waveguides with less than 0.1 dB/m propagation loss fabricated with wafer bonding. *Opt. Express* **19**, 24090 (2011).
75. Qianfan Xu *et al.* Silicon microring resonators with 1.5- $\mu$ m radius. *Opt. Express* **16**, 4309–4315 (2008).
76. Thomson, D. *et al.* Roadmap on silicon photonics. *J. Opt. (United Kingdom)* **18**, 1–20 (2016).
77. Duan, G. H. *et al.* Hybrid III - V on silicon lasers for photonic integrated circuits on silicon. *IEEE J. Sel. Top. Quantum Electron.* **20**, (2014).
78. Karouta, F. *et al.* An InP-based photonic integrated beamformer for phased-array antennas. in *Optical Amplifiers and Their Applications/Integrated Photonics Research, Technical Digest (CD) (Optical Society of America, 2004)* (2014). doi:10.1364/ipr.2004.ifb2
79. Zhuang, L. *et al.* On-chip microwave photonic beamformer circuits operating with phase modulation and direct detection. *Opt. Express* **22**, 17079 (2014).
80. Lin, C. Y. *et al.* Silicon nanomembrane based photonic crystal waveguide array for wavelength-tunable true-time-delay lines. *Appl. Phys. Lett.* **101**, 1–5 (2012).
81. Xie, J., Zhou, L., Li, Z., Wang, J. & Chen, J. Seven-bit reconfigurable optical true time delay line based on silicon integration. *Opt. Express* **22**, 22707 (2014).
82. Norberg, E. J., Guzzon, R. S., Parker, J. S., Johansson, L. A. & Coldren, L. A. Programmable photonic microwave filters monolithically integrated in InP-InGaAsP. *J. Light. Technol.* **29**, 1611–1619 (2011).
83. Liu, Y., Marpaung, D., Choudhary, A., Hotten, J. & Eggleton, B. J. Link performance optimization of chip-based Si<sub>3</sub>N<sub>4</sub>microwave photonic filters. *J. Light. Technol.* **36**, 4361–4370 (2018).
84. Lloret, J. *et al.* Tunable complex-valued multi-tap microwave photonic filter based on single silicon-on-insulator microring resonator. *Opt. Express* **19**, 12402 (2011).

85. Liu, X. *et al.* Silicon-on-insulator-based microwave photonic filter with narrowband and ultrahigh peak rejection. *Opt. Lett.* **43**, 1359–1362 (2018).
86. Xing, Y. *et al.* Digitally controlled phase shifter using an SOI slot waveguide with liquid crystal infiltration. *IEEE Photonics Technol. Lett.* **27**, 1269–1272 (2015).
87. Marpaung, D. *et al.* Low-power, chip-based stimulated Brillouin scattering microwave photonic filter with ultrahigh selectivity. *Optica* **2**, 76 (2015).
88. Pant, R. *et al.* On-chip stimulated Brillouin Scattering for microwave signal processing and generation. **14**, 1–14 (2014).
89. Zhang, M., Wang, C., Cheng, R., Shams-Ansari, A. & Loncar, M. Monolithic Ultrahigh-Q Lithium Niobate Microring Resonator. **4**, 1536–1537 (2017).
90. Wang, C., Zhang, M., Stern, B., Lipson, M. & Loncar, M. Nanophotonic Lithium Niobate Electro-optic Modulators. **26**, 1547–1555 (2017).
91. Wang, C. *et al.* Integrated lithium niobate electro-optic modulators operating at CMOS-compatible voltages. *Nature* (2018). doi:10.1038/s41586-018-0551-y
92. Yeniay, A. & Gao, R. True time delay photonic circuit based on perfluoropolymer waveguides. *IEEE Photonics Technol. Lett.* **22**, 1565–1567 (2010).
93. DiMitrAdIs, A. I. *et al.* Polymer-Based Additive Manufacturing of High- Performance Waveguide and Antenna Components. in *Proceedings of the IEEE* 668–676 (2017).
94. Tang, J. *et al.* Integrated optoelectronic oscillator. *Opt. Express* **26**, 12257–12265 (2018).
95. Erklein, M. O. M. *et al.* Widely tunable , low phase noise microwave source based on a photonic chip. *Opt. Lett.* **41**, 4633–4636 (2016).
96. Zhang, W. & Yao, J. Silicon Photonic Integrated Optoelectronic Oscillator for Frequency-Tunable Microwave Generation. *J. Light. Technol.* **36**, 4655–4663 (2018).
97. Chew, S. X. *et al.* Optoelectronic oscillator based sensor using an on-chip sensing probe. *IEEE Photonics J.* **9**, (2017).
98. Maleki, L. Sources: The optoelectronic oscillator. *Nat. Photonics* **5**, 728–730 (2011).
99. Pant, R. *et al.* On-chip stimulated Brillouin scattering. *Opt. Express* **19**, 8285–8290 (2011).
100. Soref, R., Fellow, L. & Paper, I. The Past, Present, and Future of Silicon Photonics. *Sel. Top. Quantum Electron. IEEE J.* **12**, 1678–1687 (2006).
101. Zhou, Z., Yin, B. & Michel, J. On-chip light sources for silicon photonics. *Light Sci. Appl.* **4**, 1–13 (2015).
102. Hoang, T. H. C. *et al.* Narrow-linewidth carbon nanotube emission in silicon hollow-

- core photonic crystal cavity. *Opt. Lett.* **42**, 2228–2231 (2017).
103. Bradley, J. D. B. *et al.* Monolithic erbium- and ytterbium-doped microring lasers on silicon chips. *Opt. Express* **22**, 12226 (2014).
  104. Li, N. *et al.* Monolithically integrated erbium-doped tunable laser on a CMOS-compatible silicon photonics platform. *Opt. Express* **26**, 16200 (2018).
  105. Li, N. *et al.* C-Band Swept Wavelength Erbium-Doped Fiber Laser With a High-Q Tunable Interior-Ridge Silicon Microring Cavity. *Opt. Express* **24**, 22741–22748 (2016).
  106. Fan, H., Hua, S., Jiang, X. & Xiao, M. Demonstration of an erbium-doped microsphere laser on a silicon chip. *Phys. Rev. A* **74**, 72–75 (2006).
  107. Polman, A., Min, B., Kalkman, J., Kippenberg, T. J. & Vahala, K. J. Ultralow-threshold erbium-implanted toroidal microlaser on silicon. *Appl. Phys. Lett.* **84**, 1037–1039 (2004).
  108. Camacho-Aguilera, R. E. *et al.* An electrically pumped germanium laser. *Opt. Express* **20**, 11316–11320 (2012).
  109. Crosnier, G. *et al.* Hybrid indium phosphide-on-silicon nanolaser diode. *Nat. Photonics* **11**, 297–300 (2017).
  110. Liu, J. *et al.* Ge-on-Si optoelectronics. *Thin Solid Films* **520**, 3354–3360 (2012).
  111. Spitzer, W. G., Trumbore, F. A. & Logan, R. A. Properties of Heavily Doped *n*-Type Germanium. *J. Appl. Phys.* **32**, 1822–1830 (1961).
  112. Walle, V. De. Band theory. *Phys. Rev.* **39**, (1989).
  113. He, G. & Atwater, H. A. Interband Transitions in  $\text{Sn}_x\text{Ge}_{1-x}$  Alloys. *Phys. Rev. Lett.* **79**, 1937–1940 (1997).
  114. Lee, J. H. *et al.* High power and widely tunable Si hybrid external-cavity laser for power efficient Si photonics WDM links. *Opt. Express* **22**, 7678–7685 (2014).
  115. Wang, T., Liu, H., Lee, A., Pozzi, F. & Seeds, A. 1.3- $\mu\text{m}$  InAs/GaAs quantum-dot lasers monolithically grown on Si substrates. *Opt. Express* **19**, 2931–2936 (2011).
  116. Fang, A. W. *et al.* Electrically pumped hybrid AlGaInAs-silicon evanescent laser. *Opt. Express* **14**, 9203 (2006).
  117. Groenert, M. E. *et al.* Monolithic integration of room-temperature cw GaAs/AlGaAs lasers on Si substrates via relaxed graded GeSi buffer layers. *J. Appl. Phys.* **93**, 362–367 (2003).
  118. Langdo, T. A. *et al.* High quality Ge on Si by epitaxial necking. *Appl. Phys. Lett.* **76**, 3700–3702 (2000).

119. Liu, A. Y. *et al.* High performance continuous wave 1.3  $\mu$  m quantum dot lasers on silicon. *Appl. Phys. Lett.* **104**, 3–7 (2014).
120. Chen, S. *et al.* Electrically pumped continuous-wave III-V quantum dot lasers on silicon. *Nat. Photonics* **10**, 307–311 (2016).
121. Zhang, J. *et al.* Transfer-printing-based integration of a III-V-on-silicon distributed feedback laser. *Opt. Express* **26**, 8821 (2018).
122. Liu, A., Jones, R., Liao, L. & Samara-rubio, D. A high-speed silicon optical modulator based on a metal – oxide – semiconductor capacitor. *Nature* **427**, 615–619 (2004).
123. Xu, Q., Schmidt, B., Pradhan, S. & Lipson, M. Micrometre-scale silicon electro-optic modulator. *Nature* **435**, 325–327 (2005).
124. Dionne, J. A., Diest, K., Sweatlock, L. A. & Atwater, H. A. PlasMOSStor : A Metal - Oxide - Si Field Effect Plasmonic Modulator. *Nano Lett.* **9**, 879–902 (2009).
125. Oessbacher, C. H. *et al.* Plasmonic modulator with > 170 GHz bandwidth demonstrated at 100 GBd NRZ. *Opt. Express* **25**, 159–164 (2017).
126. Liu, M. *et al.* A graphene-based broadband optical modulator. *Nature* **474**, 64–67 (2011).
127. Soriano, V. *et al.* Graphene-silicon phase modulators with gigahertz bandwidth. *Nat. Photonics* **12**, 40–44 (2018).
128. Koos, C. *et al.* All-optical high-speed signal processing with silicon – organic hybrid slot waveguides. **3**, 1–4 (2009).
129. Koeber, S. *et al.* Femtojoule electro-optic modulation using a silicon – organic hybrid device. (2015). doi:10.1038/lisa.2015.28
130. Roelkens, G. *et al.* III-V-on-Silicon Photonic Devices for Optical Communication and Sensing. *Photonics* **2**, 969–1004 (2015).
131. Chmielak, B. *et al.* Pockels effect based fully integrated , strained silicon electro-optic modulator. **19**, 17212–17219 (2011).
132. Lischke, S. *et al.* High bandwidth, high responsivity waveguide-coupled germanium p-i-n photodiode. *Opt. Express* **23**, 27213–27220 (2015).
133. Li, M., Wang, L., Li, X., Xiao, X. & Yu, S. Silicon intensity Mach–Zehnder modulator for single lane 100 Gb/s applications. *Photonics Res.* **6**, 109 (2018).
134. Yao, X. S. & Malelu, L. Optoelectronic Oscillator for Photonic Systems. *J. quantum Electron. Electron.* **32**, 1141–1149 (1996).
135. Tang, Z. *et al.* Tunable optoelectronic oscillator based on a polarization modulator and a chirped FBG. *IEEE Photonics Technol. Lett.* **24**, 1487–1489 (2012).

136. Xu, H. *et al.* High-speed silicon modulator with band equalization. *Opt. Lett.* **39**, 4839 (2014).
137. Milivojevic, B. *et al.* Demonstration of Optical Transmission at Bit Rates of Up to 321.4 Gb/s Using Compact Silicon Based Modulator and Linear BiCMOS MZM Driver. *J. Light. Technol.* **35**, 768–774 (2017).
138. Ohira, K., Kobayashi, K., Iizuka, N. & Yoshida, H. On-chip optical interconnection by using integrated III-V laser diode and photodetector with silicon waveguide. *Opt. Express* **18**, 15440–15447 (2010).
139. Piels, M., Bauters, J. F., Davenport, M. L., Heck, M. J. R. & Bowers, J. E. Low-Loss Silicon Nitride AWG Demultiplexer Heterogeneously Integrated With Hybrid III–V/Silicon Photodetectors. *J. Light. Technol.* **32**, 817–823 (2014).
140. Lischke, S. *et al.* –1 V bias 67 GHz bandwidth Si-contacted germanium waveguide p-i-n photodetector for optical links at 56 Gbps and beyond. *Opt. Express* **24**, 4622–4631 (2016).
141. Bowers, J. *et al.* Integrated Optical Amplifiers on Silicon Waveguides. *Integr. Photonics Nanophotonics Res. Appl. / Slow Fast Light ITuG1* (2007).  
doi:10.1364/IPNRA.2007.ITuG1
142. Kuyken, B. *et al.* On-chip parametric amplification with 265 dB gain at telecommunication wavelengths using CMOS-compatible hydrogenated amorphous silicon waveguides. *Opt. Lett.* **36**, 552 (2011).
143. Bi, L. *et al.* On-chip optical isolation in monolithically integrated non-reciprocal optical resonators. *Nat. Photonics* **5**, 758–762 (2011).
144. Wang, C., Zhong, X. L. & Li, Z. Y. Linear and passive silicon optical isolator. *Sci. Rep.* **2**, 1–6 (2012).
145. Li, Q., Soltani, M., Yegnanarayanan, S. & Adibi, A. Design and demonstration of compact, wide bandwidth coupled-resonator filters on a silicon-on-insulator platform. *Opt. Express* **17**, 2247–2254 (2009).
146. Bogaerts, W. *et al.* Silicon-on-insulator spectral filters fabricated with CMOS technology. *IEEE J. Sel. Top. Quantum Electron.* **16**, 33–44 (2010).
147. Liu, A. L. A. *et al.* Wavelength Division Multiplexing Based Photonic Integrated Circuits on Silicon-on-Insulator Platform. *IEEE J. Sel. Top. Quantum Electron.* **16**, 23–32 (2010).
148. Dai, D., Wang, J. & Shi, Y. Silicon mode (de)multiplexer enabling high capacity photonic networks-on-chip with a single-wavelength-carrier light. *Opt. Lett.* **38**, 1422

- (2013).
149. Ye, W. N. *et al.* Passive broadband silicon-on-insulator polarization splitter. *Opt. Lett.* **32**, 1492 (2007).
  150. Duval, D. & Lechuga, L. M. Optical Waveguide Biosensors. *Photonics Sci. Found. Technol. Appl.* **4**, 323–365 (2015).
  151. Gavela, A. F., Garc?a, D. G., Ramirez, J. C. & Lechuga, L. M. Last advances in silicon-based optical biosensors. *Sensors (Switzerland)* **16**, 1–15 (2016).
  152. Fan, X. *et al.* Sensitive optical biosensors for unlabeled targets: A review. *Anal. Chim. Acta* **620**, 8–26 (2008).
  153. Estevez, M. C., Alvarez, M. & Lechuga, L. M. Integrated optical devices for lab-on-a-chip biosensing applications. *Laser Photon. Rev.* **6**, 463–487 (2012).
  154. Claes, T., Bogaerts, W. & Bienstman, P. Experimental characterization of a silicon photonic biosensor consisting of two cascaded ring resonators based on the Vernier-effect and introduction of a curve fitting method for an improved detection limit. *Opt. Express* **18**, 22747 (2010).
  155. E.F. Schipper, A.M. Brugman, C. Dominguez, L.M. Lechuga, R.P.H. Kooyman, j. G. The realization of an integrated Mach-Zehnder waveguide immunosensor in silicon technology. *Sensors Actuators B* **40**, I47-I53 ' (1997).
  156. Tang, T. & Luo, L. Refractive index sensor of Mach–Zehnder interferometer based on thermo-optic effect of SOI waveguide. *Optik (Stuttg.)* **127**, 6366–6370 (2016).
  157. Qin, K., Hu, S., Retterer, S. T., Kravchenko, I. I. & Weiss, S. M. Slow light Mach–Zehnder interferometer as label-free biosensor with scalable sensitivity. *Opt. Lett.* **41**, 753 (2016).
  158. Densmore, A. *et al.* A silicon-on-insulator photonic wire based evanescent field sensor. *IEEE Photonics Technol. Lett.* **18**, 2520–2522 (2006).
  159. De Vos, K., Bartolozzi, I., Schacht, E., Bienstman, P. & Baets, R. Silicon-on-Insulator microring resonator for sensitive and label-free biosensing. *Opt. Express* **15**, 7610 (2007).
  160. Kim, H.-T. & Yu, M. Cascaded ring resonator-based temperature sensor with simultaneously enhanced sensitivity and range. *Opt. Express* **24**, 9501 (2016).
  161. Claes, T. *et al.* Label-free biosensing with a slot-waveguide-based ring resonator in silicon on insulator. *IEEE Photonics J.* **1**, 197–204 (2009).
  162. Ciminelli, C., Dell’Olio, F., Conteduca, D., Campanella, C. M. & Armenise, M. N. High performance SOI microring resonator for biochemical sensing. *Opt. Laser*

- Technol.* **59**, 60–67 (2014).
163. Jugessur, A. S., Dou, J., Aitchison, J. S., De La Rue, R. M. & Gnan, M. A photonic nano-Bragg grating device integrated with microfluidic channels for bio-sensing applications. *Microelectron. Eng.* **86**, 1488–1490 (2009).
  164. Wang, X. *et al.* A silicon photonic biosensor using phase-shifted Bragg gratings in slot waveguide. *J. Biophotonics* **6**, 821–828 (2013).
  165. Prabhathan, P., Murukeshan, V. M., Jing, Z. & Ramana, P. V. Compact SOI nanowire refractive index sensor using phase shifted Bragg grating. *Opt. Express* **17**, 15330 (2009).
  166. Lee, M. R. & Fauchet, P. M. Two-dimensional silicon photonic crystal based biosensing platform for protein detection. *Opt. Express* **15**, 4530 (2007).
  167. Lai, W.-C., Chakravarty, S., Wang, X., Lin, C. & Chen, R. T. On-chip methane sensing by near-IR absorption signatures in a photonic crystal slot waveguide. *Opt. Lett.* **36**, 984 (2011).
  168. Lai, W. C., Chakravarty, S., Zou, Y., Guo, Y. & Chen, R. T. Slow light enhanced sensitivity of resonance modes in photonic crystal biosensors. *Appl. Phys. Lett.* **102**, (2013).
  169. Zhang, Y. N., Zhao, Y. & Lv, R. Q. A review for optical sensors based on photonic crystal cavities. *Sensors Actuators, A Phys.* **233**, 374–389 (2015).
  170. Chrostowski, L. *et al.* Silicon photonic resonator sensors and devices. in *Proc. of SPIE* **8236**, 823620 (2012).
  171. Fan, X. & White, I. M. Optofluidic Microsystems for Chemical and Biological Analysis. *Nat. Photonics* **5**, 591–597 (2011).
  172. Fard, S. T. *et al.* Performance of ultra-thin SOI-based resonators for sensing applications. *Opt. Express* **22**, 14166 (2014).
  173. Fan, I. M. W. and X. On the performance quantification of resonant refractive index sensors. *Opt. Express* **16**, 1020–1028 (2008).
  174. Yoshie, T., Tang, L. & Su, S. Y. Optical microcavity: Sensing down to single molecules and atoms. *Sensors* **11**, 1972–1991 (2011).
  175. Stern, L. *et al.* Ultra-precise optical to radio frequency based chip-scale refractive index and temperature sensor. *Optica* **4**, 1 (2017).
  176. Yao, J. Microwave Photonics for High-Resolution and High-Speed Interrogation of Fiber Bragg Grating Sensors. *Fiber Integr. Opt.* **34**, 230–242 (2015).
  177. Yao, J. Microwave photonics for high-resolution and high-speed interrogation of fiber

- Bragg grating sensors. *Fiber Integr. Opt.* **34**, 204–216 (2015).
178. Bernou, C., Rebière, D. & Pistré, J. Microwave sensors: a new sensing principle. Application to humidity detection. *Sensors Actuators, B Chem.* **68**, 88–93 (2000).
  179. Cao, Y. *et al.* Resolution-improved in situ DNA hybridization detection based on microwave photonic interrogation. *Opt. Express* **23**, 27061 (2015).
  180. Yin, B. *et al.* High sensitivity axial strain and temperature sensor based on dual-frequency optoelectronic oscillator using PMFBG Fabry-Perot filter. *Opt. Express* **25**, 14106–14113 (2017).
  181. Yao, J. Optoelectronic Oscillators for High Speed and High Resolution Optical Sensing. *J. Light. Technol.* **35**, 3489–3497 (2017).
  182. Yao, J., Liu, J., Deng, H. & Zhang, W. On-Chip Sensor for Simultaneous Temperature and Refractive Index Measurements Based on a Dual-Passband Microwave Photonic Filter. *J. Light. Technol.* **36**, 4099–4105 (2018).
  183. Pavesi, L. V. and L., Lorenzo, Vivien, L., Pavesi, L. V. and L. & Lorenzo. *Handbook of Silicon Photonics*. (2013). doi:10.1201/b14668-4
  184. Chrostowski, L. & Hochberg, M. *Silicon Photonics Design From Devices to Systems*. Cambridge university press (2015). doi:10.1017/CBO9781316084168
  185. Ye, W. N. & Xiong, Y. Review of silicon photonics: History and recent advances. *J. Mod. Opt.* **60**, 1299–1320 (2013).
  186. Bogaerts, W. & Chrostowski, L. Silicon Photonics Circuit Design: Methods, Tools and Challenges. *Laser Photonics Rev.* **12**, 1–29 (2018).
  187. Bogaerts, W. *et al.* Silicon microring resonators. *Laser Photonics Rev.* **6**, 47–73 (2012).
  188. Xu, D. X. *et al.* Silicon photonic integration platform-Have we found the sweet spot? *IEEE J. Sel. Top. Quantum Electron.* **20**, (2014).
  189. Marris-Morini, D. *et al.* Germanium-based integrated photonics from near-to mid-infrared applications. *Nanophotonics* **7**, 1781–1793 (2018).
  190. D.J. Lockwood and L. Pavesi. Chapter 1 Silicon Photonic Wire Waveguides: Fundamentals and Applications. in *Silicon Photonics II* **119**, 1–29 (2011).
  191. Wang, J. & Long, Y. On-chip silicon photonic signaling and processing: a review. *Sci. Bull.* (2018). doi:10.1016/j.scib.2018.05.038
  192. Almeida, V. R., Xu, Q., Barrios, C. A. & Lipson, M. Guiding and confining light in void nanostructure. *Opt. Lett.* **29**, 1209–1211 (2004).
  193. Densmore, A. *et al.* Silicon photonic wire biosensor array for multiplexed real-time and label-free molecular detection. *Opt. Lett.* **34**, 3598 (2009).

194. Dell'Olio, F. & Passaro, V. M. N. Optical sensing by optimized silicon slot waveguides. *Opt. Express* **15**, 4977–4993 (2007).
195. Selvaraja, S. K. *et al.* Highly uniform and low-loss passive silicon photonics devices using a 300nm CMOS platform. *Conf. Opt. Fiber Commun. Tech. Dig. Ser.* 3–5 (2014). doi:10.1109/OFC.2014.6886713
196. Kita, D. M., Michon, J., Johnson, S. G. & Hu, J. Are slot and sub-wavelength grating waveguides better than strip waveguides for sensing? **5**, (2018).
197. Lin Zhang, Yunchu Li, Jeng-Yuan Yang, Muping Song, Raymond G. Beausoleil, and A. E. W. Silicon-Based Microring Resonator Modulators for Intensity Modulation. *IEEE J. Sel. Top. Quantum Electron.* **16**, 149–158 (2010).
198. Lotsch, H. K. V *et al.* *Optical Microresonators Theory, Fabrication, and Applications.* (Springer Series in OPTICAL SCIENCES, 2009).
199. Yu, J. *et al.* High performance micro-fiber coupler-based polarizer and band-rejection filter. *Opt. Express* **20**, 17258 (2012).
200. K. Okamoto. Fundamental of Optical Waveguides. in *Elsevier Academic Press* Chap. 4 (Elsevier Inc., 2006). doi:10.1016/B978-0-12-385469-8.05002-4
201. Lindecrantz, S. M. & Helleso, O. G. Estimation of propagation losses for narrow strip and rib waveguides. *IEEE Photonics Technol. Lett.* **26**, 1836–1839 (2014).
202. Vlasov, Y. & McNab, S. Losses in single-mode silicon-on-insulator strip waveguides and bends. *Opt. Express* **12**, 1622–1631 (2004).
203. Bogaerts, W. & Selvaraja, S. K. Compact single-mode silicon hybrid rib/strip waveguide with adiabatic bends. *IEEE Photonics J.* **3**, 422–432 (2011).
204. Altissimo, M. E-beam lithography for micro-/nanofabrication. *Biomicrofluidics* **4**, (2010).
205. Carroll, L. *et al.* Photonic Packaging: Transforming Silicon Photonic Integrated Circuits into Photonic Devices. *Appl. Sci.* **6**, 426 (2016).
206. Li, C. *et al.* Silicon photonics packaging with lateral fiber coupling to apodized grating coupler embedded circuit. *Opt. Express* **22**, 24235 (2014).
207. Lim, A. E. J. *et al.* Review of Silicon Photonics Foundry Efforts. *IEEE J. Sel. Top. Quantum Electron.* **20**, (2014).
208. Mekis, A. *et al.* A Grating-Coupler-Enabled CMOS Photonics Platform. *ResearchGate* **17**, 597–608 (2011).
209. Nambiar, S., Sethi, P. & Selvaraja, S. Grating-Assisted Fiber to Chip Coupling for SOI Photonic Circuits. *Appl. Sci.* **8**, 1142 (2018).

210. Altissimo, M. E-beam lithography for micro-/nanofabrication. *Biomicrofluidics* **4**, 2–7 (2010).
211. Cen Shawn Wu et.al. High-energy Electron Beam Lithography for Nanoscale Fabrication. in *Lithography*
212. NanoBeam nB4 Electron Beam Writer Standard Operating Procedures. (2015).
213. Delâge, A. *et al.* Wavelength-dependent model of a ring resonator sensor excited by a directional coupler. *J. Light. Technol.* **27**, 1172–1180 (2009).
214. Yu, J. *et al.* High performance micro-fiber coupler-based polarizer and band-rejection filter. *Opt. Express* **20**, 17258 (2012).
215. Xiao, S., Khan, M. H., Shen, H. & Qi, M. Modeling and measurement of losses in silicon-on-insulator resonators and bends. *Opt. Express* **15**, 10553–10561 (2007).
216. Saleh, K., Lin, G. & Chembo, Y. K. Effect of laser coupling and active stabilization on the phase noise performance of optoelectronic microwave oscillators based on whispering-gallery-mode resonators. *IEEE Photonics J.* **7**, (2015).
217. Volyanskiy, K., Chembo, Y. K., Larger, L. & Rubiola, E. Contribution of laser frequency and power fluctuations to the microwave phase noise of optoelectronic oscillators. *J. Light. Technol.* **28**, 2730–2735 (2010).
218. Erklein, M. O. M. *et al.* Widely tunable , low phase noise microwave source based on a photonic chip. **41**, (2016).
219. Nelson, C. W., Hati, A. & Howe, D. A. Relative intensity noise suppression for RF photonic links. *IEEE Photonics Technol. Lett.* **20**, 1542–1544 (2008).
220. Li, W. & Yao, J. An Optically Tunable Optoelectronic Oscillator. *J. Light. Technol.* **28**, 2640–2645 (2010).
221. Lelievre, O. *et al.* A model for designing ultralow noise single- and dual-loop 10-GHz optoelectronic oscillators. *J. Light. Technol.* **35**, 4366–4374 (2017).
222. Guill, M. A., Caverley, M., Cretu, E., Jaeger, N. A. F. & Chrostowski, L. Large-Area , High- Q SOI Ring Resonators. *2014 IEEE Photonics Conf. IPC 2014* **4**, 336–337 (2014).
223. <https://m.raith.com/products/raith150-two.html>.
224. Rooks, M. J. *et al.* Low stress development of poly(methylmethacrylate) for high aspect ratio structures. *J. Vac. Sci. Technol. B Microelectron. Nanom. Struct.* **20**, 2937 (2002).
225. <http://www.cargille.com/refractivestandards.shtml>.
226. Yao, J. Microwave photonics. *J. Light. Technol.* **27**, 314–335 (2009).

227. Yao, J. Optoelectronic oscillators for high speed and high resolution optical sensing. **35**, 3489–3497 (2017).
228. Kim, G.-D. *et al.* Silicon photonic temperature sensor employing a ring resonator manufactured using a standard CMOS process. *Opt. Express* **18**, 22215–22221 (2010).

**Titre :** Oscillateurs optoélectroniques à base de résonateurs silicium pour applications à la génération de signaux hyperfréquences et aux capteurs.

**Mots clés :** Oscillateur optoélectronique, Photonique, Photonique hyperfréquence, Résonateur optique, Capteur, Bruit de phase.

**Résumé :** Ces travaux portent sur l'insertion de résonateurs en anneau de silicium dans des boucles d'oscillateurs optoélectroniques (OOE) pour la génération de signaux micro-ondes à faible bruit de phase et constituent une contribution à la future intégration complète des systèmes OOE en photonique silicium. L'orientation de l'application qui a été explorée a été d'évaluer la performance de ces systèmes pour la détection de variations d'indice optique en volume. Deux configurations différentes de résonateurs en anneau de silicium à base d'OOE ont été proposées et démontrées : des OOE à base de résonateurs en anneau silicium millimétriques et des OOE accordables à base d'anneaux plus compacts et d'un schéma spécifique de réinjection de porteuse optique.

Dans la première approche, le signal optique est utilisé comme porteuse optique, qui est modulée par un modulateur d'intensité qui produit un ensemble de deux bandes latérales dans le domaine optique, tandis que le résonateur en anneau génère un peigne optique qui agit comme un filtre optique, transposant son intervalle spectral libre (ISL) dans le domaine micro-onde. Par le battement des deux raies optiques adjacentes dans un photodétecteur, l'information est ainsi traduite dans le domaine RF. La contribution de notre travail a été de démontrer que la réalisation de résonateurs millimétriques (environ 6mm) en photonique silicium était une approche viable et intéressante pour la réalisation directe d'OOE. Dans les configurations étudiées, les résonateurs en anneau SOI ont été optimisés pour satisfaire la cible requise d'un ISL d'environ 15 GHz et un facteur de qualité optique supérieur à  $10^5$ . Les résultats expérimentaux obtenus ont démontré la viabilité et la stabilité de l'approche proposée, tandis qu'un niveau de bruit de phase de  $-100\text{dBc/Hz}$  à un décalage de 100 kHz par rapport à la porteuse et une capacité de détection du système d'environ  $3,72\text{ GHz/RIU}$  ont été quantifiés pour une variation de l'indice de réfraction comprise entre 1,572 et 1,688, en bon accord avec les résultats des simulations.

En complément de cette première étape, nous avons abordé la question très importante de l'accordabilité de la fréquence du signal hyperfréquence généré. À cette fin, nous avons proposé, conçu, puis développé et testé une configuration d'OOE originale, basée sur l'utilisation d'une seule bande de modulation et d'un mécanisme de réinjection de la porteuse optique du laser de la boucle. Dans ce schéma, le signal oscillant est créé par le battement entre le faisceau laser et une bande latérale unique du signal de modulation sélectionnée par un résonateur en anneau. Dans l'implémentation que nous avons réalisée, un résonateur photonique SOI avec un ISL de 77 GHz et un facteur de qualité optique à  $8,1 \times 10^4$  a été utilisé. En modifiant la fréquence du laser tout en conservant une longueur d'onde de résonance du résonateur fixe, une accordabilité de 5,8 GHz à 18,2 GHz a été démontrée, étant seulement limitée par le fonctionnement de l'amplificateur RF utilisé dans les expériences réalisées. Parallèlement, un niveau de bruit de phase de  $-115\text{ dBc/Hz}$  à une fréquence de décalage de 1 MHz a été obtenu pour tous les signaux générés, démontrant la possibilité de créer des fréquences d'oscillation élevées avec le même niveau de bruit de phase. Nous avons ensuite appliqué cette approche à la détection de l'indice de réfraction en volume et démontré une sensibilité de détection de  $94350\text{ GHz/RIU}$  et une limite de détection d'indice de  $10^{-8}\text{ RIU}$  en considérant une résolution de signal de 1 MHz. Au-delà de ces résultats expérimentaux, l'apport de cette seconde approche apporte une solution simple et flexible au problème de la génération de signaux hyperfréquences à fréquences variables à la demande, et ouvre des perspectives d'application très riches.

Tous les résultats de la thèse contribuent à la question de l'intégration des OOE sur puces silicium et permettent d'anticiper diverses applications dans le domaine des communications et des capteurs.

**Title:** Silicon resonators based optoelectronic oscillators for applications in microwave signal generation and sensing

**Keywords:** Optoelectronic oscillator, Photonics, Microwave photonics, Optical resonators, Sensor, Phase noise.

**Abstract:** This work focuses on the insertion of silicon ring resonators into the loops of optoelectronic oscillators (OEO) for the generation of low phase noise microwave signals and is a contribution to the future full integration of OEO systems on single silicon chips. The application orientation that was explored was to evaluate the performance of these systems for bulk optical index detection. Two different configurations of silicon ring resonators based OEO have been proposed and demonstrated: OEO based on millimeter-long silicon ring resonators and tunable OEO based on more compact silicon ring resonators and a specific optical carrier reinjection scheme.

In the first approach, the optical signal is used as an optical carrier, which is modulated by an intensity modulator that produces a set of sidebands in the optical domain, while the ring resonator generates an optical comb that acts as an optical filter, translating its Free Spectral Range (FSR) into the microwave domain. By the beating of two adjacent optical comb lines in a photodetector, the optical spectral lines are then translated into the RF domain. The contribution of our work has been to demonstrate that the realization of millimeter resonators (about 6mm) in silicon photonics was a viable and interesting approach for the direct realization of OEO. In the investigated configurations, SOI ring resonators were optimized to satisfy the required target of a FSR of around 15GHz and an optical quality factor above 105. The demonstrated experimental results showed the viability and the stability of the proposed approach, while phase noise level of -100dBc/Hz at an offset of 100 kHz from carrier was obtained and sensing capability of the studied system was quantified to around 3.72 GHz/RIU for a refractive index variation in the range of 1.572 to 1.688, in good agreement with simulation results.

In a complementary direction to this first step, we addressed the very important issue of the tunability of the frequency of the microwave signal generated. To this end, we proposed, designed, and then developed and tested an original OEO configuration based on the use of a single modulation band and a mechanism for reinjection of the optical carrier from the loop laser. In this scheme, the oscillation signal is created under the beating between the laser light beam and a single modulation signal sideband selected by an add-drop ring resonator working as an effective optical bandpass filter. In the implementation we have carried out, a SOI photonic resonator with a FSR of 77 GHz and an optical quality factor at  $8.1 \times 10^4$  was used. By changing the laser frequency while keeping a fixed resonator resonance wavelength, a tunability from 5.8GHz to 18.2GHz was demonstrated, being only limited by the working operation of the RF amplifier used in the carried-out experiments. Meanwhile, a phase noise level of -115 dBc/Hz at 1MHz offset frequency was obtained for all generated signals, showing the possibility of creating high oscillation frequencies with the same phase noise level. We then applied this approach for bulk refractive index sensing application and demonstrated a sensing sensitivity of 94350GHz/RIU and an index limit of detection of 10-8 RIU by considering a signal resolution of 1MHz. Beyond these experimental results, the contribution of this second approach provides a simple and flexible solution to the problem of generating microwave signals with variable frequencies on demand and opens up very rich application perspectives.

All the results of the thesis contribute to the question of the integration of OEOs on silicon chips and make it possible to anticipate various applications in the field of communications and sensors.